Conductance through Nanometer-scale Metal-to-Graphite Contacts

A Dissertation
Presented to
The Academic Faculty

by

Asmerom Y. Ogbazghi

In Partial Fulfillment
of the Requirements for the Degree
Doctor of Philosophy

School of Physics
Georgia Institute of Technology
March 2005

Conductance through Nanometer-scale Metal-to-Graphite Contacts

Approved by :

Dr. Phillip First, Advisor
School of Physics
Georgia Institute of Technology , Advisor

Dr. Edward Conrad
School of Physics
Georgia Institute of Technology

Dr. Walt deHeer
School of Physics
Georgia Institute of Technology

Dr. Andrew Zangwill
School of Physics
Georgia Institute of Technology

Dr. Robert Whetten
School of Chemistry & Biochemistry
Georgia Institute of Technology

Date Approved: March 18, 2005

To my Parents,

Yemane Ogbazghi and Alganesh Belay

ACKNOWLEDGEMENTS

I would like to express my sincere gratitude and appreciation to my advisor Dr. Phillip First, for his guidance and expertise to my graduate experience. I most grateful for his support, kindness, and patience with me through out my study. I am also indebted for him for allow me to study Electrical Engineering. I consider myself very fortune and honored to have been one of his students. I would like also to thank Dr. Walt deHeer for his collaboration and input to our project. Next, I would to thank the rest of my Thesis committee members Dr. Edward Conrad, Dr. Robert Whetten, and Dr. Andrew Zangwill.

I am thankful for Dr. Claire Berger for her initial input to my project. I also thank my fellow group members Tianbo Li, Sameh Dardona and Jianfe Shao. They each helped make my time in the PhD program more fun and interesting.

I would like to thank Dr. Asmerom Hagos and his wife Selome for their love, support and prayer through out my study. My gratitude also goes to Rev. Gebremichael Yohannes for his prayer and encouragements. I would like to thank my church members Medhane Alem Eritrean Orthodox Church for their prayer and support during my study.

I would also like to thank my family for the support and prayer they provided me through my entire life. Finally, my thanks goes to my God for blessed me with the ability to undertake and finally complete my study.

TABLE OF CONTENTS

LIST OF TABLES

LIST OF FIGURES

SUMMARY

The metal/graphite interface is interesting due to the typically large disparity in the characteristics of the electronic structure (e.g. Fermi wavelength and Fermi energy) and dimensionality (3D in the metal versus quasi-2D in graphite). The goal of this work is to determine how the contact conductance to graphite depends on the metal contact area for nanometer-scale contacts. From this we deduce the effect of electronic screening in the graphite. Three different metals were chosen for this work: Solid Cu and Al, and liquid Ga. Liquid Ga provided a unique opportunity to reduce the effect of mechanical interactions to near zero, while Cu and Al were chosen for their different electronic structures. At the interface between the metal and graphite, the large Fermi wavevector of Al should allow phase matching of Al states to those in graphite, while the Cu Fermi surface lies inside of all available graphite wavevector states.

Conductance spectra as a function of tip displacement toward the graphite sample [$G(Z)$] were obtained using a scanning tunneling microscope. The contact area and force for the solid tips were estimated from the DMT (Derjaguin-Muller-Toporov) contact model using experimental deformation displacements. The spectra always began by breaking the contact completely, i.e. by retracting the tip to beyond the point at which the conductance became zero. We observed very small initial contact conductance (a few nS; 1 Siemen = 1 Ω^{-1}) for small tip displacements with all of the metals. The hysteresis between forward- and reverse-traced conductance spectra was very small for small Z displacement. This indicates elastic mechanical interactions. Consequently, we attribute features in the $G(Z)$ spectra, particularly distinct plateaus and regions of reversible *negative* dG/dz, to the electronic structure of the metal-graphite interface. A simple model was developed to explain the results for small tip-sample displacements.

Remarkably, it was found possible to image the graphite surface with liquid metal tips in contact with the surface. This enabled us to correlate conductance features with the

atomic-scale surface structure of the graphite. The contact radius for the Ga tip during imaging was estimated to be $\sim 2.5\ nm$ from the width of atomic step edges on the graphite. This is much smaller than expected from the macroscopic radius of the Ga liquid drop (tens to a few hundred micrometers). The drop apparently distorts dramatically in the applied electric field to a conical shape (the Taylor cone) with a very small radius of curvature at its apex.

CHAPTER I

INTRODUCTION

Carbon nanotubes (CNTs) are promising materials for electronic devices and it has been suggested that they could become an alternative to the standard Si technology [1–4]. It is known, though not often appreciated, that graphite has an electronic structure very similar to CNTs. A major challenge in creating future nanometer-scale devices will be to control the electronic properties of the contact that exists at the interface of a metal and the nanoscale material. The issue is analogous to the control of Schottky barrier heights in metal/semiconductor contacts, to which decades of prior research has been devoted. In this Thesis, the contact conductance at the interface of a nanometer-scale metal tip and the surface of highly-oriented pyrolytic graphite (HOPG) has been studied, with the contact area adjusted via a scanning tunneling microscope (STM). While this is not identical to the problem of contacting a nanoscale graphitic element (e.g. a CNT), results from this controlled geometry will be important for understanding the general problem of contacts to carbon-based nanodevices [5, 6].

Nanometer-scale contacts between metals have been studied for many years [7, 8], with several interesting results. Most prominent among these is the quantization of conductance, discovered first in a 2D electron system [9]. Experiments in the early 1990's [10–13] demonstrated that conductance quantization in nanoscale wires and constrictions was a very general phenomenon, even at room temperature. In these experiments, the conductance $G = I/V$ is found to occur in integer multiples of the "conductance quantum" $Go = 2e^2/h = (12.9\,\mathrm{k}\Omega)^{-1}$ (this definition includes 2-fold spin-degeneracy). Metallic constrictions of only a few atoms diameter reach a resistance of $12.9\,\mathrm{k}\Omega$. In contrast, a recent experiment investigating metal-to-graphite contact resistance [14] showed that even for much larger contact areas, the contact resistance was around $1\,\mathrm{M}\Omega$. Contact experiments between a CNT and graphite also have been done [15] and the measured contact

resistance was large (50 $k\Omega$). Furthermore, the measurements showed a dependence on the angle of the CNT with respect to the graphite surface, which indicated the important role of electronic structure in graphitic materials.

This Thesis describes measurements of the contact conductance of different metals to graphite, including a liquid metal (gallium). The metals (Cu, Al, Ga) were chosen to encompass a range of different Fermi surface cross-sections, which affects the states available for transmission across the interface. We will present the behavior of conductance as a function of contact radius (controlled via STM tip displacement) and force (or pressure) for each of these metals contacted to graphite.

In the first Chapter, we will review the electronic structure of graphite, contact conductance, and contact mechanics. In Chapter II we present the experimental setup and procedures for collecting the data. Chapters III and IV will present the experimental results and some discussion. We discuss the aspects common to all metals in Chapter V, and summarize the conclusions of this work in Chapter VI.

1.1 Graphite

The atomic configuration of a carbon atom is $1s^2 2s^2 2p^2$, with an ionization potential of 11.2 eV [16]. Carbon exists in diamond, graphite, fullerene, and nanotube forms. Graphite is very widely used in the production of fibers, carbon nanotubes, lubricants etc. All of these different materials are built from the same sp^2 (trigonal) bonding of the carbon atoms, unlike diamond which is built from sp^3 (tetrahedral) bonding of carbon atoms. Tetrahedral bonding forms a rigid three-dimensional crystal structure of covalent bonds.

Graphite has four valence electrons, and the angle between nearest-neighbor sp^2-bonded atoms is 120^o. The carbon atom in each layer is bonded to three other carbon atoms, forming a series of hexagons. The distance between two nearest atoms is 1.42 $\mathring{A}$ and the lattice constant a in the unit cell is 2.46 $\mathring{A}$. The spacing $c/2$ between graphite layers is 3.35 $\mathring{A}$, which is approximately twice the van der Waals radius of carbon [17].

The in-plane bonding in graphite is covalent, and as a result it is a good electrical and thermal conductor within the layer. Between the layers, however, bonding is due to the

weak van der Waals interaction, and as a consequence graphite is a poor electrical and thermal conductor perpendicular to the layers. The calculated interlayer binding energy is about 27 meV/atom [18] and the measured binding energy 52±5 meV/atom [19], which is one-hundred times smaller than the tight-binding interaction between in-plane neighbors. Thus, in many cases, the properties of graphite are similar to those of a single sp^2-bonded sheet of carbon atoms, i.e. "graphene."

Natural graphite crystals are made of a series of stacked parallel graphene planes, which occur in three different stacking sequences. The simplest crystal structure is the **AAA** stacking sequence for which there are two atoms per unit cell. The layers are placed on top of each other, aligned in the xy plane. The second crystal structure is known as the Bernal crystal structure and its stacking sequence is **ABABAB**. Figure 1 shows the Bernal crystal structure, where every other plane is shifted in the horizontal direction to give the **ABABAB** stacking. There are four atoms per unit cell. The Bernal crystal structure is the most common and stable stacking sequence of graphite. In this crystal structure the atoms in B sites (open circles in Fig. 1) have a different chemical environment from the atoms in the A sites (full circles) [20]. The B-atoms have no direct neighbors in adjacent planes, while the A-atoms do have direct neighbors in the adjacent planes.

The third crystal structure is the **ABCABC** stacking sequence, which forms a rhombohedral crystal structure. The carbon atoms in every third layer are superimposed. There are six atoms per hexagonal unit cell or there are two atoms per rhombohedral unit cell [21]. The chemical environment in layers A, B and C are different from each other. This stacking order is thermodynamically unstable and can not be found in a pure form but can be found in combination with Bernal graphite crystal structure.

1.1.1 Physical Properties of Graphite

The anisotropic atomic binding in the graphite crystal creates an anisotropic material, with striking differences between properties measured perpendicular to the graphene planes versus within the planes. The elastic constants for different crystallographic directions are [22]:

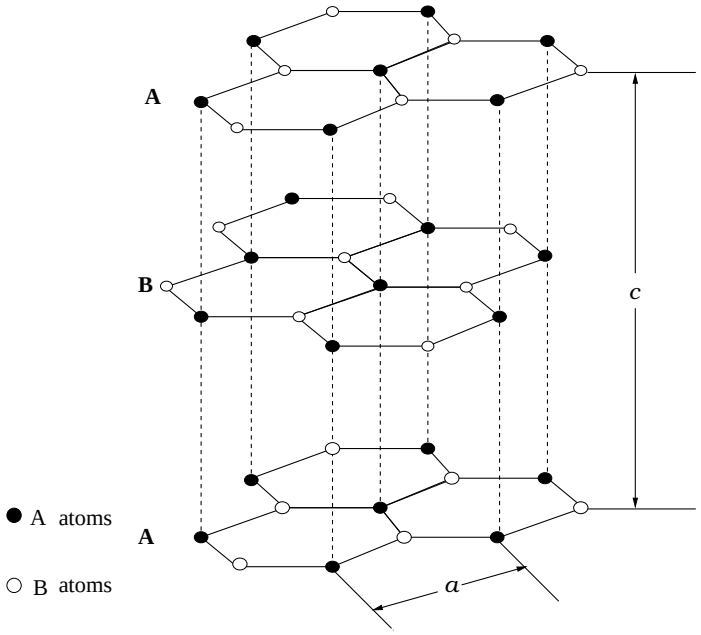

Figure 1: The crystal structure of graphite **ABABA** (Bernal Structure). The primitive unit cell with dimensions $a = 2.46$ $\mathring{A}$ and $c = 6.70$ $\mathring{A}$. There are four atoms per unit cell. The atoms with full circles (A atoms) have neighbors directly above and below in the adjacent layer planes but the atoms with open circles (B atoms) have neighbors above and below in layer planes 6.70 $\mathring{A}$ away.

C_{11}=1060 GPa (a direction)

C_{33}=36.5 GPa (c direction)

C_{44}=4.5 GPa (shear parallel to the plane).

The Young's modulus (C_{11}) parallel to the graphene planes is larger than the perpendicular Young's modulus (C_{33}) due to the atoms in the basal plane being tightly bonded to each other. The interaction between the layers is very weak and as a result the Young's modulus in c-axis (C_{33}) and the shear modulus C_{44} are very small.

The color of graphite is black and the density at room temperature and at atmospheric pressure is 2.26 gm/cm^3, i.e. little more than twice the density of water, and far less than most refractory materials [17]. The melting temperature of graphite is around 3950 K [17].

The electrical resistivity ρ of graphite is approximately 1–8$\times 10^{-4}$ ohm-cm when measured parallel to the basal planes and 0.2–0.4 ohm-cm when measured perpendicular to the basal planes [23]. The resistivity perpendicular to the basal planes is 100-1000 times greater than that parallel to the basal planes. For comparison, the resistivity of aluminum

is 2.73×10^{-6} ohm-cm [24], but most semiconductors have intrinsic resistivity on the order of 100 ohm-cm. Therefore graphite is a fairly good conductor and it is classified as a semi-metal. An interesting point is that parallel to the basal planes, the resistivity of graphite increases with temperature (metallic behavior), whereas the resistivity in the c direction decreases slightly with increasing temperature (semiconducting behavior). Within the planes the mean free path decreases with increasing temperature, which increases the resistivity, while the the decreased resistance perpendicular to the planes is a consequence of thermally-assisted tunneling [25–27]

1.1.2 Electronic Band Structure of Graphite

The ϕ_{2s}, $\phi_{2p}^{(x)}$ and $\phi_{2p}^{(y)}$ carbon wave functions hybridize to form three σ orbitals which form strong bonds with the three neighboring atoms [28]. The fourth electron wave function is $\phi_{2p}^{(z)}$ which is known as the π orbital. The π orbital does not hybridize on-site. It is antisymmetric under reflection through the basal plane while the σ orbitals are symmetric under reflection through the basal plane [29]. The strength of the covalent bond (σ) is around 5.43 eV/molecule while the van der Waals bond has a strength of only 0.073 eV/molecule [17].

In the Bernal structure, the energy separation between the π band and the σ bands is large enough to neglect the effect of σ electrons on the band structure near the Fermi energy. The in-plane bonds (first three wave functions) do not contribute to the conduction or play any role in transport (including tunneling). The fourth $\phi_{2p}(z)$ wave function plays a significant role in the conductivity of graphite [30].

The first Brillouin zone is bounded by six vertical planes of π/a distance from the center of the axis, which forms a hexagonal cylinder. The Fermi surface of a single graphene plane consists of only six points corresponding to the corners of the hexagonal first Brillouin zone. Figure 2(a) shows the 2D Brillouin zone which is generated from the reciprocal lattice plane. The reciprocal lattice vectors are expressed as:

$$\vec{b_1} = 2\pi\left(\frac{-1}{\sqrt{3}a}, \frac{1}{a}, 0\right) \Longrightarrow |\vec{b_1}| = \frac{4\pi}{\sqrt{3}a} \tag{1}$$

$$\vec{b_2} = 2\pi\left(\frac{-1}{\sqrt{3}a}, -\frac{1}{a}, 0\right) \Longrightarrow |\vec{b_2}| = \frac{4\pi}{\sqrt{3}a}, \tag{2}$$

$$\vec{b_3} = 2\pi\left(0, 0, \frac{1}{c}\right) \Longrightarrow |\vec{b_3}| = \frac{2\pi}{c}. \tag{3}$$

The 3D Brillouin zone of graphite is shown in Fig. 2(b). The height of the lowest zone is $2\pi/c$ and the boundaries at $\pm\pi/c$ correspond to Bragg reflection with a wavelength of $2c$. The Fermi surface is located near the HKH and $H'K'H'$ edges of the Brillouin zone. Portions of the Fermi surface are centered on each of K and K' points. At each point there is a central pocket of holes, surrounded by two smaller pockets of electrons centered at the neighboring H or H' points [30].

The volume of the Brillouin zone is $16\pi^3/\sqrt{3}a^2c$. For a crystal of volume NV_c (where $V_c = \frac{\sqrt{3}}{2}a^2c$ is the volume of a primitive unit cell), the Brillouin zone contains $2N$ states. For a single hexagonal layer (graphene), at absolute zero temperature, the hexagonal zone will be completely filled and the next zone will be completely empty but at higher temperature there will be some thermal flow into the outer zone [25] and for that reason graphite is a semi-metal with zero activation energy at absolute zero.

Graphene, which is a one monolayer sheet of graphite, is considered to be a zero-gap semiconductor [31]. It has conducting states at Fermi energy E_F only in specific directions in momentum space, at the corners of the two-dimensional Brillouin zone as shown in Fig. 3b. This unique electronic structure is the basis of nanotube electronic structure [32–35]. When a graphene sheet is wrapped into a cylinder, it will form a carbon nanotube (CNT), which will be either semiconductor or metallic, depending on the chirality of the wrapping [36]. The two main carbon nanotube types are shown in Fig. 3. The armchair CNT, which is a metallic CNT, and a zigzag CNT, which is a semiconductor CNT. The length of CNTs are usually over 1 μ m and its diameters range from 1 nm to 30 nm.

The band structure of a Bernal hexagonal graphite is dominated by the 2D in-plane interactions. There are four atoms per unit cell in graphite and there are 16 energy bands without considering the spin. There are 12 σ-bands and 4 π-bands. Half of the σ are

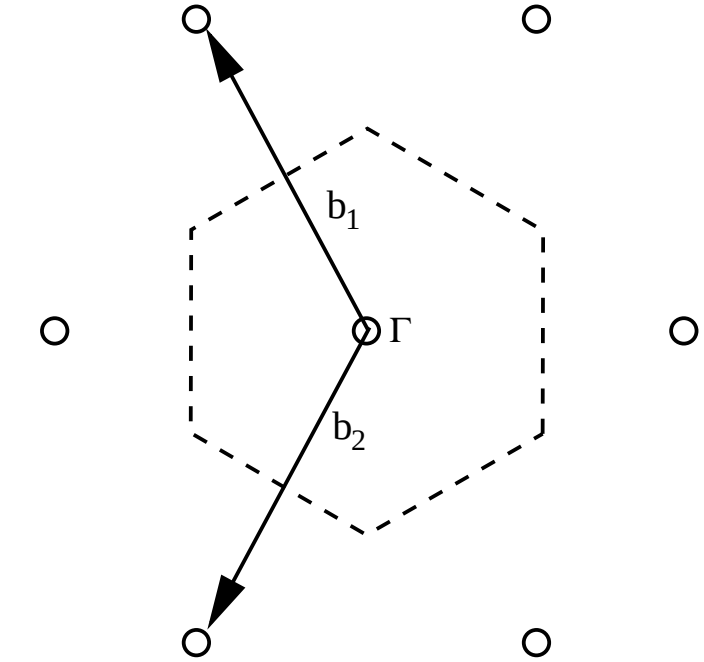

(a)

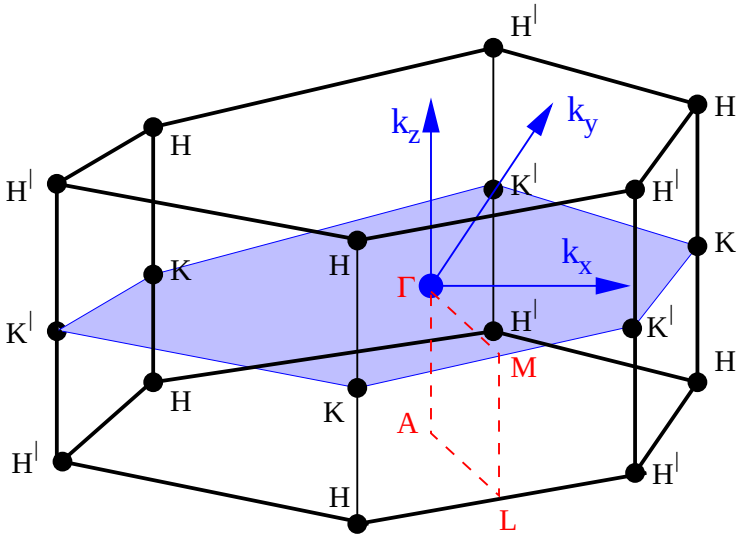

(b)

Figure 2: (a)The two-dimensional Brillouin zone of hexagonal graphite. The first Brillouin zone is indicated by the dashed line. (b) The three dimension Brillouin zone of graphite.The electron and hole Fermi surface are located in the vicinity of the edges of HKH and $H^{'}K^{'}H^{'}$.

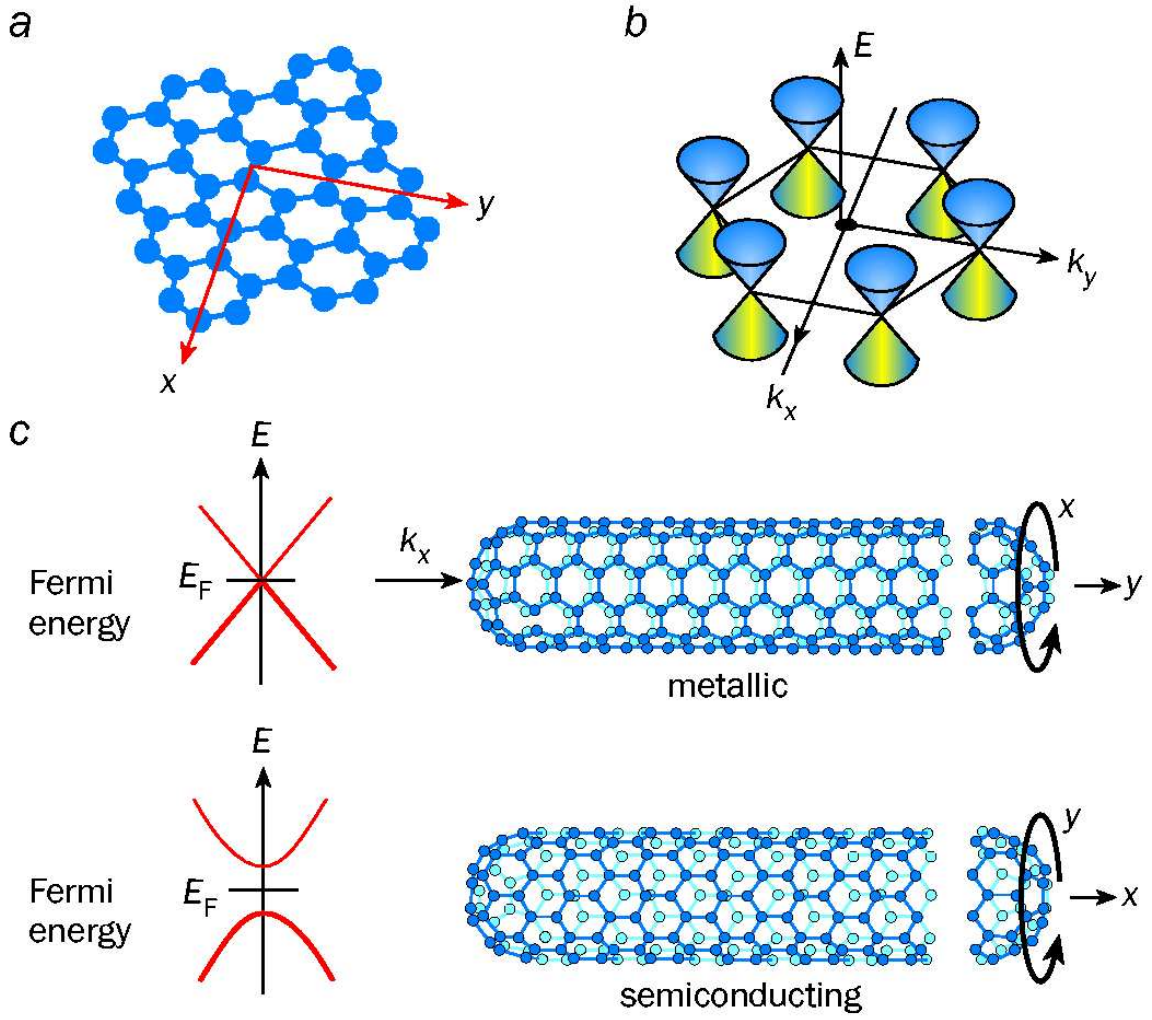

Figure 3: (a) The lattice structure of graphene. (b) The energy of conducting states as function of the wave vector k. (c) Metallic carbon nanotubes and semiconductor carbon nanotubes. The figure is taken from Ref. [37].

bonding and the other half are anti-bonding which exist at higher energies. The bonding and anti-bonding of the σ-bands are separated by approximately 5 eV [38]. The π-bands lie between these two groups of σ-bands. Two of the π-bands are bonding (π-energy) and the other two are anti bonding (π^*-energy). The upper π^* and lower π band are degenerate at K points through which the Fermi energy passes and therefore the π band forms the valence band while the π^* forms the conduction band. The σ bands are full and they cannot play any role in the conductivity of graphite.

The Fermi level is located 3.8 eV below unoccupied states [39]. The bottom of the occupied σ band is located $\sim$ 20 eV below the Fermi level and the energy splitting in the degeneracy of this band is around 0.3 eV [20]. The top occupied σ band is slightly more than 3 eV below the Fermi level and the energy splitting is roughly around 0.1 eV. The bottom of the π bands is located 9 eV below the Fermi level and the energy splitting in the π is around 2 eV which is much larger than the energy splitting of the σ bands. This huge energy splitting in the π band is due to the interaction of the interlayer. The π band at the Γ point has a strong dispersion and as result the wave function in this band has a maximum density in the direction perpendicular to basal plane. The σ bands have small or no dispersion but the π bands show a dispersion in band structure for hexagonal graphite [40, 41]. The interaction of the A atoms (full circles in Fig. 1) with the adjacent planes causes dispersion, but for B atoms (open circles in Fig. 1) have very small dispersion. The first unoccupied σ band is located around 4 eV above the Fermi level. Therefore the band near the Fermi level plays a very dominant role in transport of electrons in graphite

1.1.3 STM Image and Spectroscopy

The scanning tunneling microscope (STM) was invented in early 1980's by Binning and Rohrer[43]. Many researchers have exploited this wonderful instrument in studying the topography and electronic structure of different materials. STM has also a potential to study the mechanical properties of the surface of the sample via conductance measurements [44].

STM is based on the interaction of atoms separated by a thin vacuum gap, so that

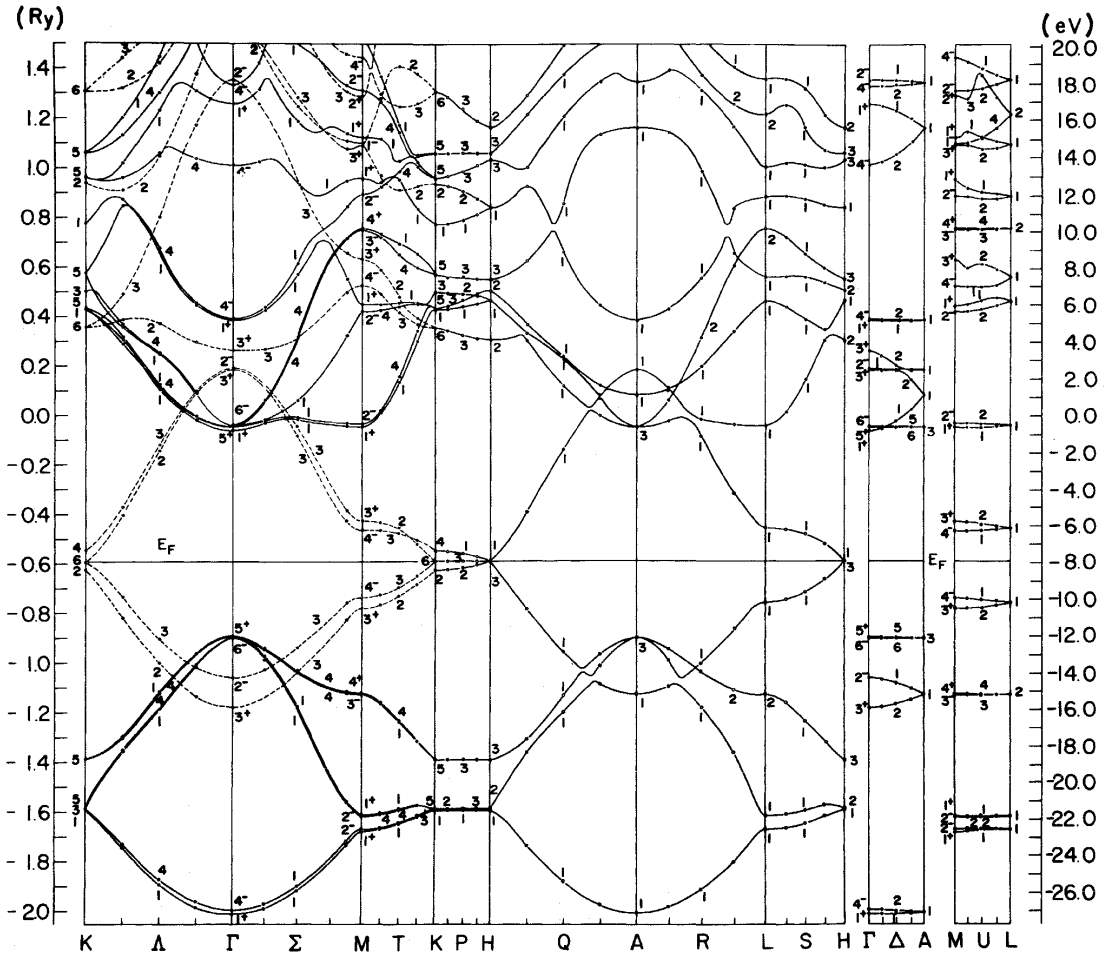

Figure 4: The band structure of 3-dimensional graphite (Bernal crystal structure) taken from Ref. [42]. The solid line and dashed line represent the σ and the π bands respectively.

electrons can tunnel from a very sharp metallic tip to or from the sample surface. The tunneling current depends on the tip-sample separation d as in equation 4 which shows that the tunneling current decays exponentially with d [45].

$$I \propto e^{-2\kappa d}, \tag{4}$$

where κ is the inverse decay length and it is expressed as:

$$\kappa = 2m(V_B - E)/\hbar^2, \tag{5}$$

with V_B the potential energy within the barrier and E is the energy of the state.

Most STM's work at constant current and depending on the topography of the sample the tip moves into or away from the sample to maintain constant current. The movement of the tip is controlled by piezoelectric drivers. For a positive tip voltage, electrons will be transferred from the sample to the tip but for negative tip bias voltage, electrons will be transferred from the tip to the sample.

1.1.4 Imaging and spectroscopy of HOPG

The surface of graphite has been imaged many times using STM and in most of the STM image only three of the six carbon atoms are observed. The STM images revealed many unusual features [46–51] such as asymmetry in the apparent height, large atomic corrugation etc. In STM images of graphite at low bias voltage, only half of the atoms are normally visible because the B site electrons have the higher density of states near the Fermi energy and for this reason the images at low voltages show the locations of B atoms [52, 53]. At higher bias voltages both the B and A atoms are visible in the STM images because the STM probes states lying farther below the Fermi energy. One can see directly the interactions between atoms in adjacent planes leads to dispersion, and how the dispersion spreads out the density of states.

Figure 5 shows an STM image of HOPG [54] with the A and B atoms are indicated in the image. The profile of the atoms are shown below the image.

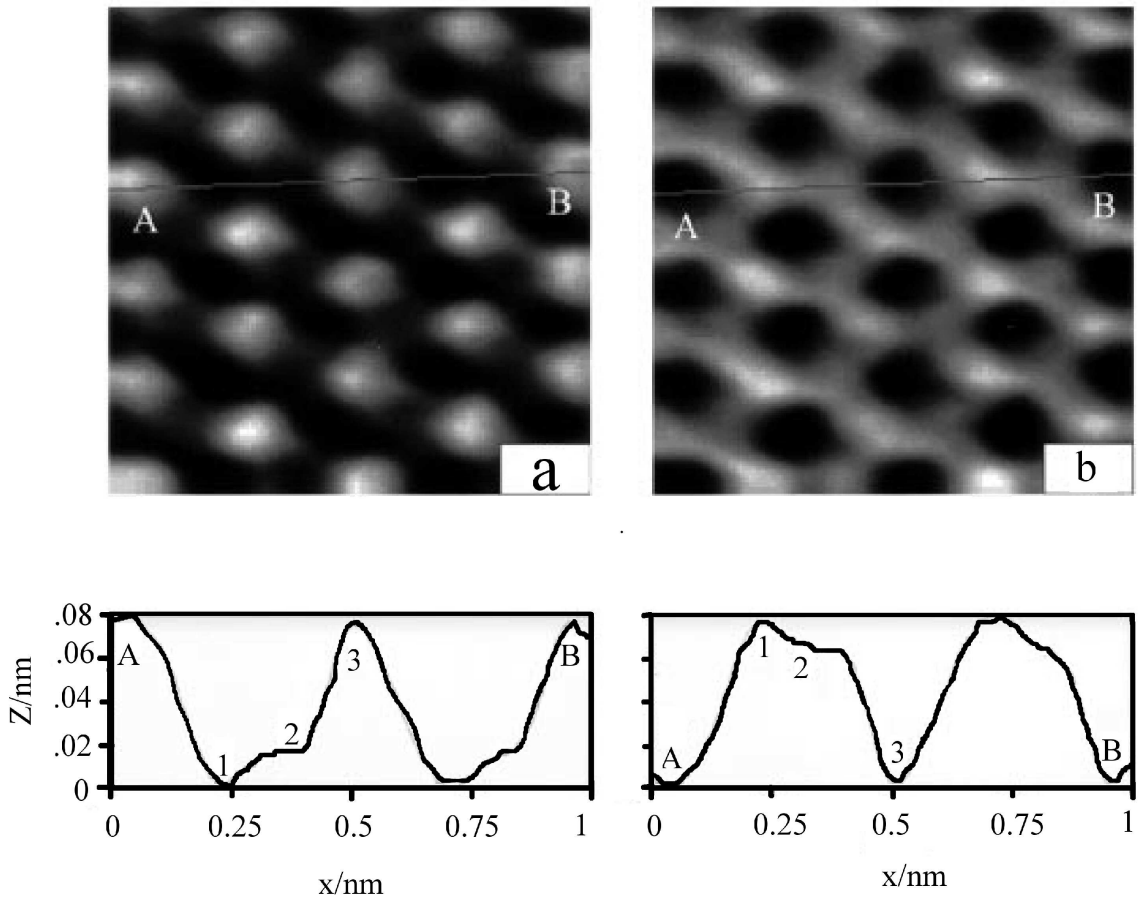

Figure 5: STM image of HOPG (10 Å× 10 Å), taking at 0.2 V bias voltage. The A and B atoms are labels in the image and the height profile is also shown below the images. The figure taken from Ref. [54].

We used a highly oriented pyrolytic graphite (HOPG) sample for all of our experiments. The graphite was cleaved in air and transferred to the UHV chamber immediately. The HOPG was annealed about 1000 C in UHV for half an hour to remove surface contamination. A sample graphite image was taken by our STM at room temperature and it is shown in Fig. 6(a). This atomic resolution image was taken at tunneling current 100 pA and tip bias voltage 0.1 V. The image was obtained by a tungsten tip. The profile of the atoms are shown in Fig. 6(b). The distance between the two bright spots (lattice constant a) is around 2.5 $\mathring{A}$ which agrees with values in the literature. The white spots are the B atoms and the black spot are the A atoms in the image. The A and B atoms are geometrically identical for a normal graphite surface but the B atoms have a higher intensity than the A atoms in most STM images. This difference in the intensity is due to the ABAB stacking of the graphite layers, that is for the B atoms there are atoms in the underneath layer but for A atoms, there are no atoms in the underneath layer. The B atoms have a higher density of states as compared with A atoms, and as a consequence they are brighter in STM images.

The $I(V)$ spectroscopy of graphite is shown in Fig. 7(a) and its numerical derivative is also shown in Fig. 7(b). The dI/dV is calculated numerically from the $I(V)$ characteristics which is obtained with a set current 100 pA and bias voltage 1 V.

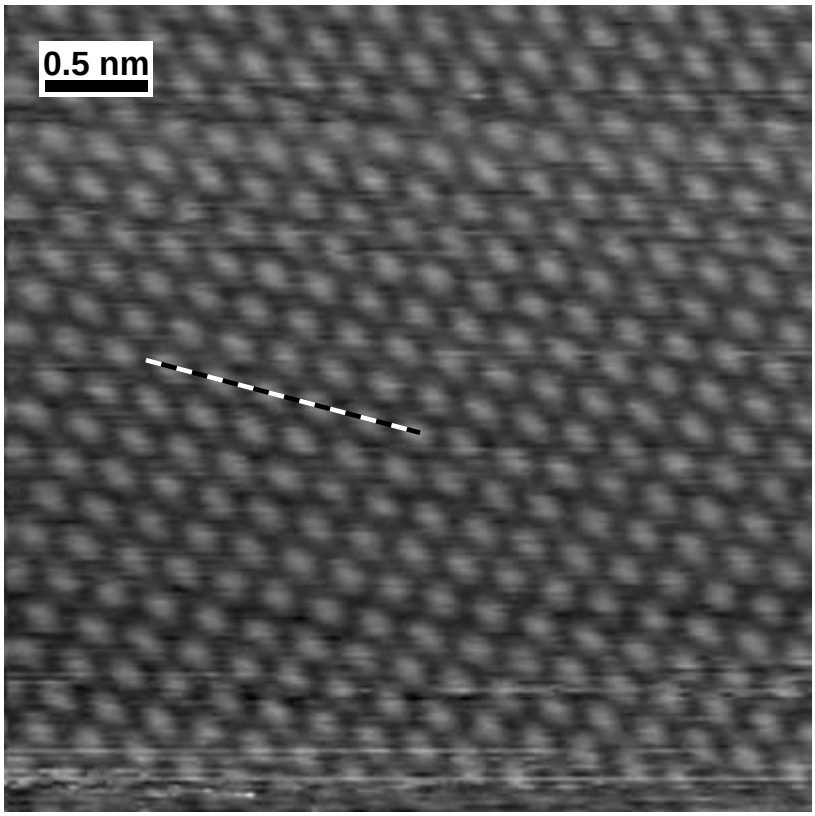

(a)

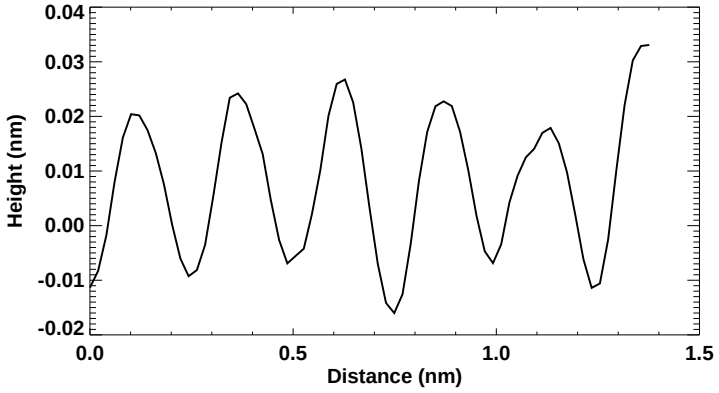

(b)

Figure 6: (a) Atomic scale STM image (50 Å × 50 Å) of HOPG ($V_{sample} = 0.1\ V$, $I = 100\ pA$) at room temperature. Data is unfiltered (unprocessed). The mean surface corrugation is 0.31 Å peak to peak. Slight distortion from hexagonal symmetry is due to thermal drift of the STM tip. (b) Height profile of the atoms across the marked segment in the image.

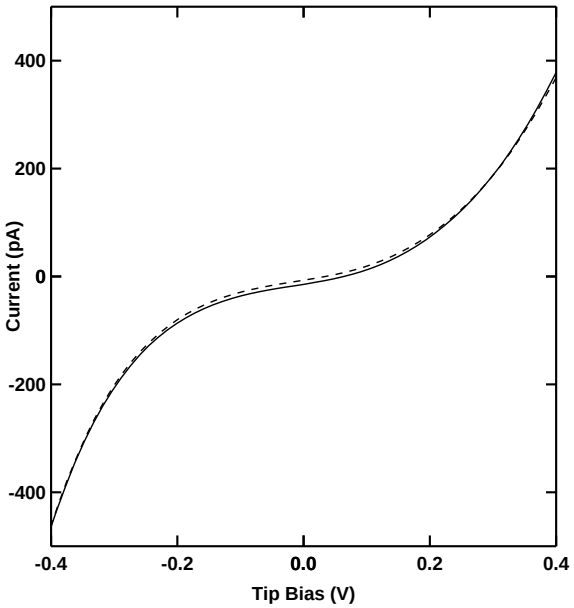

(a)

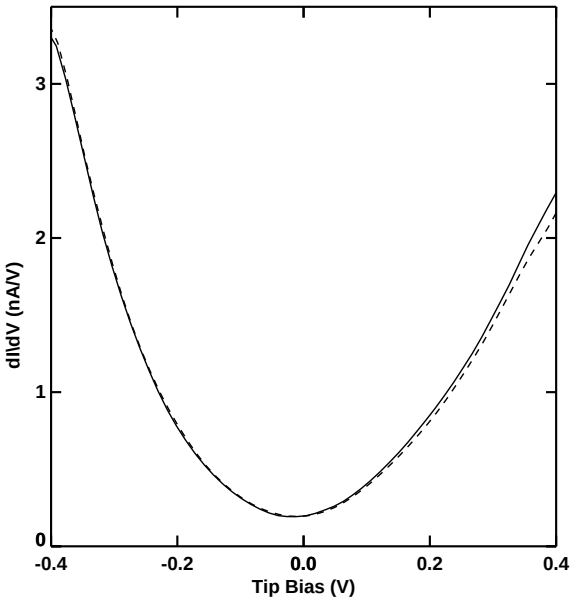

(b)

Figure 7: The $I(V)$ spectrum is the average of 2601 $I(V)$ spectra acquired at different positions on an x-y grid within an area of 5 Å X 5 Å. (a) Tunneling spectroscopy of graphite at room temperature (b) Numerical derivative of the spectra shown in (a) (tip voltage = 0.2 V and set point tunnel current = 100 pA).

1.2 Review of Conductance

1.2.1 Point Contact Conductance: Theory

The transition from the tunneling regime to a point contact is the starting point for studying contact conductance [14, 55–58]. At the initial approach of the tip toward the surface of the sample the force is an attractive force and the resistance between the two junctions is very large. As the tip nears the surface, the resistance of the gap decreases and the force between the two surfaces becomes repulsive. This force deforms the surfaces. When the force between the tip and sample changes from attractive to repulsive, the potential barrier between the two junctions collapses and it transforms from the tunneling regime to the contact regime [59] .

When a metallic tip is brought toward a metallic surface with very small contact area a "point contact" is established between the two surfaces. For normal metallic contacts the relation between voltage and current is linear according to Ohm's law but for a point contact, where the contact radius is less than the mean free path of the electrons, the $I(V)$ relation is not linear [7]. For point contact conductance, the conductance is ballistic and electrons are transferred across the junction due to the electric field caused by the bias voltage.

Maxwell studied the diffusive regime between two contacting surfaces. Maxwell conductance G_M is valid for $l \ll a$ (where l is the electron mean free path and a contact radius) and the conductance G_M is given by [60]

$$G_M = \frac{2a}{\rho}, \tag{6}$$

where ρ is the resistivity of the metal, given by

$$\rho = \frac{p}{Ne^2 l}, \tag{7}$$

where p is the Fermi momentum and N is the electron density. This resistance sometimes is known as the spreading resistance or diffusive resistance. The Maxwell conductance scales linearly with contact radius.

Electrical contact between the two surfaces is defined when the electrons from one of the surface pass freely to the other without any potential barrier. The relationship between

contact resistance and contact area in the ballistic regime ($l \gg a$) was proposed originally by Sharvin and today is known as the Sharvin conductance. Sharvin's original contact resistance is given by [61]

$$R = \frac{p}{e^2 D^2 N}, \tag{8}$$

where D is the contact diameter.

The most common expression of Sharvin conductance in the literature is given by [62–66]

$$G_s = \frac{3\pi a^2}{4\rho l}. \tag{9}$$

Since the resistivity ρ is inversely proportional to l from equation 7, the Sharvin conductance does not depend on the mean free path l, in contrast to G_M (as long as $l \ll a$).

The semi-classical Sharvin conductance can be expressed in terms of the quantum conductance ($2e^2/h$) as

$$G_s = \frac{2e^2}{h}\pi\frac{A}{{\lambda_f}^2}, \tag{10}$$

where A is the contact area and λ_f is the Fermi wavelength.

From a semi-classical analysis of contact conductance for a constant cross-section wire, the Sharvin conductance is modified to include the perimeter of the cross-section of the wire and the conductance is given by [67]:

$$G_c = \frac{2e^2}{h}\left(\pi\frac{A}{{\lambda_f}^2} - \alpha\frac{P}{\lambda_f}\right), \tag{11}$$

where P is the perimeter of the cross-section and α is a correction factor. When the work function ϕ goes to infinity the factor α goes to 0.5 [66] and as ϕ/E_f decreases the correction factor decreases and approaches the classical Sharvin limit (α=0).

For the regime between Sharvin and Maxwell, Wexler expressed the contact resistance as [68]

$$R = [\frac{4}{3\pi}\frac{\rho l}{a^2} + \gamma(l/a)\frac{\rho}{2a}], \tag{12}$$

where a is the radius of contact and γ is a slowly varying function of l/a, with $\gamma(0) = 1$ and $\gamma(\infty) = 0.694$. For $l \gg a$ (the Sharvin limit) the electrons are ejected ballistically into the metal.

1.2.2 Nanowire Conductance: Theory

For two dimensional electron gas (2DEG), the conductance G is given by the Landauer formula [69]

$$G = \frac{2e^2}{h} \sum_m \sum_n T_{mn}, \tag{13}$$

where T_{mn} is the transmission probability of the sub-band mn and the sum runs over the total number of occupied sub-bands. For perfectly transmission ($T = 1$), the conductance is an integer multiple of the quantum conductance ($G_o = 2e^2/h$). In the cross-section of the nanowire, the transverse motion is quantized. There are a finite number of electronic modes below the Fermi energy E_F which can be transmitted through the wire. When the cross-section area increases, higher order transverse modes propagate one by one and the conductance increase by integer multiple G_o at each transient opening of a new mode.

1.2.3 Point Contact Conductance: Experiment

Atomic contact starts with an area of atomic dimensions. Non-destructive tip contact on a graphite surface was done first by Soler et al. [70]. This non-destructive contact between surfaces which might deforms elastically is the basis for atomic force microscope (AFM) with repulsive forces between the two surfaces.

For atomic contacts between metals, the resistance is of the order of the resistance quantum for the Sharvin case. If the density of states is constant around the Fermi level, then the atomic (point) contact is independent of the applied voltage [57] but for many materials their density of states is not constant around the Fermi level (e.g. graphite),and the contact resistance depends on the applied voltage.

The transition from tunneling to point contact was also studied by Gimzewski and Moller [56]. They made a contact experiment between a clean Iridium tip and polycrystalline Ag surface. They observed a region of metal-vacuum-metal tunneling for $\Delta z > 4$ $\mathring{A}$. They evaluated the initial contact radius from the Sharvin resistance expression and radius of

found about 1.5 $\AA$ with a contact resistance $\sim$ 10 $k\Omega$. This contact area is equivalent to a few atoms in close contact. They observed a significant hysteresis for $\Delta z > 5$ $\AA$ and suggested that in this range adhesion occurred between the tip and sample. The image taken after the contact experiment did not show a significant change of the Ag topography from the image taken before the contact. The authors concluded that the contact between these two surfaces may involve plastic or elastic deformation but that any deformation damaged must anneal within a short time for these small tip displacement (a few angstroms).

Holm [17] has given a relation for Joule heating in a point contact by using the Wiedemann-Franz law

$$\kappa\rho = TL, \tag{14}$$

where L is the Lorenz number. For the Maxwell limit for an applied voltage of 10 mV, this is equivalent to an increase of 2 K in temperature [65]. This will not be the main reason for decreasing the electron mean free path. Erts et al. [65] have done experiments to test the heating effect on Au wire. For an applied voltage up to 140 mV the $I(V)$ curves were linear. They concluded that the scattering is mainly due to fixed scattering centers, and not due to thermal scattering, which would increase at higher power level. The $I(V)$ curves should show some nonlinearity if the scattering were temperature (power) dependent.

1.2.4 Nanowire Conductance: Experiment

Different approaches, like the free electron model and molecular dynamics simulation [8, 66] have been explored to study the relation between the geometry and contact conductance. Perhaps the best experiment on contact conductance on Au nanowires was done by Rubio et al. [13], as shown in Fig. 8. In this experiment, they measured both the conductance and force simultaneously as functions of displacement. The experiment was done at room temperature. They understood both electrical and mechanical properties of the contact conductance from measurement of the conductance and force.

The conductance remains almost constant in the elastic stage and it is reflected in the force figure by a straight line. There are no atomic rearrangements in the elastic stage and it has a stable electronic structure. The conductance changes abruptly during the relaxation

of the force which is indicated in the force figure. The abrupt change in the conductance is due to the atomic rearrangements.

Conductance measurements of carbon nanotubes with a liquid metal contact (mercury) were done by Frank et al. [71], as shown in Fig. 9. The CNTs conduct ballistically without heat dissipation. They observed a plateau at integer multiples of Go which indicated the conductance is quantized. Other contact experiments were done by many people either between the same metal [10–12] or two different metals [62, 72–74]. In most experiments and simulations the conductance is an integer multiple of the conductance quantum ($Go = 2e^2/h$).

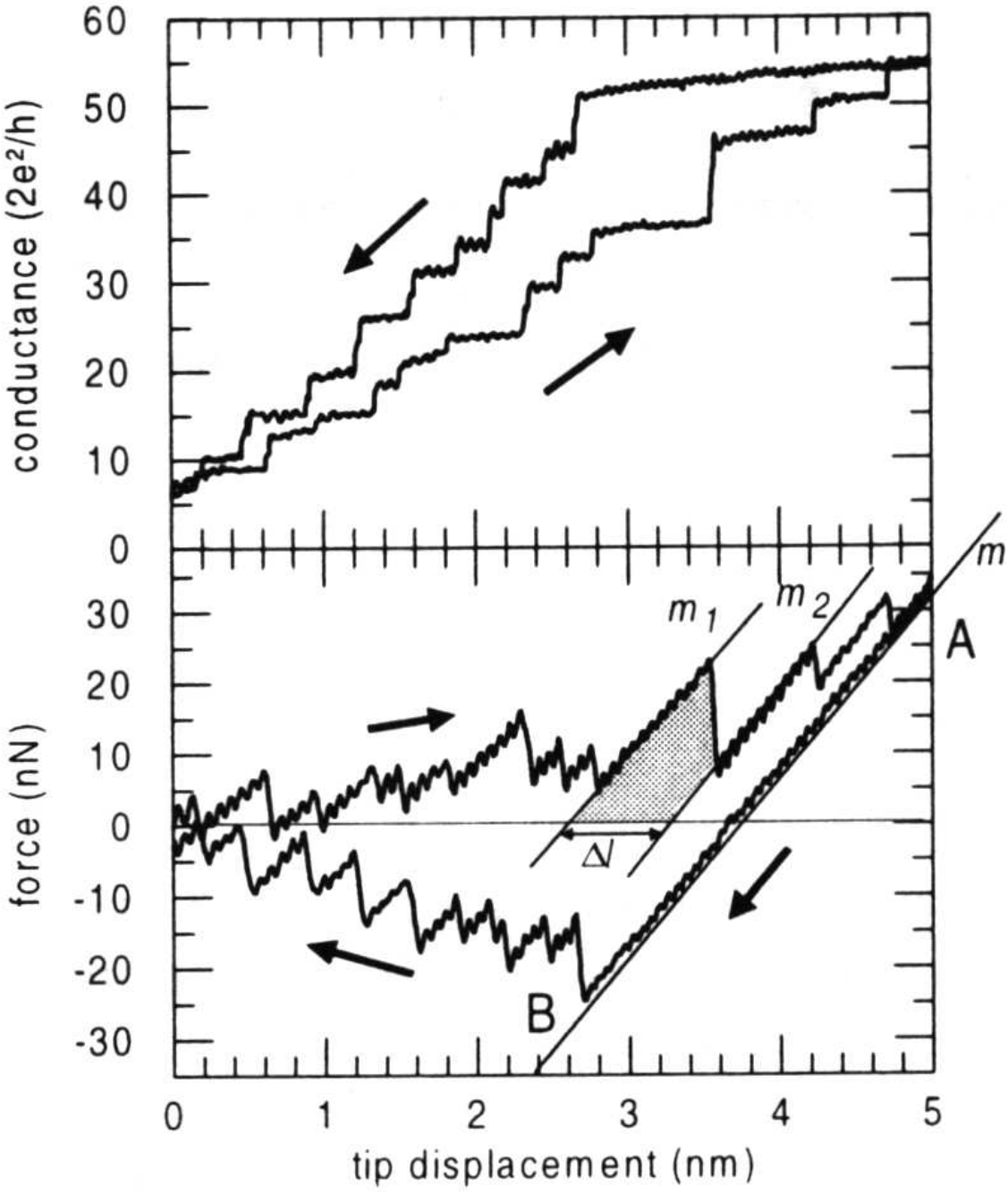

Figure 8: Simultaneous measuring of the conductance and force during compression and stretching of Gold Nanowire taking from Ref. [13]

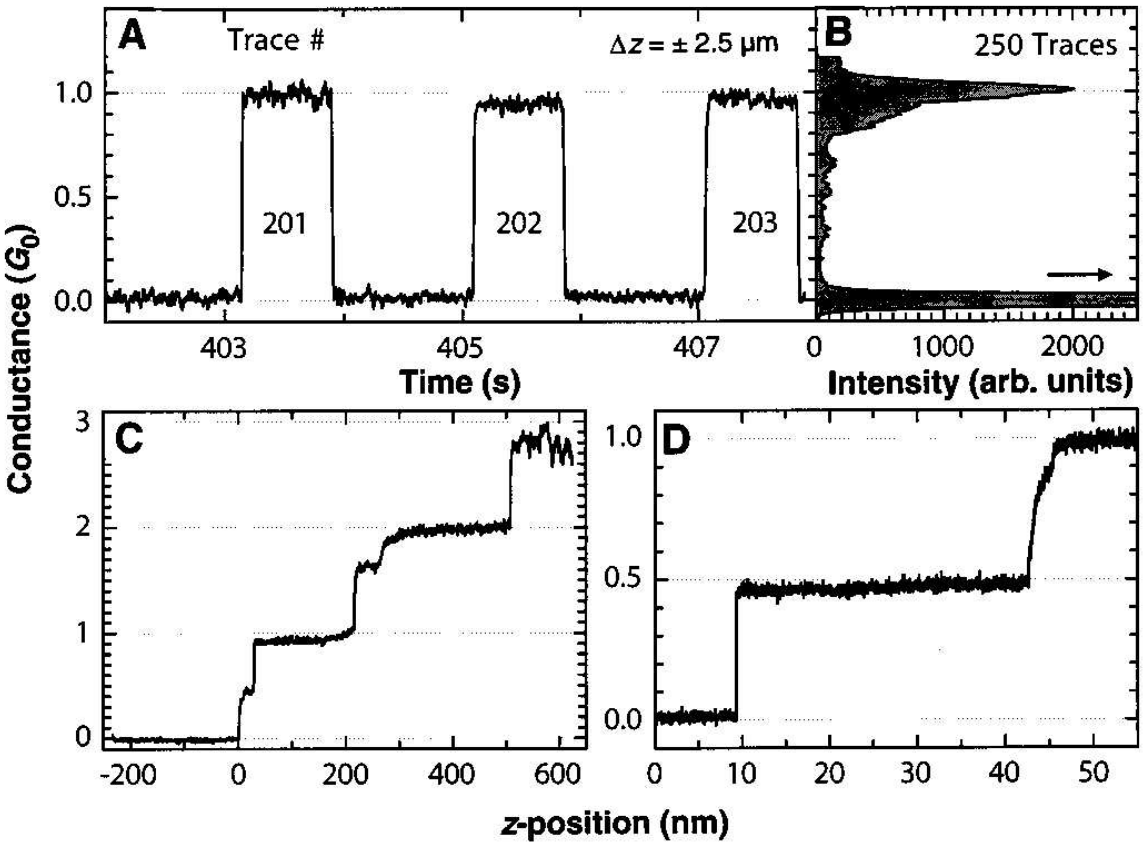

Figure 9: Conductance of carbon nanotube contact with liquid mercury and the conductance measured as function dipping depth. It is taken from Ref. [71]

1.3 Contact Mechanics Between two Surfaces

It is very important to understand the contact mechanics between two surfaces in order to understand contact conductance . As already discussed in the previous section the conductance depends on the geometry of the contacting surface (contact radius or area). The forces at the interface have a direct effect on the transport of electrons between the sample and the tip. There are several models used in estimating the forces between the two contacting surfaces. These will be presented in the following sections.

1.3.1 Hertz Theory

The most well known theory in contact mechanics is the Hertz elastic theory of contact mechanics. This theory applies for a surface with frictionless, small strains, continuous and non-conforming ($a \ll R$, a is contact radius and R is radius of curvature) [75]. Hertz theory also doesn't take into consideration the surface free energy and the adhesive force which exists between the surfaces.

Two different spheres with radii of curvature R_1 and R_2 are brought into contact as shown in Fig. 10. In general, the actual contacting interface between the two surfaces should be a curve in the plane of the page even though in the figure it is indicated by a straight line. The force applied to the system is compressive along the Z axis. The first sphere is deformed by δ_1 and the second sphere is deformed by δ_2 as indicated on the diagram. The contact radius is labeled by a in the figure and the total deformation displacement δ is expressed as:

$$\delta = \delta_1 + \delta_2. \tag{15}$$

The reduced tip-sample curvature R is given by:

$$\frac{1}{R} = \frac{1}{R_1} + \frac{1}{R_2}. \tag{16}$$

For our case the second surface is a flat surface ($R_2 \rightarrow \infty$) and the reduced curvature will be the same as R_1 (R=R_1).

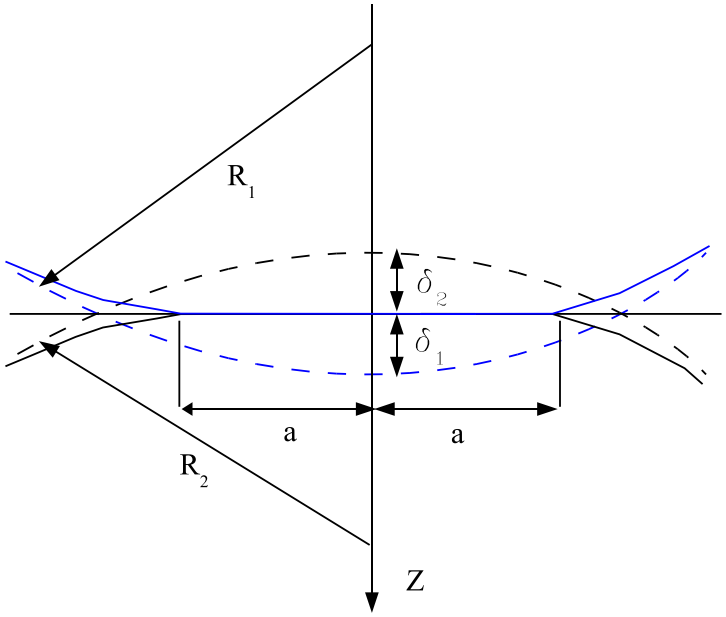

Figure 10: Illustration of the geometry used to calculated the contact radius a when two different spheres with radii of curvature R_1 and R_2 are in contact. The dashed line is the projected line before deformation and the solid line is after deformation by δ_1 and δ_2 from its original shape.

The controlling parameter in this theory is the applied load (F) to the system. The average pressure distribution in the system is given by [75]:

$$P(r) = P_o[1 - (r/a)^2]^{1/2}, \tag{17}$$

where P_o is the maximum pressure applied to the system and r is the distance from the center of the contact. The applied load can be related to the pressure by the following expression:

$$F = \int_0^a P(r) 2\pi r dr = \frac{2}{3} P_o \pi a^2 \Longrightarrow P_o = \frac{3F}{2\pi a^2} = \frac{3}{2} P_m. \tag{18}$$

As shown in the above expression the applied force is proportional to the contact area ($A = \pi a^2$) and the maximum pressure P_o is 3/2 times the mean pressure P_m. The general expression for Hertz contact force F_h between two elastics surfaces is given by [76] :

$$F_h = \frac{E^* a^3}{R} = E^* R^{1/2} \delta^{3/2}, \tag{19}$$

where E^* is the effective Young's modulus or elastic reduced modulus of the two surfaces,

Table 1: E Young modulus and ν Poisson's ratio for the metals are taken from Ref. [77], E^* effective Young's modulus between HOPG and the metals and Y Yield strength (in an annealed state). [a]Ref. [78] [b]Ref. [14].

Metal	*E (GPa)*	ν	E^*(GPa)	*Y (MPa)*
Al	70	0.345	34.84	35[a]
Cu	130	0.343	41.06	69[a]
Ga	9.81	0.5	13.05	
W	411	0.28	47.74	
HOPG	36.5[b]	0.25[b]		

given by:

$$\frac{1}{E^*} = \frac{3}{4}\left(\frac{1-{\nu_1}^2}{E_1} + \frac{1-{\nu_2}^2}{E_2}\right), \tag{20}$$

where E_1, E_2 and ν_1, ν_2 are Young's modulii and Poisson's ratios of the two materials, respectively. The elastic modulii for the interested metals are shown in Table 1.

The contact radius of a solid metal tip with a flat surface can be estimated from the radius of curvature R and deformation displacement δ [75, 79]:

$$a = (\delta R)^{1/2}. \tag{21}$$

The total force F_t for the Hertz model is same as the Hertz force F_h because the adhesive force F_{ad} is zero for this model. In the next section we will see other theories that include the attractive force between the surfaces.

1.3.2 Adhesive Force Between two Elastic Surfaces

The adhesive force (pull-off force) is an attractive force that exists between two contacting surfaces. There are several theories and models for estimating the adhesive force but we will focus on the most known ones. The two *most* well known models are the Johnson-Kendall-Roberts (JKR) [80] and Derjaguin-Muller-Toporov (DMT) [81, 82]. These two models are valid for a pure elastic deformation with a contact radius smaller than the radius of curvature of the tip [83] . Figure 11 shows the normalized force plotted as function of normalized penetration depth for different models. As shown in this figure, the JKR model

has hysteresis between the forward and reverse directions.

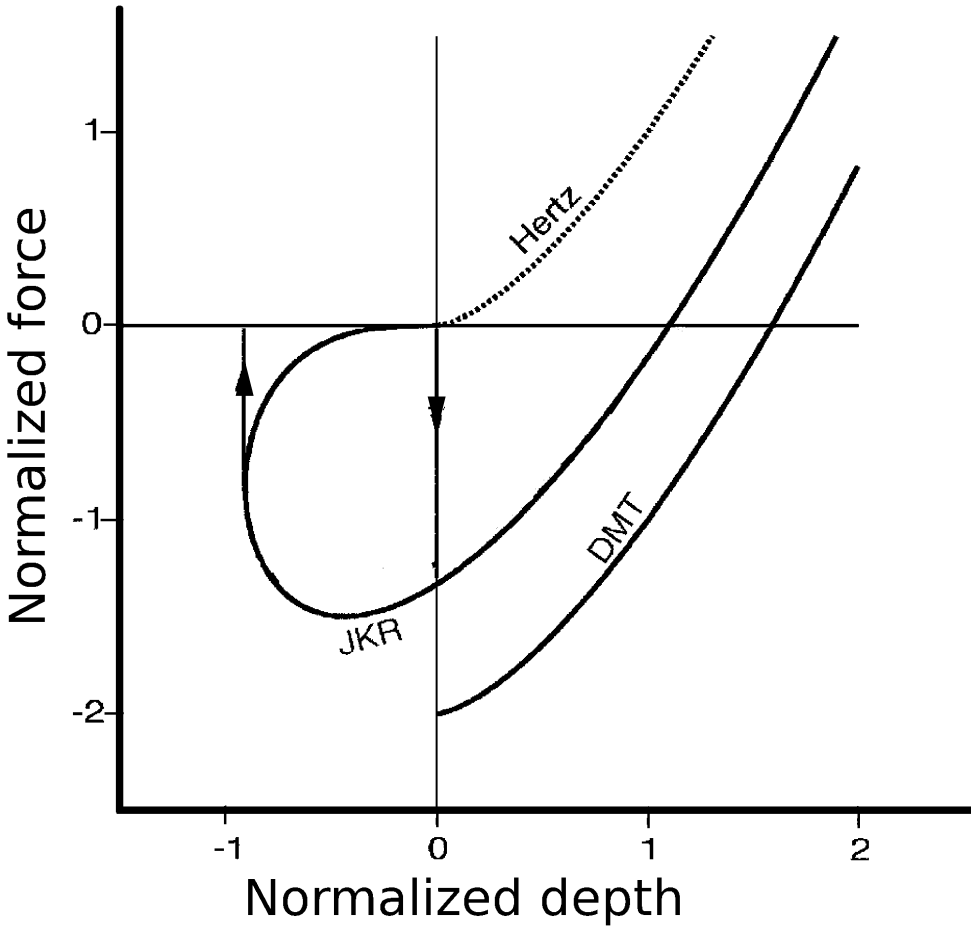

Figure 11: The figure shows the Normalized force as function of penetration depth for Hertz, JKR and DMT contact models. The JKR adhesive force has hysteresis. The diagram is taken from Ref. [84].

The work of adhesion w is the energy per unit area required to separate two surfaces from contact to infinity in vacuum and it is given by [76, 85, 86]:

$$w = \gamma_1 + \gamma_2 - \gamma_{12}, \tag{22}$$

where γ_1 and γ_2 are surface energies for the two contacting surfaces. The surface energy at the interface γ_{12} can be estimated as [85]:

$$\gamma_{12} \simeq 2\sqrt{\gamma_1 \gamma_2}. \tag{23}$$

Table 2: Surface energy (γ) and adhesive work (w) for selected metals with HOPG. The adhesive work is calculated using Eq. 22. [a]Ref. [87] [b]Ref. [77] [c]Ref. [88].

Metal	γ *(N/m)*	w *(N/m)*
Al	0.914[a]	0.39
Cu	1.285[a]	0.64
Ga	0.718[b]	0.27
W	2.5[a]	2.1
HOPG	0.11[c]	

The surface energy and work of adhesion for some metals is shown in Table 2. The work of adhesion was calculated between the surface of graphite and different metals using Eqs. 22 and 23. Gallium has the lowest adhesive work compared with other metals in the list.

The JKR model [80] assumes the adhesive force acts only inside the contact, i.e. only short range forces are considered. There is no force between the surfaces when they are not in contact.

The adhesive force F_{ad} and deformation displacement δ for the JKR model are expressed as [76]:

$$F_{ad} = (3/2\pi)Rw, \tag{24}$$

$$F_t = F_h - F_{ad} = \frac{E^* a^3}{R} - \sqrt{6\pi w E^* a^3}, \tag{25}$$

$$\delta = \frac{a^2}{R} - \frac{2}{3}\sqrt{\frac{6\pi w a}{E^*}}. \tag{26}$$

When the repulsive force is cancelled out by the attractive force the total load F_t is zero, and the contact radius a_o is given by:

$$a_o = \left(\frac{6\pi R^2 w}{E^*}\right)^{\frac{1}{3}}. \tag{27}$$

The JKR model is good for large tip radius and soft materials with large surface energy.

The DMT model [89] includes long-range surface forces that exist outside the contact area. In this model a force of adhesion exists even when the surfaces are not in contact.

The adhesive force and contact radius for DMT model is given by:

$$F_{ad} = 2\pi R w, \tag{28}$$

$$F_t = F_h - F_{ad} = \frac{E^* a^3}{R} - 2\pi R w, \tag{29}$$

$$\delta = \frac{a^2}{R}. \tag{30}$$

The contact radius a_o at zero applied load is given by:

$$a_o = \left(\frac{2\pi w R^2}{E^*}\right)^{\frac{1}{3}}. \tag{31}$$

The DMT model is good for small radius of curvature of the tip and low adhesion. The contact radius is similar to the Hertz theory which means that the tip-sample geometry is constrained to remain Hertzian.

The JKR and DMT theories are not exact and can't be applied to all materials. However, the Maugis theory [90] is the most complete macroscopic theory, and applies to all materials. The properties of the material are described by a dimensionless parameter λ, given by:

$$\lambda = \frac{2.06}{Z_o}\sqrt[3]{\frac{R w^2}{\pi E^{*2}}}, \tag{32}$$

where Z_o is the equilibrium separation distance between the tip and the surface.

The JKR model is the $\lambda \to \infty$ limit of Maugis theory, while the DMT model is obtained as $\lambda \to 0$. The transition from the DMT model to the JKR module is developed by Maugis and Dugdale (MD). The set equations relating F, δ, a, m and λ are [90]:

$$F = \frac{E^* a^3}{R} - \lambda a^2 \left(\frac{\pi w E^{*2}}{R}\right)^{1/3} \left[\sqrt{m^2 - 1} + m^2 \arctan\sqrt{m^2 - 1}\right] \tag{33}$$

$$\delta = \frac{a^2}{R} - \frac{4\lambda a}{3}\left(\frac{\pi w}{R E^*}\right)^{1/3}\sqrt{m^2 - 1}, \tag{34}$$

where m is the ratio of the width of annular region to the radius of contact. The annular region is the outer radius at which the adhesive force no longer acts in the gap between the

surfaces. Practically speaking, the MD theory shows that the JKR model is valid for $\lambda \geq 5$, while DMT is useful for $\lambda \leq 0.1$.

For the experiment described in this Thesis, the maximum equilibrium separation distance Z_o between the tip and the surface can be approximated as the interlayer separation distance between graphite layers, which is 3.35 $\mathring{A}$. For all cases of interest, $\lambda \ll 0.1$. Therefore, we will use the DMT model in the analysis of our experiments. The DMT model is without hysteresis in the force versus penetration depth but in the JKR model, hysteresis in the force versus displacement exists between pushing and pulling of the tip from the sample surface.

CHAPTER II

EXPERIMENTAL SET UP AND PROCEDURE

2.1 UHV Chamber and Vacuum System

All experiments were done in ultrahigh vacuum (UHV) at or near room temperature. The room temperature STM is in a vacuum chamber with a base pressure around 1×10^{-10} *mbar*. A photo of the UHV chamber is shown in Fig. 12. For a detailed description of the UHV chamber see P.E. Quesenberry, Ph.D. Thesis [91]. In brief, the UHV chamber is equipped with Low Energy Electron Diffraction (LEED), Auger Electron Spectroscopy (AES), Field Emission Microscope (FEM), STM, electron-beam (e-beam) sample heater and e-beam tip heater.

The UHV chamber was pumped by a turbo-molecular pump [92] and an ion pump [93]. The turbo pump was operated during transfer of tips and samples and also during baking of the chamber. We turned off the turbo pump during our experiment because it could potentially introduce vibrational noise to the chamber that would affect the experimental measurements. The ion pump operated continuously since it doesn't introduce any vibrational noise. The only time we closed the valve of the ion pump from the main chamber was during sputtering of tips when we leaked Ne gas into the chamber. The ion pump is not able to pump Ne gas efficiently, so we used the turbo pump to pump out the Ne gas.

The chamber normally has water vapor and gases that stick on the wall of the chamber and can not be pumped out by our pumps. This makes the pressure of the chamber high. To achieve UHV pressure the chamber should be baked to desorb water and other condensed gases. We normally baked the chamber around 145 ^oC for 24 hours with the pumps running to achieve UHV pressure. We out-gassed all the filaments inside the chamber while the chamber was hot.

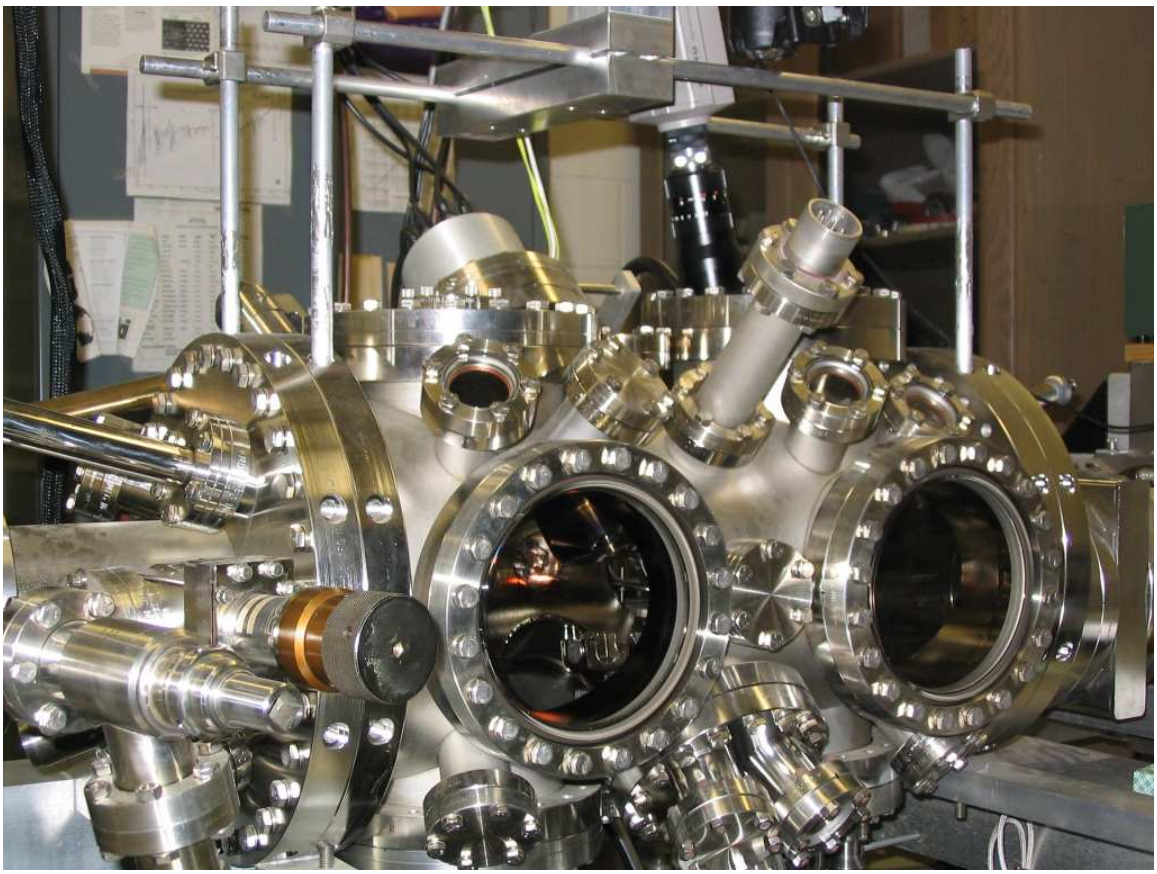

Figure 12: The UHV chamber.

Some modification was made to the existing in-vacuum current to voltage amplifier which was connected to the sample by a small Cu wire. This amplifier has a fixed conversion factor 10^8 V/A and was not suitable to measure currents in the entire range from 1 mA to 1 pA. The servo setpoint current was determined by the amplifier gain. A DL Instruments model 1211 [94] external adjustable sensitivity was used for most of the experiments. A switch was mounted with epoxy on the top of the existing amplifier. The switch allows us to bypass the amplifier in order to use a current amplifier outside the chamber. A wobble stick was used to turn on or off the switch while the chamber was under vacuum. We put also a thermocouple wire near the STM scanner to monitor the temperature of the liquid tip.

2.2 Sample Preparation

The graphite (HOPG) sample used for this work was bought from Spi company [95]. The original size of the sample was $10 \times 10 \times 1$ mm but the thickness of the graphite decreases

due to cleaving the sample from time to time. The sample was cleaved in air using adhesive tape to peel several layers, and immediately transferred to UHV to minimize exposure to the air. The sample was annealed by the electron bombardment (e-beam) sample heater at temperature $\sim$1000 ^oC for 30 min. to clean from surface contamination. This temperature required typically 4 A of filament current at 0.5 kV accelerating potentials. The temperature of the sample was measured by an optical pyrometer. The optical pyrometer is a device which allows contactless temperature measurement by using incandescence color matching. The optical pyrometer is good for temperatures greater than 600 ^oC.

2.3 Tip preparation

In the experiments, both liquid and solid metal tips were used for the contact conductance measurements. In each case, the contact area can be varied by pushing the STM tip further into the graphite sample. The liquid will exert far less pressure than solid tips, and thus will only minimally disort the graphite surface. Gallium (Ga) was used for a liquid metal tips. Copper and aluminum were used as solid metal tips.

2.3.1 Liquid metal tip

Gallium was chosen as the liquid metal for the following reasons:

• It will form a liquid easily around 30 ^oC.

• It doesn't wet in microscopic scale [96].

• It has very low vapor pressure (9.31×10^{-36} Pa at 303 K [97]) even at high temperature, which is essential in UHV.

The other metal which forms a liquid at low temperature is mercury (Hg) but it is not compatible with UHV because of its high vapor pressure (0.0002 Pa at 234 K [97]). Therefore, we didn't use Hg for our experiments even though some contact experiments were done previously between Hg and carbon nanotubes at room temperature in air [98].

Approximately 0.2 cm^3 melted Ga was placed on small stainless-steel dish and the oxide layers of the Ga drop were scraped. The Ga drop was transferred immediately to the load-lock chamber to minimize further exposure to air. After transfer to the UHV chamber, a flat sheet of stainless-steel mounted on a 1 mm tungsten rod was used for further scraping

of the oxide layer from the Ga drop by using the wobble stick. The Ga was then annealed at about 300 ^oC inside the chamber and the Ga drop surface was scraped again to remove any remaining oxide.

A 1 mm Cu rod was cleaned by electron bombardment heating before dipping into the liquid Ga. The dipped end of the Cu rod sometimes etched or stretched to achieve a smaller cylider radius and hence a smaller Ga drop radius. The clean Cu rod approached the liquid Ga for dipping via a Burleigh inchworm motor [99]. This process was monitored by a camera video with 12X maginication. When the Cu rod made contact with the liquid Ga, we observed a clear jump to contact in video image. This was an indication that the liquid Ga was free of oxide contamination. Even a very thin oxide skin was dperessed slightly by the Cu rod before the Ga wetted the rod. The Cu rod was left in contact with the Ga for up to 30 minutes. We also observed a jump on the monitor when contact broke during the process of removing the Cu rod from the Ga drop.

The radius of curvature of the Ga drop-tip was measured from the magnified image of the tip which was taken by a digital camera. The 1 mm Cu rod was taken as a reference and we fitted a circle to the curvature of Ga drop to measure the radius of curvature R_{Ga} of drop.

2.3.2 Solid Metal Tips

0.125 mm Cu and Al wires with purity 99.99% were used as a solid metallic tips in the contact experriments. The solid tips were etched by electro-chemical methods. We used orthophosphoric acid solution (70% orthophosphoric acid in water) for etching the Cu tip with an AC voltage between 1-5 V. We used perchloric acid solution (10% perchloric acid in methanol) for etching the Al tip with an AC voltage between 1-10 V (smaller volatge is for smaller tip radius) [100]. We transferred the tips to our chamber and we expected oxides on the tips. Therefore, it required cleaning procedure in vacuum before the contact experiments. We used a sputtering technique [101, 102] for cleaning and sharpening the tip further. Ion sputter is standard technique used for tip and sample preparation. We used Ne gas for the sputtering of the tips.

We leaked Ne gas to the chamber and the pressure the chamber increases. The pressure of the chamber with Ne gas was between 6.6×10^{-6} to $2 \times 10^{-5} mbar$ for most of the tips. We set the emission current to a fixed value (for most of the tips 5 to 20 μA) and the tip was connected to negative high voltage. The high voltage was increased until the emission current reached its setpoint. We then monitored the voltage of the tip with a voltmeter until it dropped to a minimum possible voltage (the voltage would decrease and increase cyclically, with the minimum voltage increasing slightly on each cycle). The smaller the minimum sputtering voltage of the tip, the sharper is the tip. With this method, we cleaned the tip from oxide and at the same time sharpened the tip further. We switched the high voltage polarity to positive for annealing the tip by electron bombardment heating. Most of the tips were annealed at 1-1.5 kV with about 1.3 mA emission current for about 20-45 seconds.

The next step was to measure the radius of the tip. We used the field emission microscope (FEM) to do so. FEM was invented by Erwin Mueller in 1936 [103]. This instrument allows us to view the surface of the tip and at the same time you can follow the rapid changes on the surface of the tip. The schematic diagram of the FEM is shown in Fig. 13.

By applying negative high voltage to the tip, electrons were emitted from the surface of the tip to the direction of the screen. A micro-channel plate (MCP) [104] was placed in front of the phosphor screen to amplify the emitted electrons from the tip. A MCP is a detector consisting of two channel-plates, with one connected to ground and the other to 950 V to established a multiplication of the emitted electrons. The phosphor screen was held at 3 kV.

The emission current was very small, of the order of nA, and the ammeter of the power supply was not sensitive enough to measure nA current. We put a 10 MΩ resistance in series to the cable of the high voltage (HV) which was connected to tip. We were able to measure the voltage drop V_D across the resistor and from this we were able to measure the emission current ($I = V_D/10\ M\Omega$) of the tip. We measured the emission current of the tip as a function of applied voltage for the measurement of the tip radii.

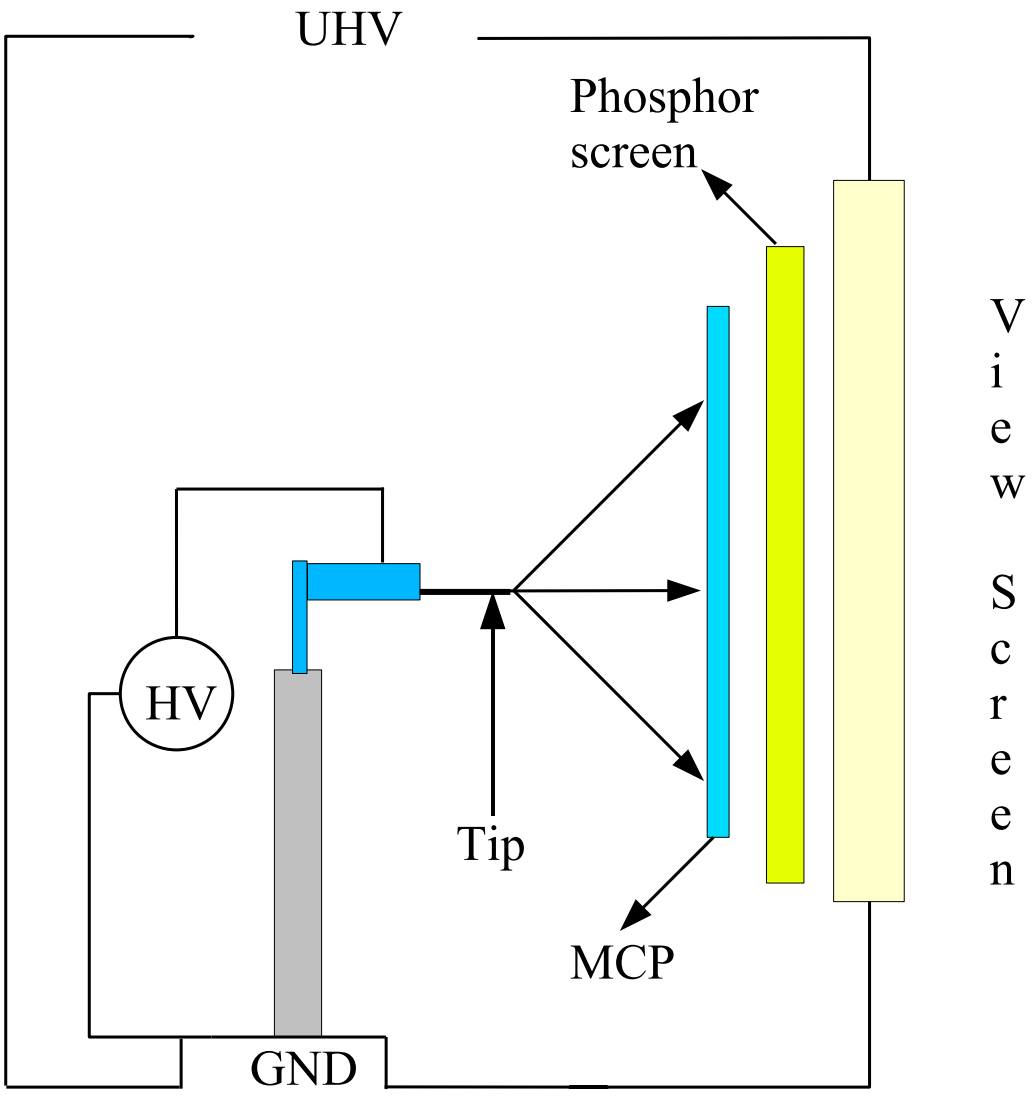

Figure 13: Schematic diagram of the field emission microscope (FEM) and field ion microscope (FIM) arrangement used to measure the radius of curvature of a solid metallic tip.

The electric field for a normal emitter is given by [105]:

$$F = \frac{V}{\kappa R}, \tag{35}$$

where V is applied voltage, R is the emitter radius (for our case the tip radius of curvature) and κ is a geometric factor. For the typical hyperboloidal shape of our tips κ is approximately 5 [105], and for most emitters κ is between 4 and 8. The parameter κ increases with the angle of the tip apex.

From the Fowler-Nordheim theory [103], the emission current is related to emitter radius by:

$$\ln\left(\frac{I}{V^2}\right) = \frac{-bR}{V}\upsilon\left(c\frac{V^{1/2}}{R^{1/2}}\right) + \ln\left(\frac{a}{R^2}\right), \tag{36}$$

where υ is a tabulated function, ϕ is the work function in eV, and the constants are defined by:

$$a = 6.16 \times 10^{-8} A/\phi$$
$$b = 3.415 \times 10^{8}\phi^{3/2}$$
$$c = 1.7 \times 10^{-4}\phi,$$

where A is the emitter area. The value of the constants for Al ($\phi^{Al} = 4.28\ eV$) and Cu ($\phi^{Cu} = 4.65\ eV$) tips are:

$$b^{Al} = 3.02 \times 10^{9}(eV)^{3/2}$$
$$c^{Al} = 3.97 \times 10^{-5}(eV)$$
$$b^{Cu} = 3.43 \times 10^{9}(eV)^{3/2}$$
$$c^{Cu} = 3.66 \times 10^{-5}(eV)$$

The graph of $\ln(I/V^2)$ versus $1/V$ is a straight line with a slope $bR\upsilon$ and intercept $\ln(a/R^2)$. By First assuming $\upsilon = 1$, we estimated the value of R from the slope of the line and the work function. By using this value of R to calculate the argument of υ, from the table the value of υ [106] can be found. By repeating the procedure the radius of the curvature will converge to a single value. The problem with this technique is the current density is sensitive to the work function and the work function varies with crystal

Table 3: Emission current as function of applied voltage

Voltage (in Volts)	*Current (in Amperes)*
300	8×10^{-11}
350	1.8×10^{-9}
400	1.22×10^{-8}
450	5×10^{-8}
500	1.88×10^{-7}
550	4.1×10^{-7}
600	1.15×10^{-6}
650	2.063×10^{-6}

Table 4: Sample of calculating the radius of the tip

Tabulate function	*Radius (in cm)*
$\upsilon(0)$	1.377×10^{-6}
$\upsilon(.62)$	2.5×10^{-6}
$\upsilon(.46)$	1.89×10^{-6}
$\upsilon(.53)$	2.12×10^{-6}
$\upsilon(.5)$	1.99×10^{-6}
$\upsilon(.52)$	2.09×10^{-6}
$\upsilon(.51)$	2.02×10^{-6}

orientation. By using the average value for the work function of the tip, the radius will be estimated to an accuracy of better than ±15% [103].

As an example sample we present the FEM data for one Cu tip. The measured emission current as a function of applied voltage by FEM is shown in Table 3. The current was measured from a potential drop across the 10 MΩ resistance connected in a series to the FEM.

A plot of $\ln(I/V^2)$ versus $1/V$ is shown in Fig. 14 and the graph is a straight line as expected from Fowler-Nordheim theory. The slope for this particular graph is -4718.8 ($=-bR\upsilon$) and the y-intercept is -18.62 ($=\ln(a/R^2)$).

A sample calculation of the radius of curvature for a Cu tip is shown in Table 4. We used κ=5 for this typical calculation and it is clear that the radius of the tip converges.

The radius of curvature R of the tip can be calculated from this slope using Fowler-Nordheim theory [105] and we obtained the radius of curvature R of this particular Cu tip

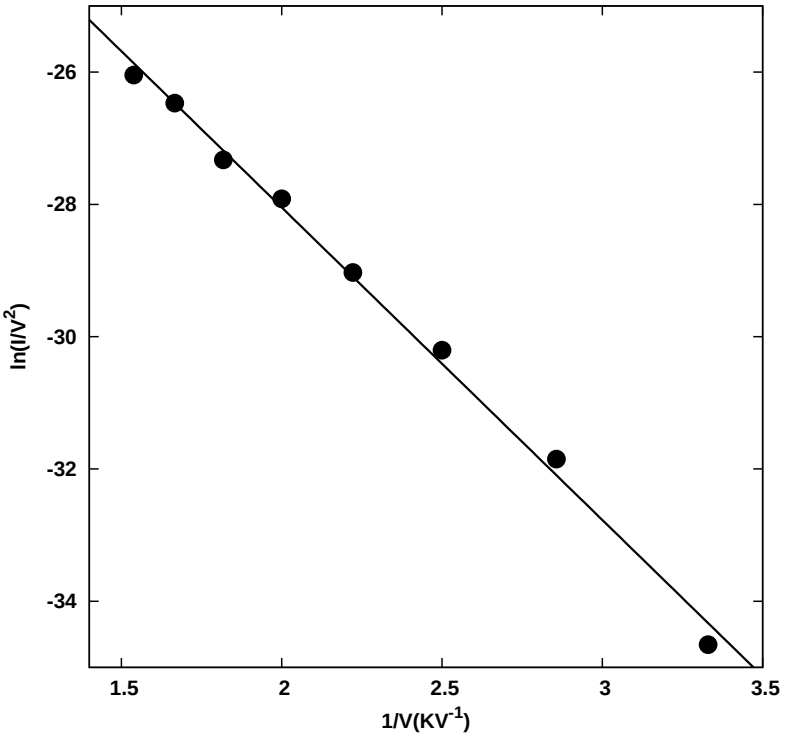

Figure 14: $\ln(I/V^2)$ versus $1/V$, with a slope of -4718.8 and y intercept -18.608. The points are the experimental data and the solid line is the linear fit to the data.

is about 20 nm and 12.5 nm for $\kappa = 5$ and 8 respectively.

2.4 Experimental setup

The schematic diagram of the Ga-HOPG contact conductance experiment is shown in Fig. 15(a). The image of the Ga-tip is shown in Fig. 15(b), magnified 12X from actual tip size. The dark spot at the end of the tip is due to the highly reflective surface of the liquid tip. No light is scattered in this region. This high reflectance is another confirmation that the Ga drop was not covered by any oxide skin.

The STM piezo controls the motion of the tip and the initial conductance is controlled by the STM servo. After achieving initial conductance, we retracted the tip a few nm to break the initial contact, and then pushed toward the HOPG surface by steps of 0.01 nm or larger while recording the current as a function of displacement at a fixed tip voltage (the HOPG sample was maintained at virtual ground by the current amplifier).

Figure 16(a) shows the image of the tip before the contact. The radius of curvature of

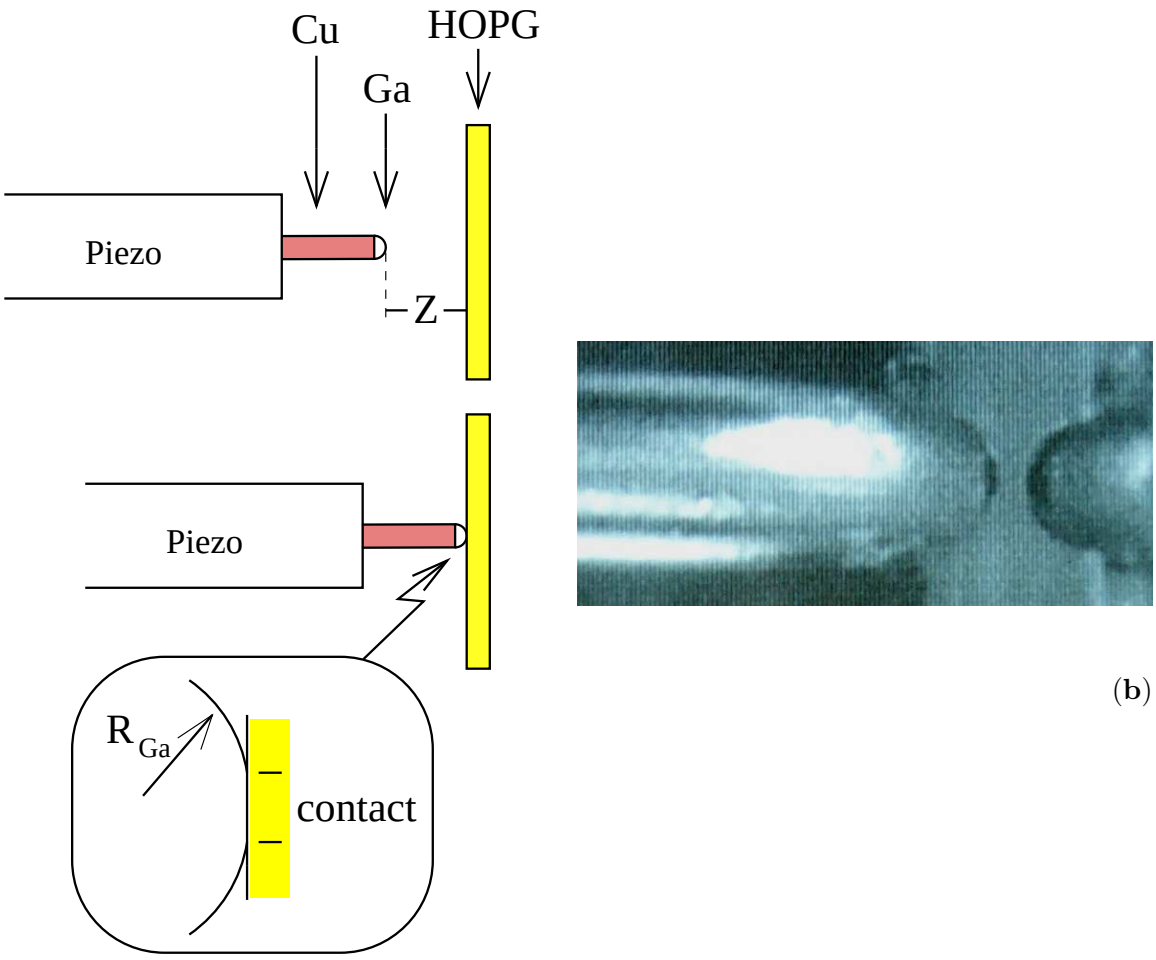

(a)

(**b**)

Figure 15: (a) Schematic diagram of the Ga-HOPG experiment. The top diagram when the drop and the surface are out of contact, the middle diagram when the drop and the surface are in contact and the bottom diagram is the detail between the drop and graphite during contact. (b) An image of Cu rod with Ga liquid at the end of the rod. This is an image of the video screen taken by a digital camera.

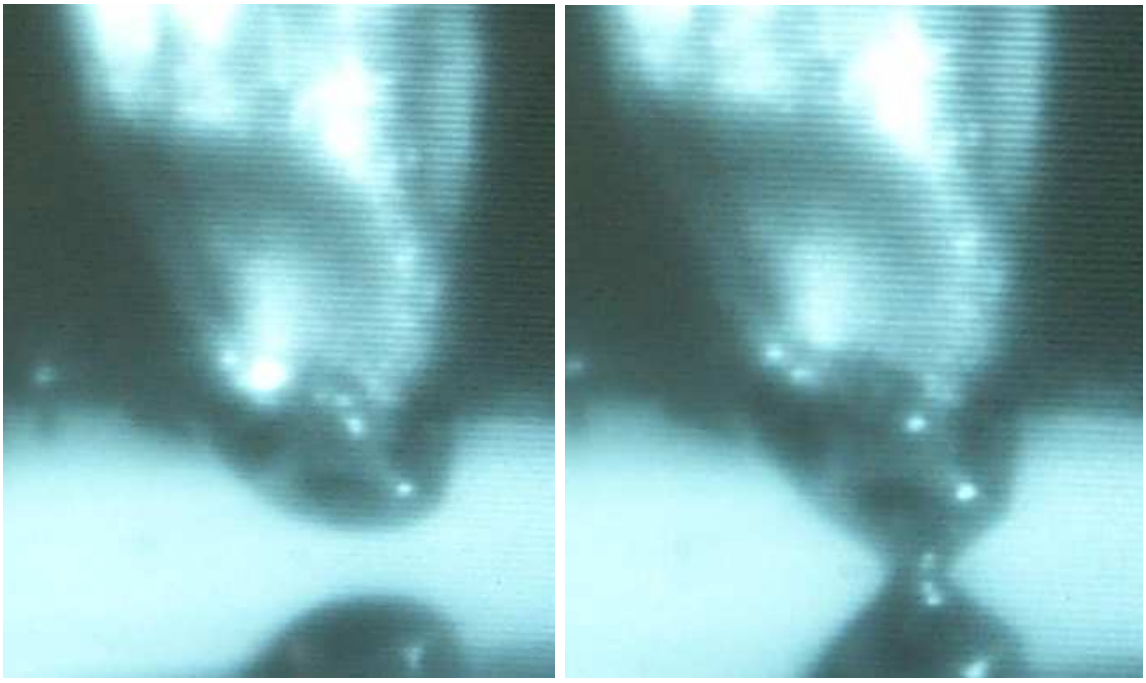

(a) (b)

Figure 16: Image of a Ga liquid tip. (a) Image of the Ga drop before contact. The radius of drop is 235 μm. (b) The image of Ga drop in contact with HOPG. The radius of the neck is 85 μm. Formation of the "neck" as in (b) indicated substantial wetting of the HOPG surface, which was unacceptable for these experiments. After an observation such as this, the HOPG was typically cleaved again, the Ga source was reheated and scraped, and the Ga drop was re-formed.

the tip before contact is around 235 μm, as measured by fitting a circle to the end of the drop. The radius of the neck is 85 μm and measured from contact neck in Fig. 16(b). The formation of such a neck indicated wetting of the HOPG surface. Date from these cases was not considered reliable

The schematic drawing of a solid tip is shown in Fig. 17 and the shape of the tip is hyperboloid. The radius of curvature for the tip is indicated by R and the detailed measurement of the radius of curvature was discussed in the previous section. The sample initially approached toward the tip by the manual control of the inch-worm motor, after which the tip was brought into tunneling range by the STM servo controlled by a computer. The initial displacement (tunneling distance) between the tip and HOPG is indicated by Z in the diagram. Current versus displacement $[I(Z)]$ measurements were done in the same manner as

described for liquid tips, with the increment of tip displacement typically $0.1-1$ $\mathring{A}$. At each displacement increment the current was measured for a fixed tip voltage in both forward and reverse displacement directions. In some of the experiment we measured the current as function of displacement and tip voltage. For most of the experiments imaging and $I(Z)$ measurements were done simultaneously. Thus, we were able to observe the effect of atomic steps on the conductance spectra.

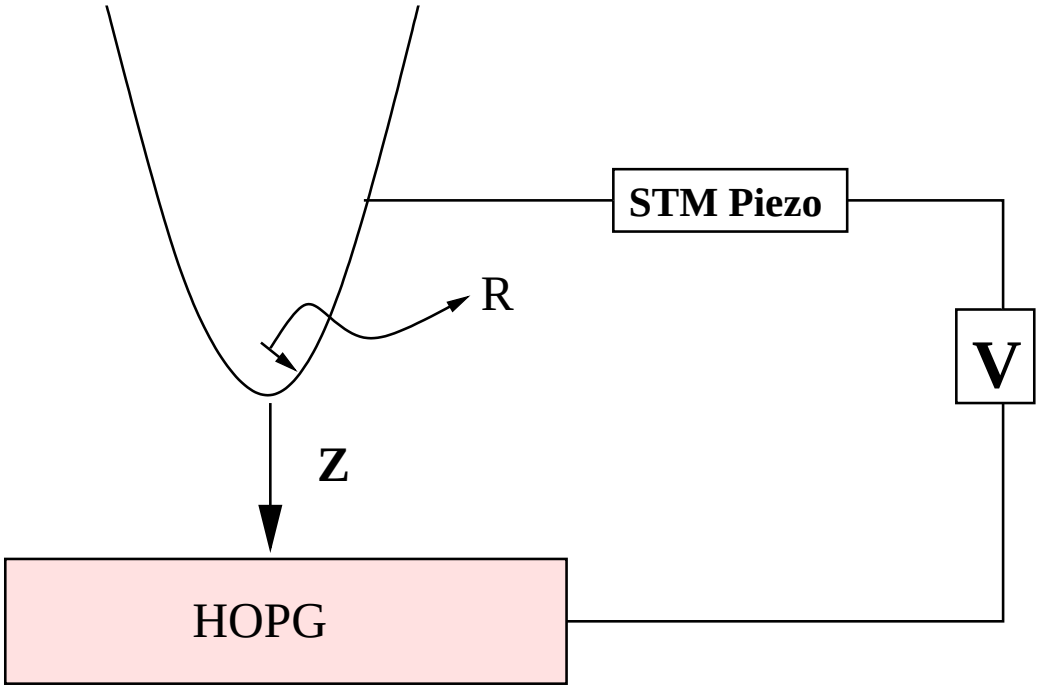

Figure 17: A simple schematic diagram between a solid tip and HOPG. The Z motion of the tip was controlled by the STM piezo. The initial position of the tip was determined by the current setpoint. V is the applied bias to the tip.

CHAPTER III

CONTACT CONDUCTANCE OF LIQUID METAL TIPS

Gallium metal was used in its liquid state to create nearly zero-load contacts to graphite with easily adjustable contact area. The detailed preparation and characterization of the Ga tips and graphite substrate were stated in Chapter II. Liquid Ga does not deform the surface of graphite during contact. Consequently we were able to use large tip displacements without changing the structure of the sample. The contact pressure P can be estimated from the Young-Laplace equation [107] $P = \frac{2\gamma}{R}$, where γ is the surface free energy (0.72 N/m for Ga liquid [77]) and R is the radius of curvature of the spherical liquid surface. The contact force F at the Ga-HOPG interface is estimated as $F = PA = \frac{2\gamma}{R}\pi a^2$, where a is the contact radius. The pressure for radius of curvature 215 μm is 6.68 kPa and the contact force for contact radius a= 2.5 nm (estimated later in this Chapter from the image width of a graphite step-edge) is around 130 fN. This is 10 - 10^2 times less than the smallest forces achievable in commercial scanning force microscopes.

The initial contact of the liquid-drop tip to the graphite surface was controlled by the STM servo. This allowed us to achieve gentle contact to the surface in most cases (resistance$\geq$200 $M\Omega$). Our initial experiments utilized Ga drops with $R_{Ga} \geq 200$ μm. In many such cases it proved difficult to achieve stable contact conductance for STM servo setpoint current >100 nA, corresponding to a resistance of 200 kΩ at the typically tip bias voltage of 20 mV. During subsequent experiments with smaller Ga drops, it was possible to achieve stable contact conductance for servo setpoints as low as 0.1 nA (200 MΩ). It should be understood that in either case, the contact conductance was measured over a range of tip displacement, beginning with a retraction from the surface to beyond the point at which the conductance vanished (broken contact). Current versus Z displacement was then recorded while pushing the tip towards the HOPG surface and subsequently retracting to beyond the broken-contact point.

A 94.74 Ω internal series resistance of the digital to analog converter (DAC) was subtracted from measured resistance values to obtain the contact resistance at the interface of Ga-HOPG. With the ability to use the STM servo to maintain high resistance contacts (i.e. small area), we found, remarkably, that it was possible to image the HOPG surface with the liquid tip in contact with the graphite surface. The image acquisition was done in the same way as normal STM, but there is no vacuum tunnel barrier. To our knowledge, this is the first time that atomic-scale structure has been imaged with a liquid scanning probe tip. As will be seen, the simultaneous acquisition of image and $I(Z)$ spectra provides new insights into the liquid/solid interaction for Ga/HOPG. In next section, we will present experimental $G(Z) = I(Z)/V$ measurements for large tip displacements. The second following section presents $G(Z)$ measurements at small displacements which were acquired simultaneously with an image of surface of the sample. In Sec. 3.3 we discuss the imaging in more detail, and then conclude with a discussion of salient points in Sec. 3.4.

3.1 Current versus Distance: Large Displacements

HOPG substrates were annealed at 1100 ^oC for 30 min. before contact experiments in order to clean the surface from contamination. In this experiment we didn't have information on the topography of the graphite sample at the contact region. However, separate images with a tungsten tip showed flat terraces, typically 400 nm in size as shown in Fig. 18. The images were taken at 100 pA tunneling current and tip bias of 2 V.

Figure 19 shows the variation of contact conductance as a function of tip displacement for a Ga tip with radius of curvature 215 μm. The radius of the tip was measured from the magnified image of the tip as described in Chapter II. The data were acquired for a tip voltage of 20 mV after stabilizing the Ga-HOPG contact at a servo setpoint current of 100 μA. After achieving initial contact, we retracted the tip to beyond -280 nm to break the initial contact and we pushed the Ga drop-tip toward the graphite in increments of $\sim$1.5 nm, measuring the current at each Z position. The Ga tip was pushed up to +170 nm past the initial position of the tip. The red line in the Fig. 19 was taken during forward displacement (pushing toward the graphite surface) and the black line was taken during the

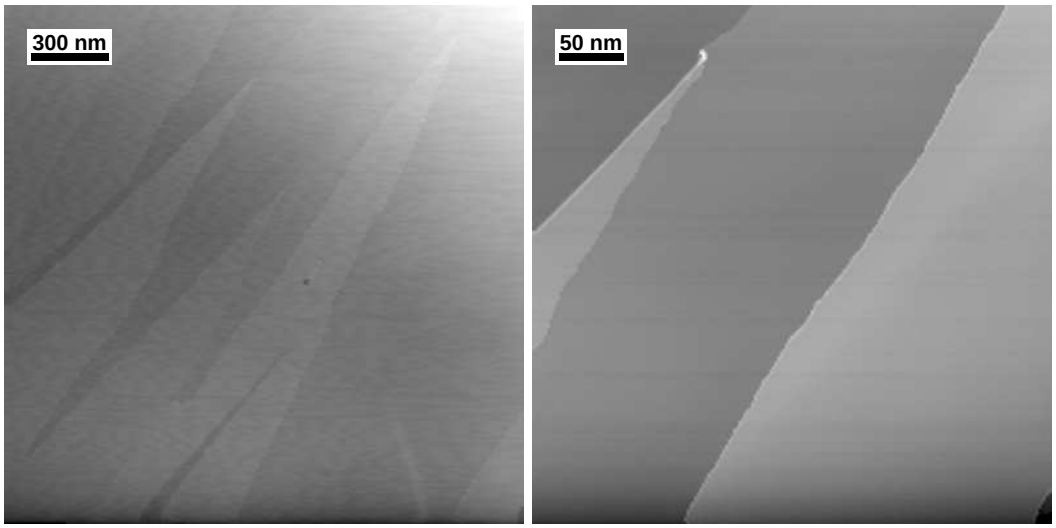

(a) (b)

Figure 18: STM images of graphite surface by a tungsten tip [(a) 2 $\mu m \times 2$ μm, (b) 400 $nm \times$ 400 nm]. The images were taken with tip bias voltage 2 V and a tunnel current of 100 pA. The graphite was annealed at 1125 ^oC for 20 min.

reverse displacement (pulling from the graphite surface). The inset in Fig. 19 shows the initial conductance step with higher resolution. The value of the initial conductance is about 0.06 Go (conductance quantum $Go = 2e^2/h = [12,960\ \Omega]^{-1}$) and the forward conductance occurs at displacement of -230 nm before the servo-determined initial position of the tip (Z=0). This conductance is equivalent to about 216 kΩ contact resistance, and it remains nearly constant over a span of 270 nm. The second plateau occurs at a Z displacement of +40 nm with respect to the servo position of the tip, with a conductance of 0.5 Go (26 kΩ). The span of the plateau on the Z-axis is about 50 nm. The third conductance plateau is 1.2 Go (10.8 kΩ) and it spans about 70 nm. The value of the next conductance plateau is about 3.5 Go (3.7 kΩ).

As we observe from the conductance curves, hysteresis exists between the forward and reverse directions even though the conductance values and the span of the plateaus are similar in both directions. The average Z hysteresis between the forward and reverse $G(Z)$ spectra is about 90 nm except in the region of the initial contact, where the hysteresis is only $\sim$ 30 nm.

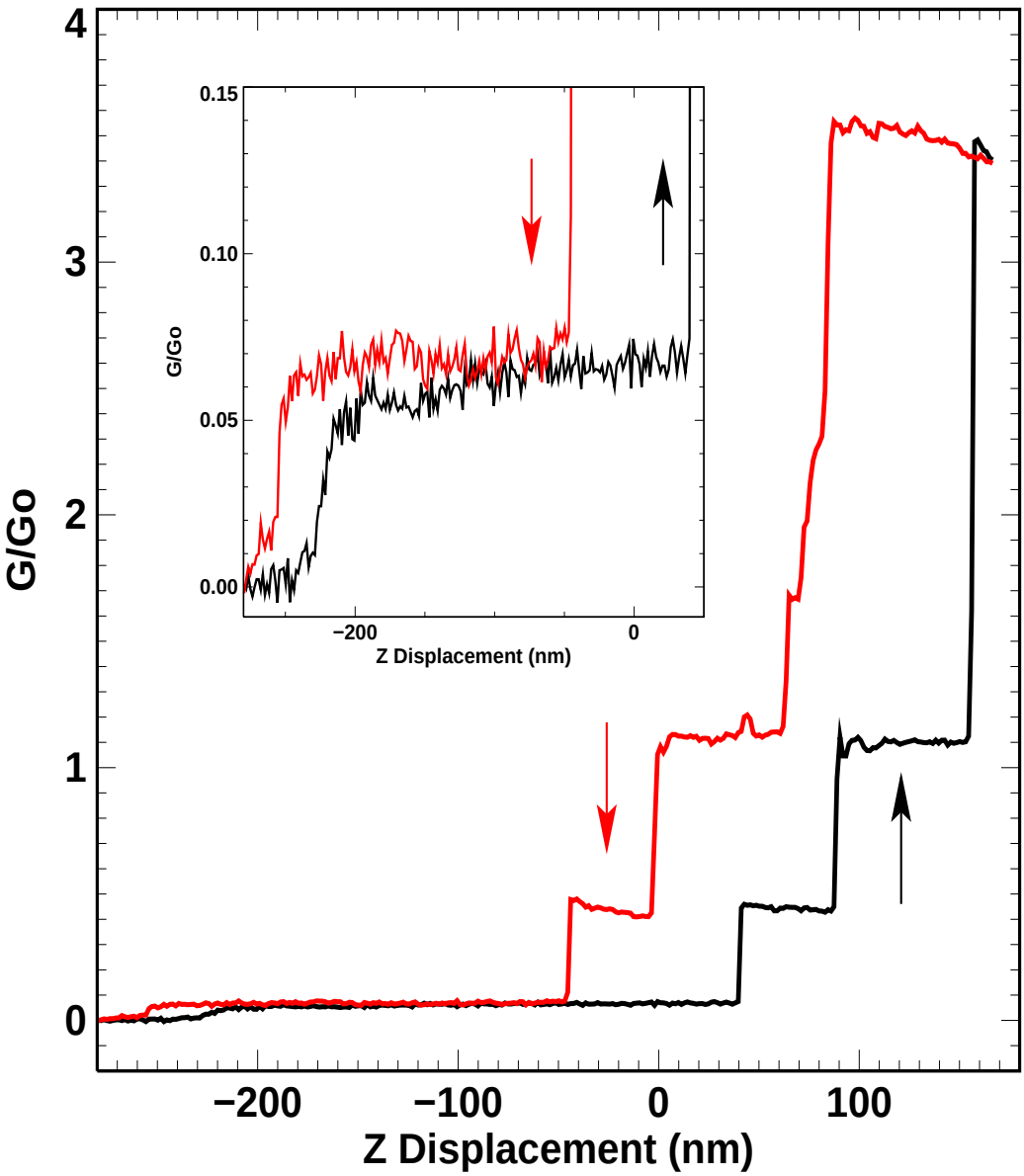

Figure 19: Variation of the conductance G as a function of the tip displacement Z at a temperature of 311 K. The radius of curvature for the Ga tip is 215 μm. The applied bias voltage between the Ga tip and HOPG is 20 mV and the set current is 100 μA. Red line is the forward conductance and black line is the reverse conductance.

In Fig. 20 are shown conductance histograms of many conductance curves to demonstrate the consistency of the conductance measurements. The largest counts occur for the initial contact (0.06 Go) and the next two conductance plateaus near 0.5 Go and 1 Go. The peaks of the last two plateaus are much broader and smaller in comparison with the first three peaks.

The same Ga drop (R_{Ga} = 215 μm) was used as in the previous experiment but the tip was moved laterally to a different spot on the graphite surface, 1.5 μm from the initial location. $I(Z)$ data was acquired at the same set current and bias voltage, but the tip displacement was much larger than the previous experiment as shown in Fig. 21(a). For tip displacement from -200 nm to 600 nm, the conductance increases from 0 to about 250 Go (52 Ω), typically in discrete steps. Figure 21(a) shows five different conductance spectra acquired sequentially in this figure. More than 30 similar spectra display the same behavior demonstrating the reproducibility of these spectra. The next step is to compare these conductance spectra with those in Fig. 19, which were taken at a different position on the graphite. Figure 21(b) shows a magnified view of one of the spectra from Fig. 21(a). We observe that the conductance in forward direction (solid line) is similar in behavior to those with smaller displacements, but in the reverse direction, the conductance curves don't show the smaller plateaus and the hysteresis is much larger. In fact, for these spectra the Ga-HOPG contact didn't break in the reverse direction. The reason for the hysteresis between the forward and reverse direction is undoubtedly due to the nature of the liquid tip. As presented in Chapter II [see Fig. 16(b)] the Ga drop began to wet the HOPG surface in some cases. As discussed in subsequent sections, we believe that wetting occurs exclusively at defects on the graphite surface.

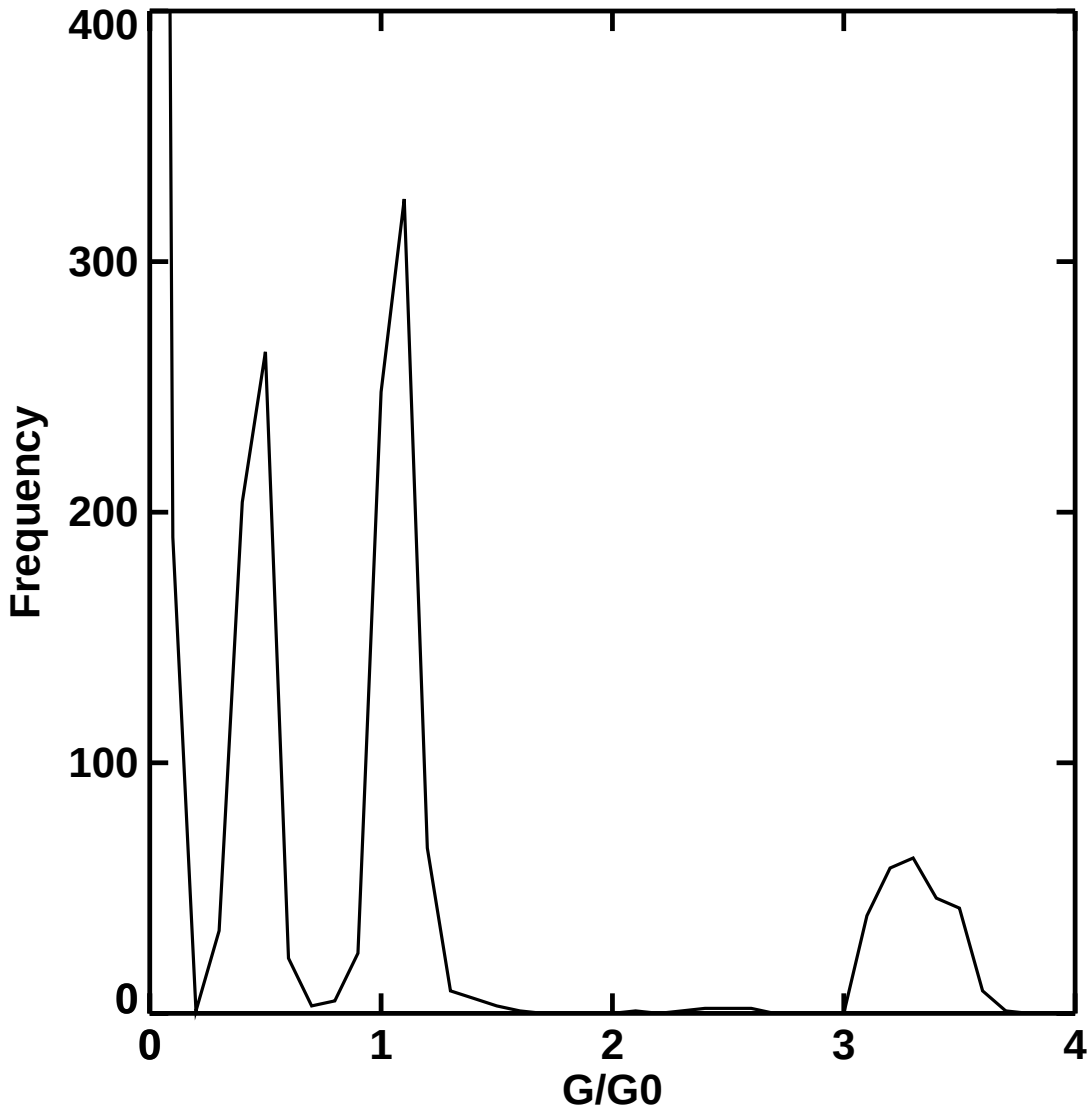

Figure 20: Conductance histogram for the Ga tip ($R_{Ga} = 215\ \mu m$) at a temperature of 311 K. The histogram is calculated for the forward spectra only. The applied bias voltage between the tip and HOPG is 20 mV and the set current is 100 μA. Note that the width of the conductance plateaus in the $G(Z)$ spectra determine peak heights, while the reproducibility of the spectra and flatness of the plateaus is reflected in the peak widths.

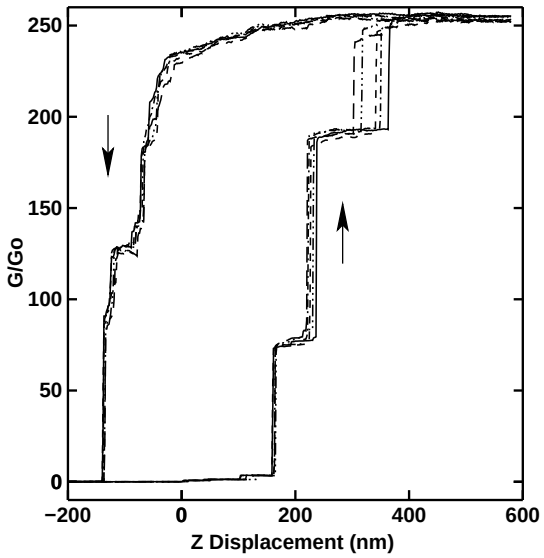

(a)

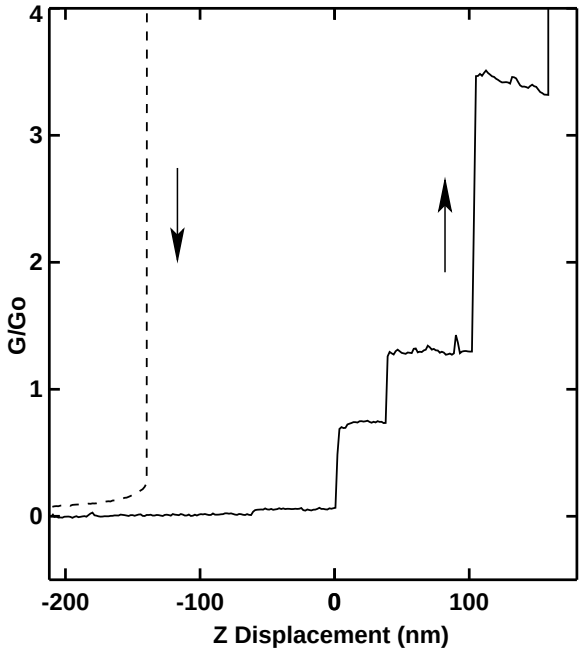

(b)

Figure 21: Conductance versus Z Displacement between Ga and HOPG at a temperature of 311 K ($R_{Ga} = 215\ \mu m$, $I_T = 100\ \mu A$, $V_T = 20\ mV$). (a) Five spectra with a large displacement. The order of acquisition was solid, dashed, dash-dot, dash-dot-dot-dot, and long dashes lines. (b) The magnified view for the sold line of the spectra from Fig. 21(a).

We used a different Ga tip with smaller Ga drop (R= 50 μm). The detail method of dipping of the Cu rod to the liquid Ga was presented in Chapter II. For most of the tips, we let the Cu rod stay inside the Ga liquid for a few min. but for this particular tip we left the tip inside the Ga for about 10 min. This 1 mm Cu rod at the end that dipped into the Ga liquid was etched with nitric acid in order to have a small Ga drop. The diameter of the Cu rod at the etched end was around 128 μm.

Figure 22 shows conductance versus Z displacement for the 50 μm Ga drop measured with V_T=20 mV. The STM servo current was 1 μA. The current was acquired every 1.5 nm increment of Z displacement from -425 nm to 250 nm. Two distinct plateaus occur at 0.02 Go and 0.04 Go in both forward and reverse directions. The next two plateaus show more variation, but are observed in both acquisition directions at $\sim$0.13 Go and 0.33 Go. As for the 215 μm Ga drop, there is hysteresis between the forward and reverse data, even though the overall behavior in both directions is similar.

The conductance spectra shown in the inset of Fig. 22 are 10 of more than 60 similar $G(Z)$ spectra which demonstrate the reproducibility of the data in both directions. The only notable time-dependent feature was a slight shift of the initial contact displacement toward positive Z from one spectrum to the next. We observed a temperature difference $\Delta T \leq +3\,^{o}C$ in the chamber from the start and the end of the experiment. This temperature variation might have caused the tip to drift away from the graphite surface and thus cause the initial contact displacement to shift to larger displacement by a few angstroms (note that the drift would be manifest only in a slight variation of the servo setpoint current and position due to proportional feedback on the Z error signal).

The radius of curvature of the liquid was determined from the microscopic image of the tip. This radius most likely is not the actual radius, because the shape of the drop might change during the contact especially when the tip is under applied field. We can't make analysis like contact radius based on the radius measured from microscopic image of the drop. We will address in the next section a method for estimating the contact radius from the image of the graphite surface taken by a liquid drop.

Figure 24 shows the conductance curve as a function of tip displacement for a Ga drop

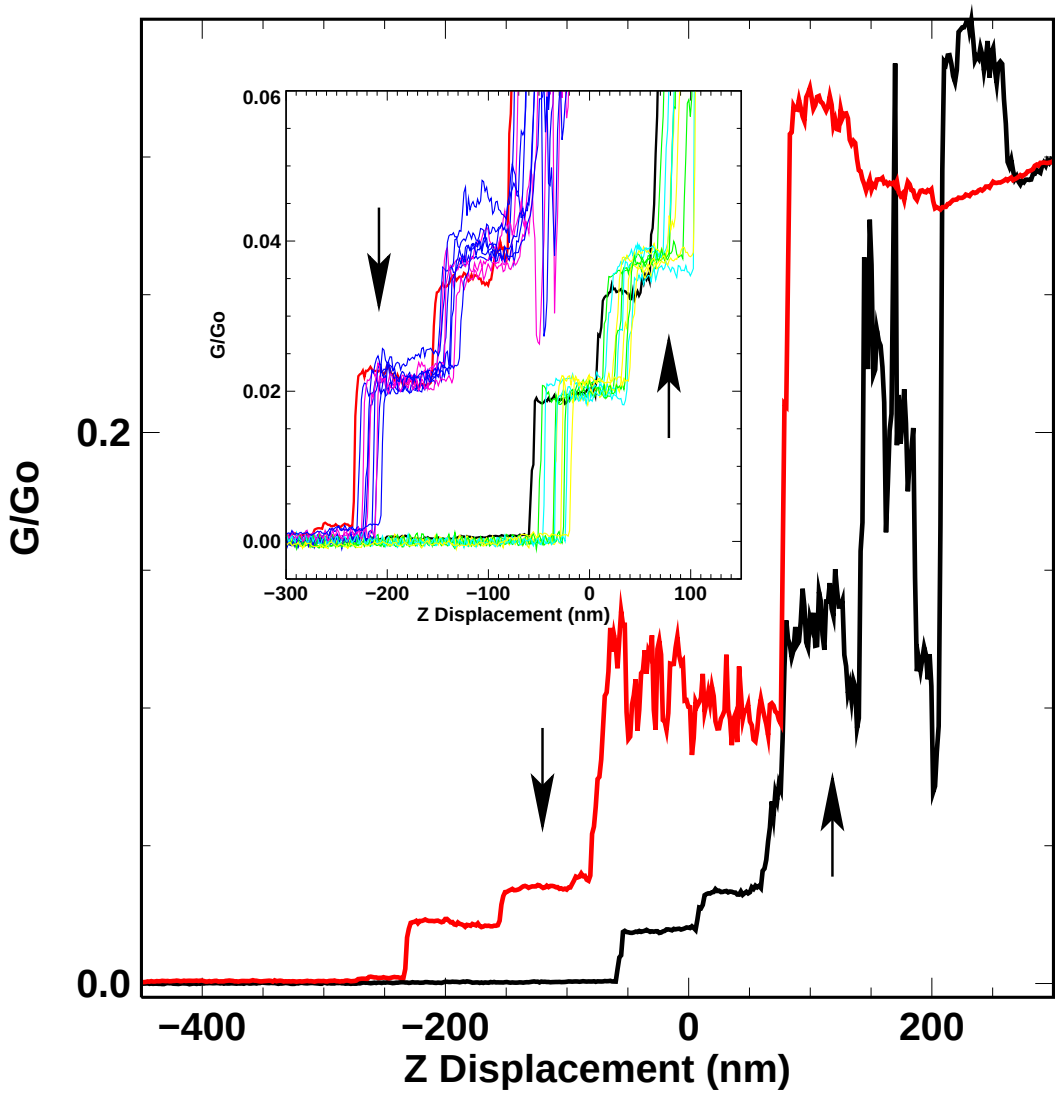

Figure 22: Contact conductance versus Z Displacement of Ga drop and HOPG ($R_{Ga} = 50\ \mu m$) at T = 311 K. The applied bias voltage between the tip and sample is 20 mV and the set current is 1 μA. Black line is forward conductance and red line reverse conductance for the main figure.

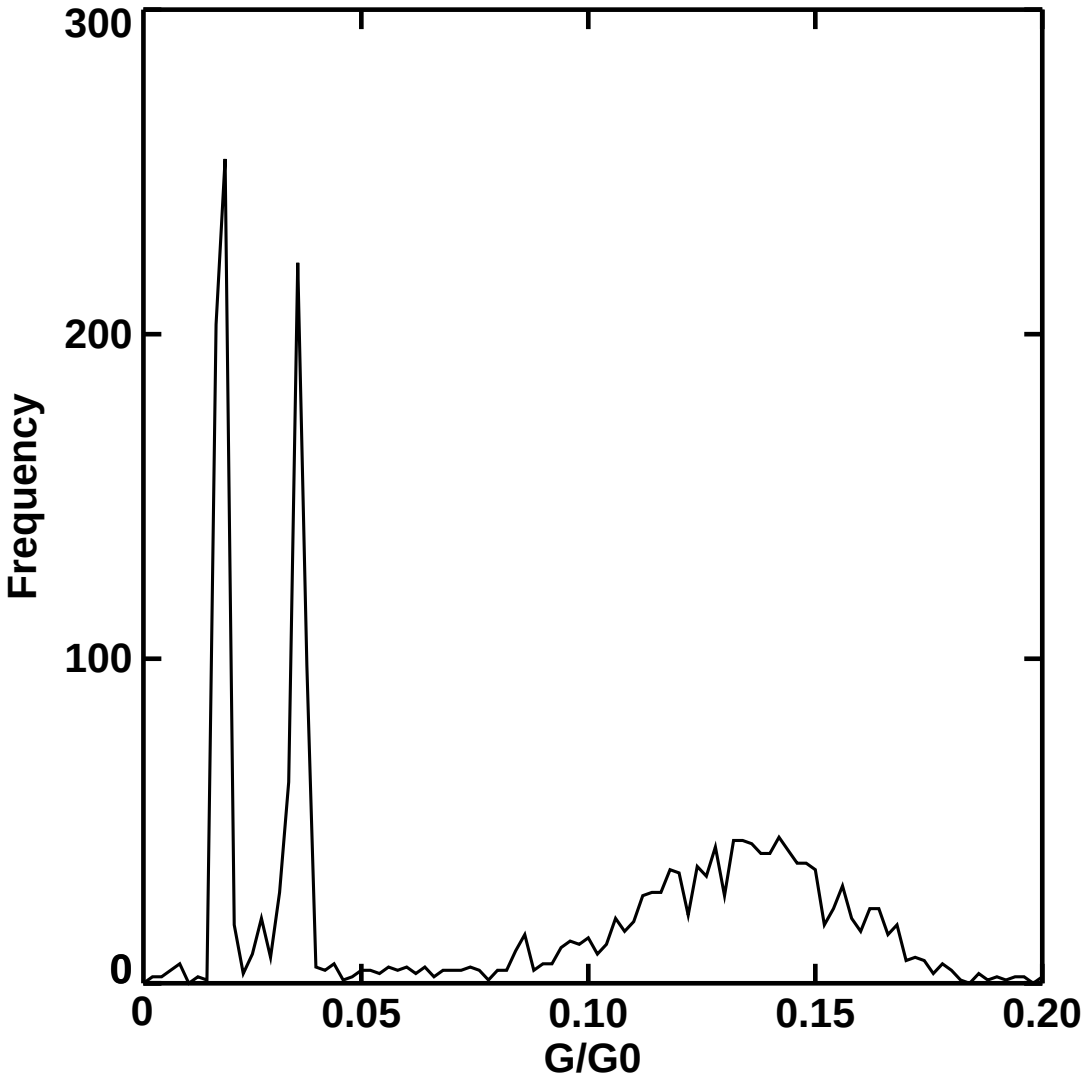

Figure 23: Conductance Histogram for the Ga tip ($R_{Ga} = 50\ \mu m$) at T = 311 K. The bias voltage between the sample and drop is 20 mV and the set current is 1 μA. The histogram is only for the forward conductance measurements.

of 36.5 μm radius. The Z=0 position was determined by the STM servo setpoint of 10 μA, at a bias voltage 15 mV (slightly different from the bias voltage of the previous conductance measurements). The solid line in the graph is the forward displacement conductance and the dashed line is for reverse displacements. We acquired a set of reproducible $G(Z)$ spectra, with a single representative shown in the figure and magnified inset. The value of the initial conductance contact is about 0.14 Go (92.6 kΩ) and it occurs at a displacement of -100 nm from the initial position of the tip. The second conductance plateau is about 0.26 Go (50 kΩ) followed by a sudden jump to a large conductance about 7 Go (1.85 kΩ). The Z displacement difference between the forward and reverse are 83 nm, 89 nm and 61 nm for the first, second and third plateaus respectively.

Figure 25 shows the conductance histogram of the 36.5 μm Ga drop. The first two plateaus contribute sharp peaks with 2000 to 3000 counts, demonstrating clearly the consistency of the data. The conductance histogram for larger G values is shown in the smaller box in the figure. In this case, many small plateaus occur (tens of histogram counts versus 1000-3000 in the first peaks), as indicated by the sharp peaks in the histogram.

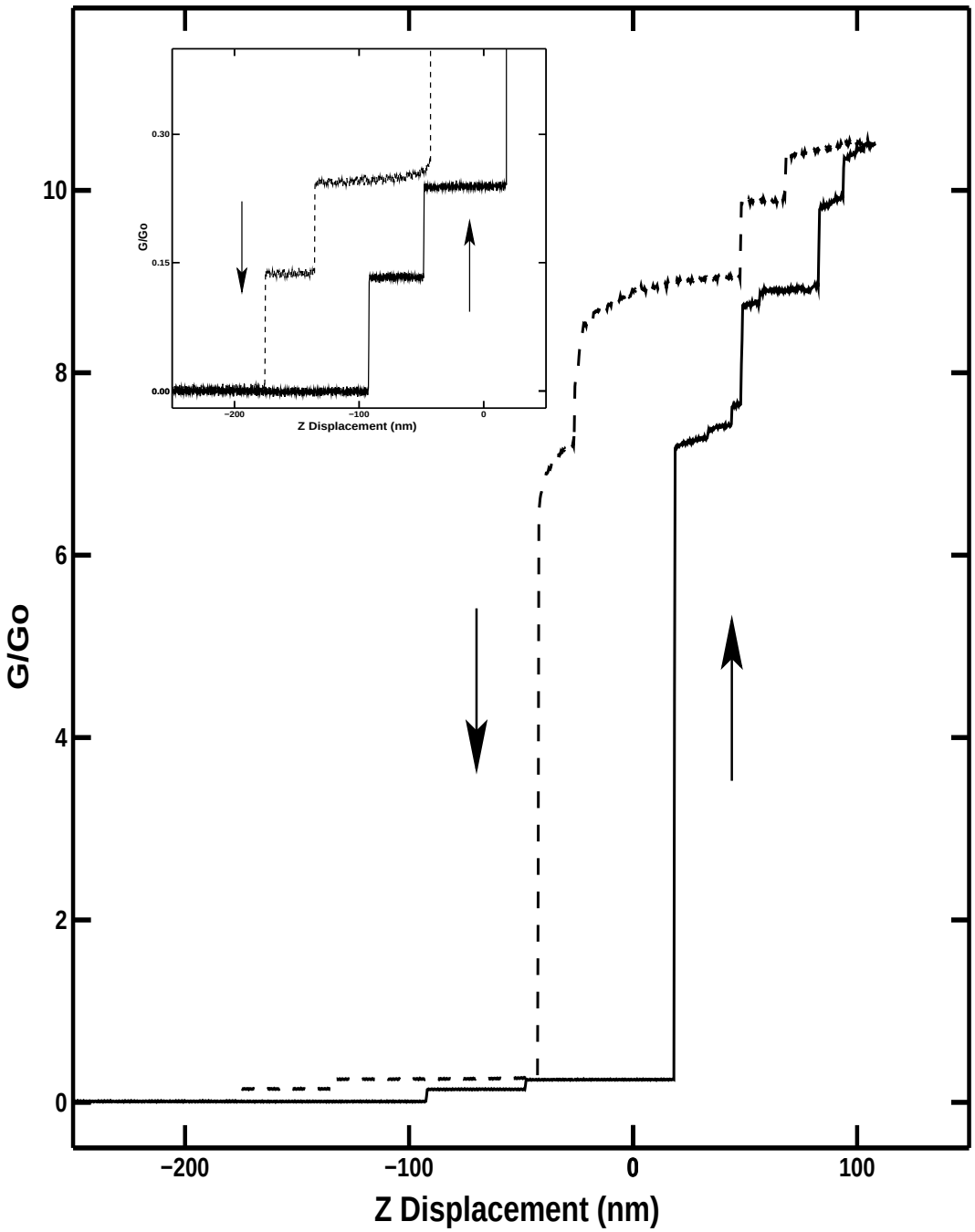

Figure 24: Contact conductance versus Z Displacement of Ga drop and HOPG ($R_{Ga} = 36.5\ \mu m$) at temperature of 311 K. The applied bias voltage between the tip and sample is 15 mV and the set current is 10 μA. The solid line is the forward conductance and dash line the reverse conductance.

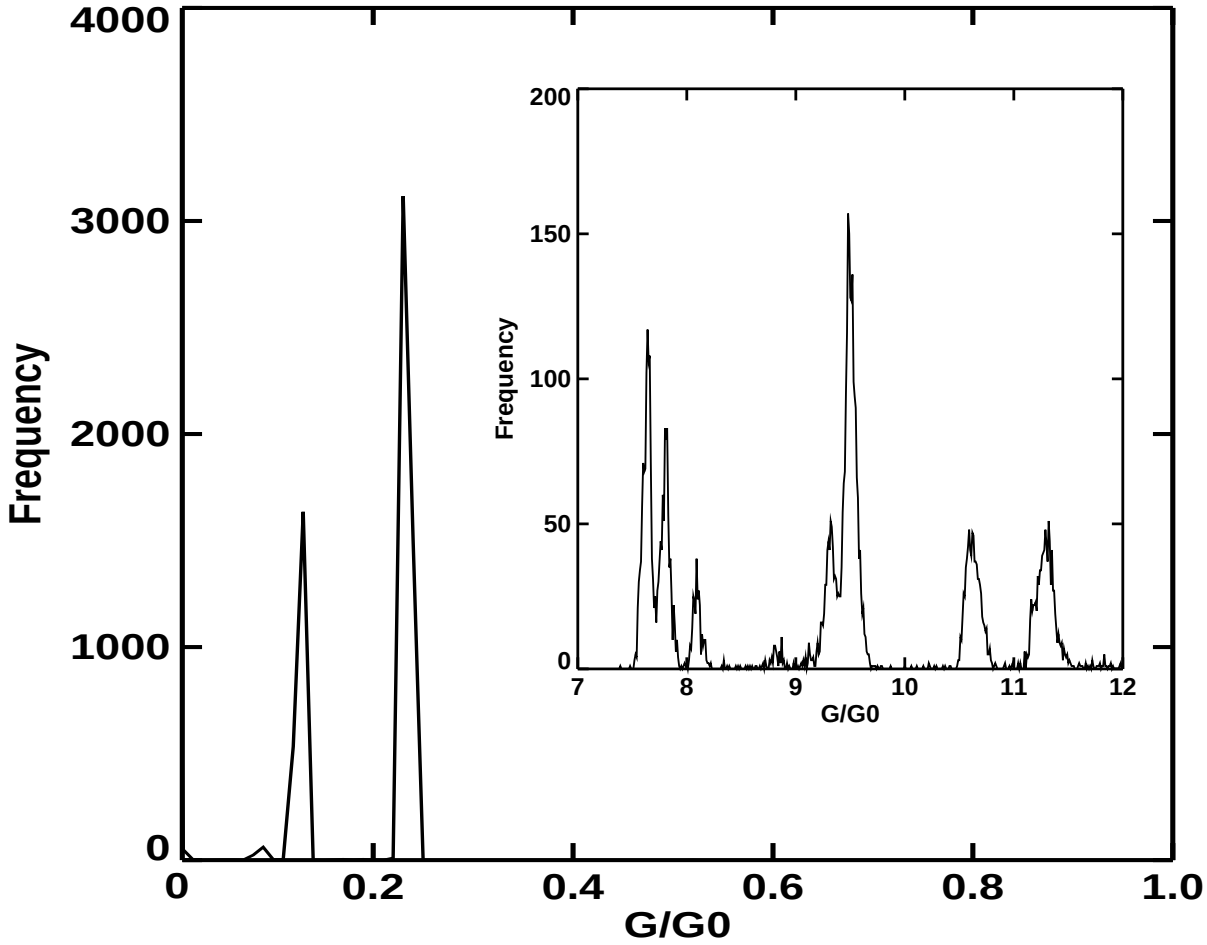

Figure 25: Conductance Histogram for the Ga tip ($R_{Ga} = 36.5\ \mu m$) at T = 311 K. 60 spectra were used to obtain the histogram. The histogram is only for the forward conductance measurements.

3.2 Simultaneous Imaging and $I(Z)$: Small Displacements

In the previous section we were not able to estimate the radius of contact at the Ga-HOPG interface. Also, we didn't know the topography of the sample at the region of contact. In this section we will try to address these two issues by imaging the graphite sample with the liquid tip itself. It is, to our knowledge, the first such imaging of a surface. The imaging was done in the normal STM mode, with 100 pA setpoint current at a tip bias of 20 mV. The small contact conductance resulted in a contact area small enough to resolve atomic-scale vertical features on the surface of the sample. In order to confine the contact area to lie within the imaged region, we didn't use large Z displacement in these experiments. All the $G(Z)$ in this section were acquired simultaneously with the image, via the method of current imaging tunneling spectroscopy (CITS) [108]. In the normal CITS technique, scanning is stopped at chosen positions during STM image acquisition, and a current versus voltage spectrum is acquired at fixed tip-sample separation. For our measurements, the tip-sample separation was varied at fixed voltage to obtain $I(Z)$.

An image of graphite taken by a liquid Ga tip is shown in Fig. 26. The liquid tip was in contact with the graphite surface during the imaging process. Atomic layer steps are apparent in the image. Imaging using a liquid tip gave us the topography where the contact conductance was acquired and we were able to observe the effect of the graphite surface features on the contact conductance measurements.

The contact diameter can be estimated from imaged width of atomic steps on the surface [14]. The initial contact radius was estimated to be 2.5 nm. The contact force for this 170 μm Ga drop is around 170 fN, as estimated from the Young-Laplace equation [107]. The profile of two steps is shown in Fig. 27. The imaged heights of these layers is about 6.6 $\AA$. This height is equivalent to the two layers of graphite.

Figure 28 shows conductance versus Z displacement at the four positions labeled in Fig. 26. The $G(Z)$ and image were taken at the same bias voltage of 20 mV, with the image set current 100 pA. We measured around 200 $I(Z)$ at different spots across the surface and they are relatively very reproducible. We present 4 $G(Z)$ as representative in this figure. The initial conductance is very small, of order 5 nS (6.5×10^{-5} Go). The

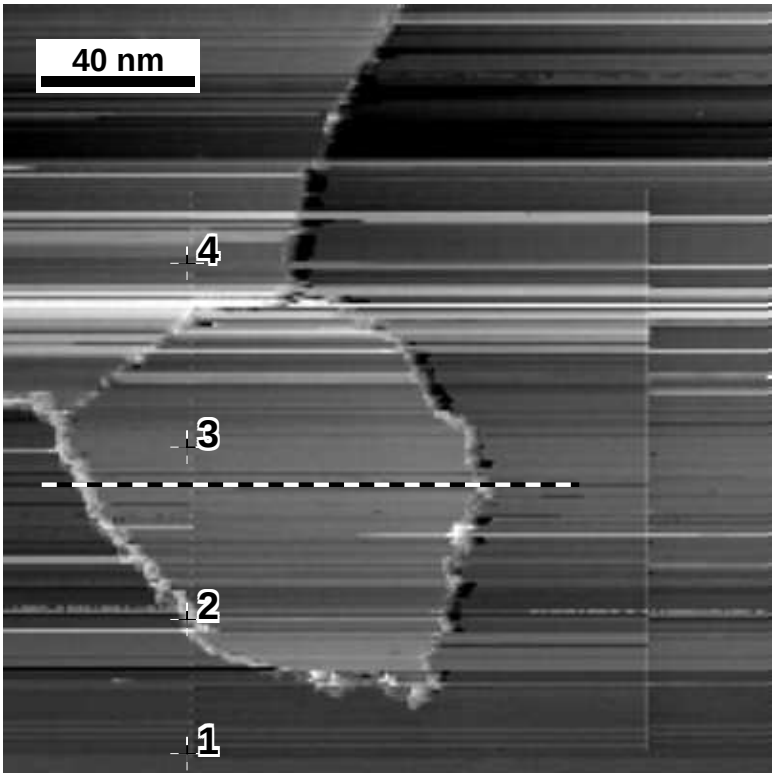

Figure 26: Imaging the graphite surface using a liquid tip ($R_{Ga} = 170\ \mu m$, $200\ nm \times 200\ nm$) at T = 311 K. The tunnel current is 100 pA and bias voltage is 20 mV.

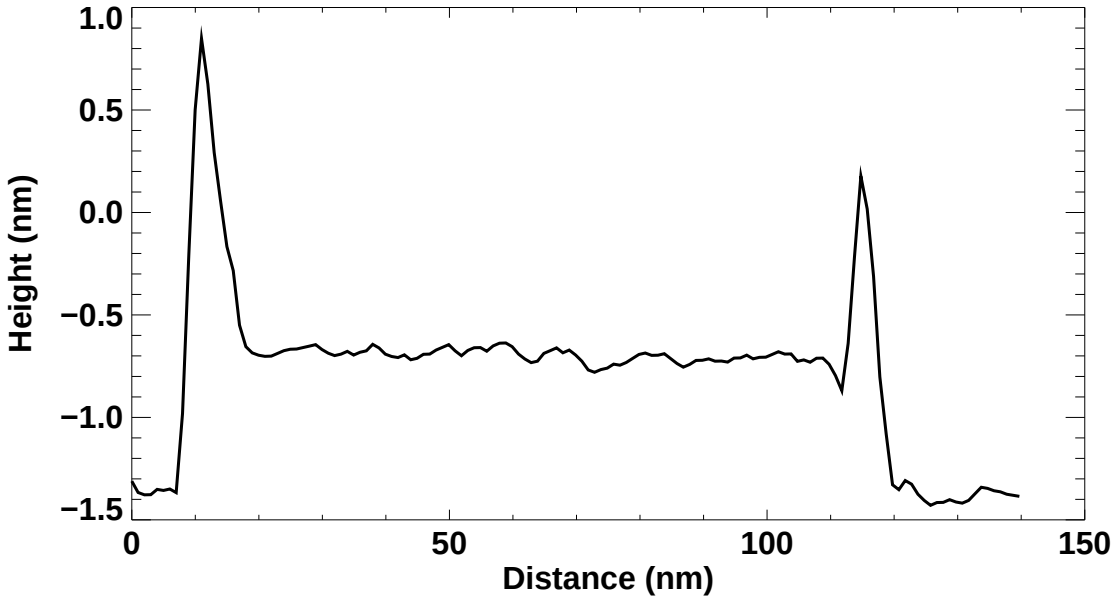

Figure 27: Profile of the surface height across the segment marked in Fig. 26.

spectra 1 and 3 were taken over flat regions of the surface as indicated in the image of Fig. 26. Their conductance spectra don't reveal any hysteresis between the forward and the reverse conductance. However, spectrum 2 which was taken over a graphite step shows hysteresis between the forward and the reverse conductance traces. We observe that the conductance in the forward direction is similar to those acquired over flat regions but in the reverse direction the conductance is not stable. This hysteresis between the forward and the reverse $G(Z)$ traces indicates an irreversible process, such as structural change at the step edge of the graphite during contact. Either the liquid Ga wets graphite at the step edge, or some carbon is removed from the step edge during contact. There is a good indication on the image of the graphite that Ga nano drops are deposited on the step edge, and for this reason we conclude Ga can wet graphite at step edges on the atomic scale. Note that spectrum 4, acquired near an atomic step, also shows a small amount of hysteresis. According to the literature [96], Ga doesn't wet graphite on the μ-scale, but from our observations it appears that gallium can wet graphite at atomic scale steps. We will discuss the wetting in more detail in the next section.

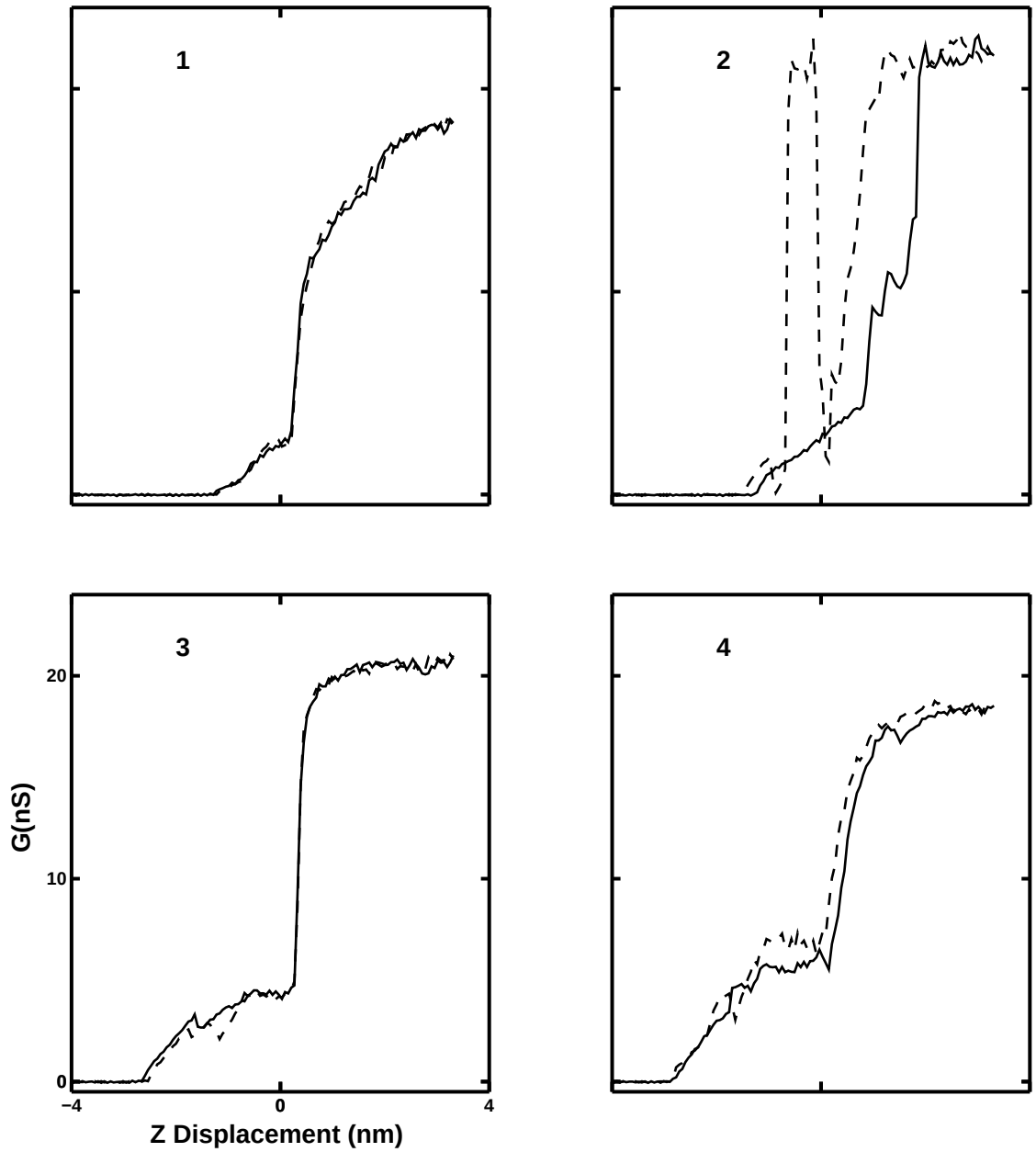

Figure 28: Contact conductance versus Z displacement, ($R_{Ga} = 170\ \mu m$) at temperature of 311 K ($I_T = 100\ pA$, $V_T = 20\ mV$). Solid line is forward and dashed line is reverse contact conductance.

Figures 29(a) and 29(b) show another image and $G(Z)$ spectra that were taken simultaneously. The Ga drop was the same as the previous experiment ($R_{Ga} = 170$ μm) but the $G(Z)$ were measured at a different location on the graphite, i.e. the tip was moved laterally X and Y by 130 nm and 40 nm from the initial spot. The image is a raw image which wasn't processed. The current was measured every 0.2 $\mathring{A}$ increment in Z displacement. The step height at the bottom right corner in image is 1 nm which is very close to 3 mono layers of graphite. The contact radius is around 2.5 nm estimated from the step width measurement (step width $\sim$ 5 nm). The source of the elevated region in the center of the image does not appear to be surface structure. Rather, the liquid may have flowed slightly. The $G(Z)$ spectra do not indicate any dramatic change in the electronic properties within this region.

In Fig. 29(b) we show four representative spectra from a total of 90. The conductance spectra were very reproducible and without significant hysteresis. Detailed views of the data between 6 - 10 nS showed behavior similar to the previous conductance spectra. That is, the conductance increases in almost a $\sqrt{Z}$ form to a short plateau at 5-6 nS, then rises to a second plateau near 20 nS. In this case, at $Z = 0.6$ nm the conductance reaches a maximum around 18 nS but the plateau has a negative slope. The conductance *decreases* with Z displacement for a while before it increases to higher conductance. Note that this behavior is reversible, i.e. it occurs identically on the forward and reverse $G(Z)$ spectra.

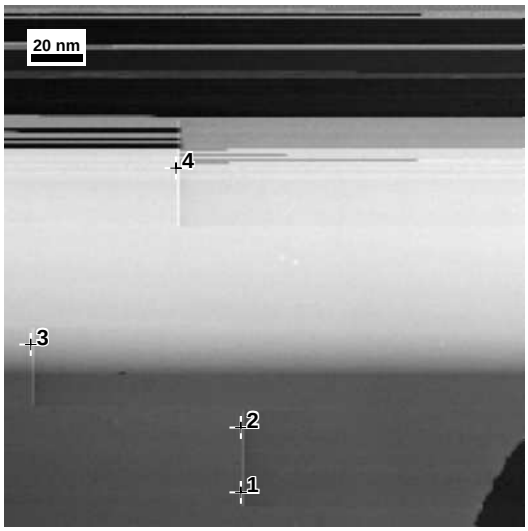

(a)

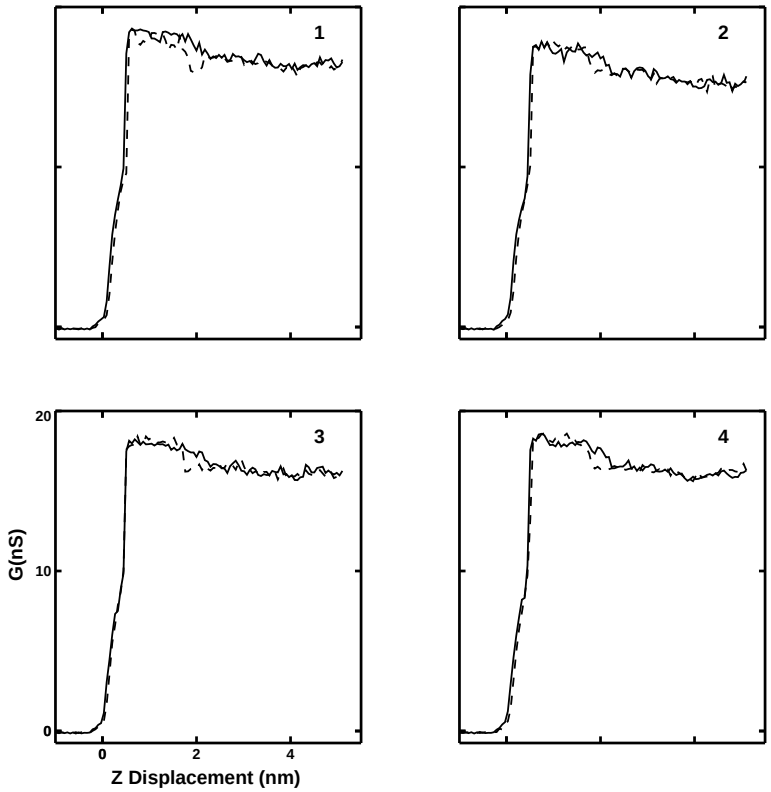

(b)

Figure 29: (a) A 200 $nm \times 200\ nm$ STM image of graphite using a Ga liquid tip at temperature 311 K ($R_{Ga} = 170\ \mu m$, setpoint $I_T = 100\ pA$, $V_T = 20\ mV$). (b) Conductance versus Z displacement at labeled spots in the above image.

The same Ga tip (R_{Ga} = 170 μm) was moved laterally by X=30 nm and Y= 20 nm from the previous position to go to a different topography on the surface of the graphite. Figures 30(a) and 30(b) show the image and $G(Z)$ spectra taken at different locations on the surface of graphite. The height of the step is 0.35 nm (one monolayer) and the width of the step is around 6 nm (3 nm contact radius).

The overall behavior of the conductance is similar to the previous ones. We observe a small conductance plateau (or inflection) near 5 nS in all the conductance spectra, but the conductance spectrum in '3' has larger span in Z-axis around 5 nS which is similar to the conductance in Fig. 28. We pushed the Z displacement up to 8 nm, which is larger than the previous Z displacement. We observe a second plateau around 18 nS which is consistent with the general behavior of the conductance measured at other positions on the surface. Note that the 5.5 nm hysteresis seen at position '4' is most likely due to a nearby step, faintly visible in the image. Spectra 2 and 3 show smaller hysteresis, perhaps from the step edge which lies between the two positions.

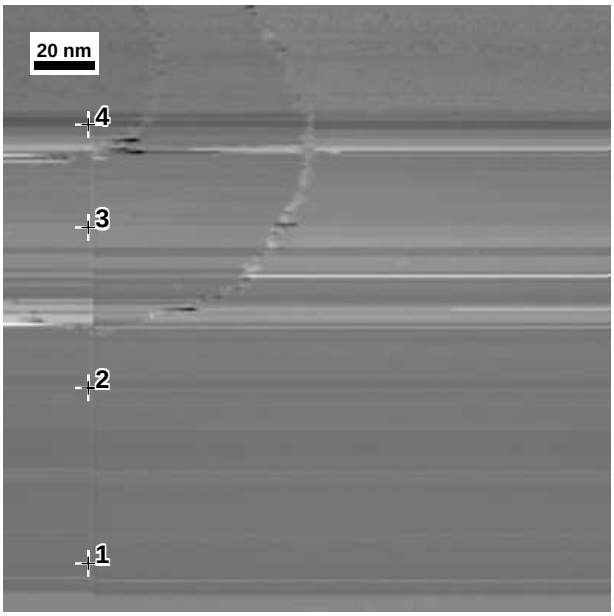

(a)

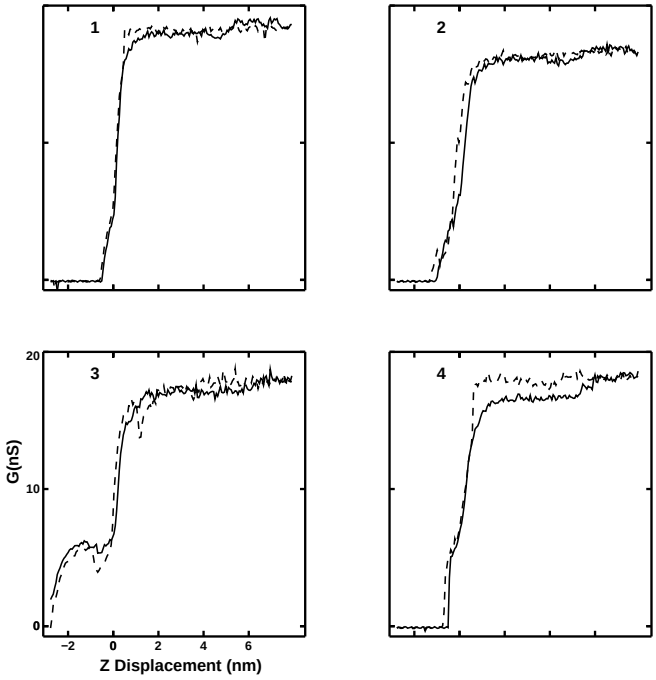

(b)

Figure 30: (a) A 200 $nm \times 200\ nm$ STM image of graphite using a liquid Ga tip at T = 311 K ($R_{Ga} = 170\ \mu m$, $I_T = 100\ pA$, $V_T = 20\ mV$). (b) Conductance versus Z displacement different spots in the above image.

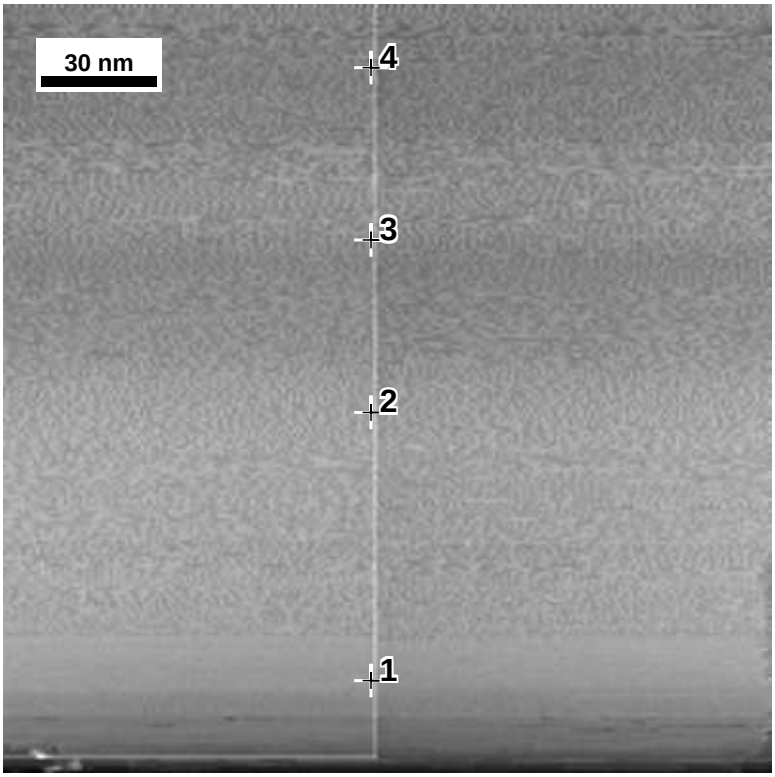

Figure 31: STM image of graphite surface (200 nm × 200 nm) by a liquid Ga tip at T = 311 K ($R_{Ga} = 157$ μm, $I_T = 100$ pA, $V_T = 20$ mV).

Figures 31 and 32(a) show the image and conductance versus Z displacement, respectively, for an experiment done with a different Ga tip of 157 μm radius. The current was not as stable as for previous tips, and for that reason the image is not as good as the previous images. However, the value of conductance at the plateau (18 nS) is similar to the previous Ga tip ($R_{Ga} = 170$ μm) and a shoulder at 4-5 nS is often observed. There is very small negative hysteresis between the forward and the reverse $G(Z)$ directions. We believe the source of the hysteresis is thermal drifting of the tip toward the surface.

We tried to see the behavior of the conductance beyond the plateau at 18 nS and we observed the forward conductance to increase almost linearly with Z displacement up to 125 nS (8 MΩ) as shown in Fig. 32(b). There is hysteresis between the forward and reverse directions, with the reverse conductance breaking contact 0.25 nm away from the forward conductance.

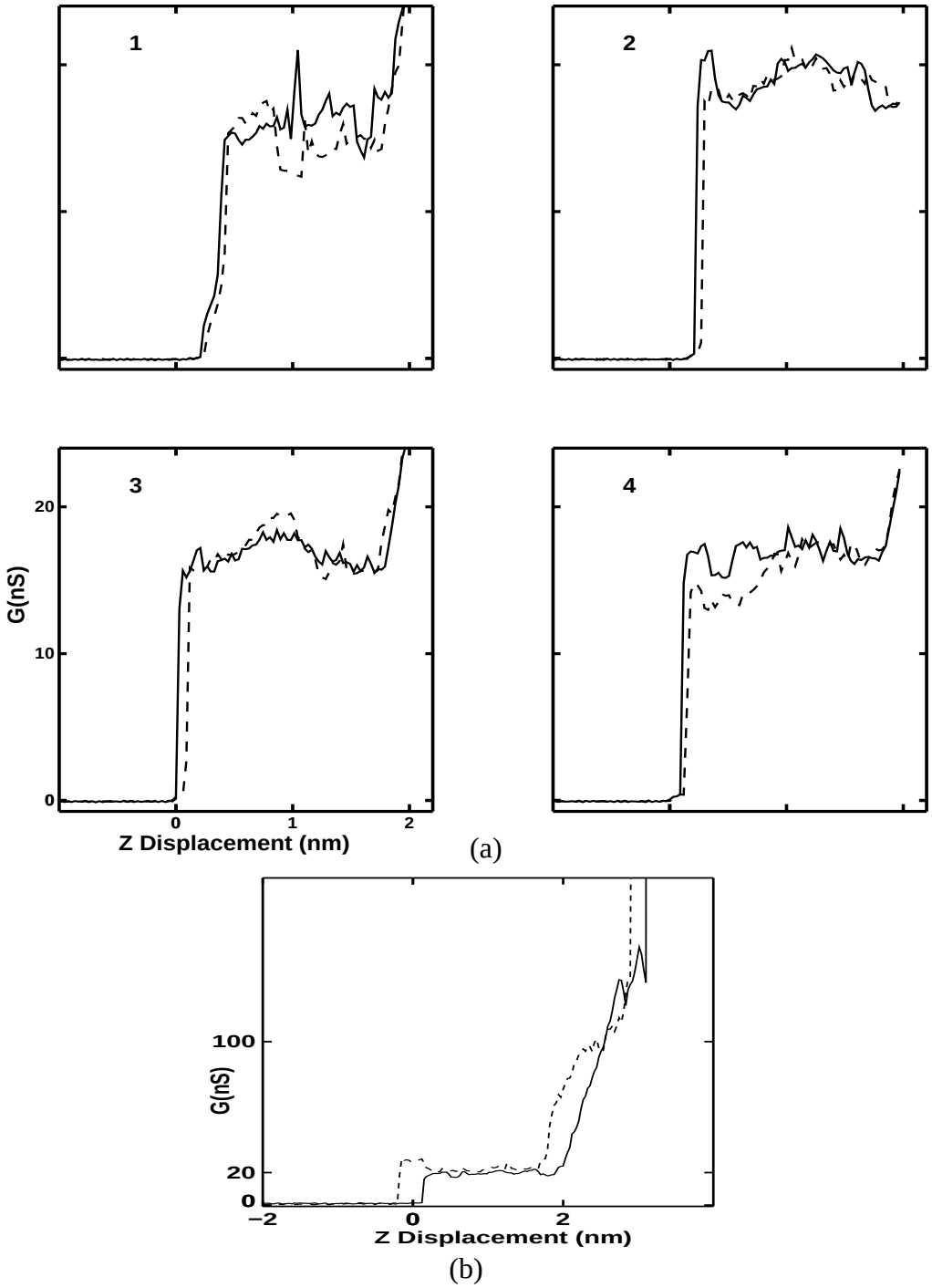

Figure 32: Conductance versus Z displacement between Ga tip and HOPG ($R_{Ga} = 157\ \mu m$, $I_T = 100\ pA$, $V_T = 20\ mV$). Solid line is forward and dashed line is reverse contact conductance (a) taken across the marked place on the image. (b) Contact conductance as function of tip displacement for larger displacement.

3.3 Imaging using a liquid tip

In this section we will examine the details of imaging the graphite surface using a liquid metal tip. STM images are usually acquired by a solid tip, but we managed to image the surface of graphite with a liquid Ga tip. The temperature of the STM was around 311 K in order to keep the Ga drop in a liquid state. The radius of curvature of the Ga drop was measured from the magnified image of the drop taken by a digital camera. But this curvature can not be the actual radius curvature of the drop under applied field. The formation of a "Taylor cone" under applied field is a well known phenomenon [109–112]. Beyond a critical field, the Taylor cone suffers a "jet" instability [110]. The typical potential between the drop and graphite was 20 mV (bias voltage of the tip). The applied field can be approximated from a parallel plate method. For a tip-sample separation of 0.5 nm, the electric field is about 4×10^7 V/m. This field is beyond the instability threshold (the minimum electric field for instability for a liquid gallium is around 5×10^6 V/m [112]). Consequently, we will not rely on the radius of curvature measured from the camera image for our analysis. The effective radius of the drop under applied field is on the nano-scale.

Due to the instability of a free drop under applied field, the liquid tip was in contact with the surface of the graphite in these images. A graphite surface was imaged previously by point-contact-microscopy [14] using a solid tip in contact with the surface during imaging. Figure 33 shows an atomic resolution image of HOPG under UHV conditions taken by a tungsten-carbide coated conductive AFM tip in contact with the surface (100 nN load). The image was taken with an average current of 945 nA and tip bias of 1 V. The lattice constant a is 2.46 $\mathring{A}$ measured from the image, consistent with imaging every other atom in the lattice. The contact radius was estimated to be about 4.1 nm from the width of atomic steps and the adhesive force was also estimated to be around 115 nN using a DMT contact mechanics model.

3.3.1 Imaging by 50 μm liquid tip

The graphite sample was annealed at about 1070 K for 15 min. prior to the experiment. In Fig. 34(a) is shown the image of graphite by a liquid drop with radius of curvature 50 μm.

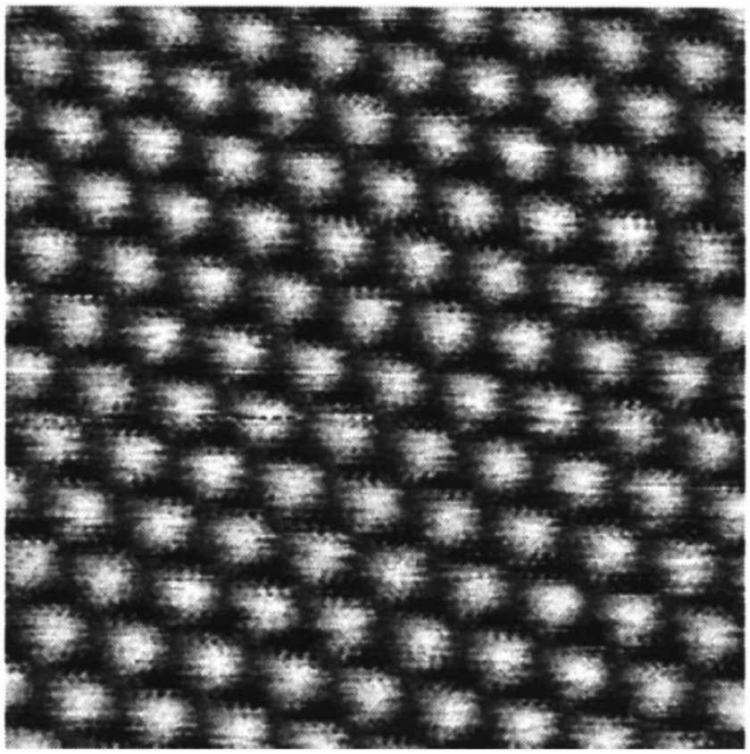

Figure 33: Point contact microscopy image of HOPG (25 Å× 25 Å) taken at 1 V bias voltage. It is taken from ref. [14].

The tip was in contact with the graphite surface during imaging, and the contact radius estimated from the width of the step edge of graphite is 2.5 nm (the contact diameter is approximately equal to the width of the step edge). The height of the step in Fig. 34(a) is 1.7 nm which is equivalent to five monolayers of graphite. The image shows many nanometer size islands on the surface, which are undoubtedly Ga nano-drops. We suspect these might be Ga that came out from the drop as drop-jets [110] when the field was high enough. For clean graphite which was annealed at high temperature the only source for these nano-drops should be from the Ga tip. We observed this behavior in many images with different tip size.

A higher resolution image of the graphite surface is shown in Fig. 34(b), corresponding to the boxed region in Fig. 34(a). Note that the drops bind to step edges and apparently to other defects. The long arc of the drop from bottom-right to top-left in Fig. 34(a) may be aligned on a low-angle grain boundary or subsurface dislocation line. The diameter of the Ga nano-drops are 3-4 nm which is close to the contact diameter estimated from the step

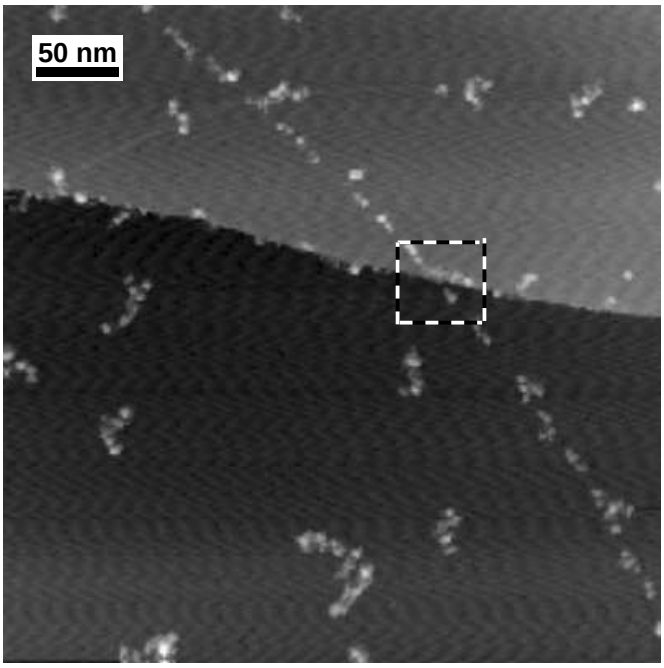

(a)

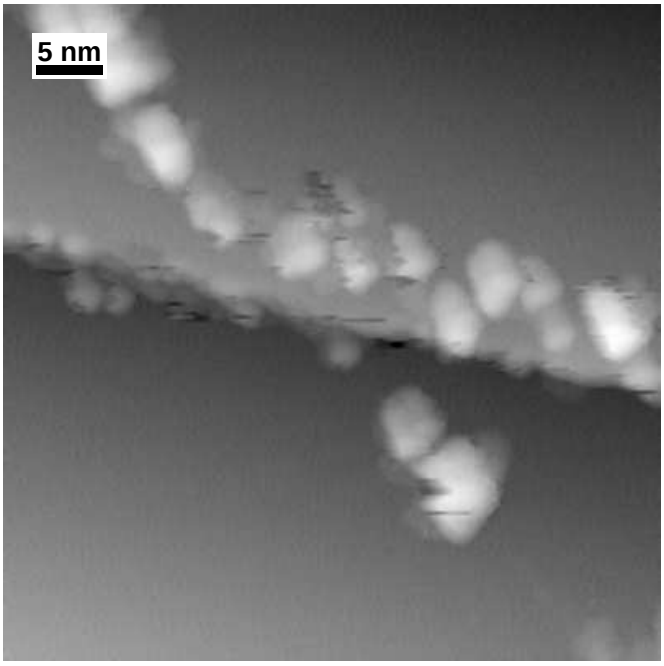

(b)

Figure 34: (a) A 400 $nm \times 400\ nm$ STM image of graphite using a liquid Ga tip at T = 311 K ($R_{Ga} = 50\ \mu m$, $I_T = 100\ pA$, $V_T = 20\ mV$). (b) A higher resolution (50 $nm \times 50\ nm$) STM image of graphite from the boxed region of part (a).

edge width. Four images were taken between Fig. 34(a) and 34(b) but the width (contact radius) did not change. This confirmed that the shape or size of the tip was not changed during the experiment. The bias voltage (applied field) was kept the same for all images, and due to that the contact radius or width of the step was not changed from one image to next.

3.3.2 Imaging by 180 μm liquid tip

The HOPG sample was annealed around 1170 K for 20 min. before the experiment. We used a different drop with a radius of curvature 180 μm and we imaged the surface of the graphite with the same tunneling current and bias voltage as previously. The image is shown in Fig. 35. There are many steps on this image, and we observe small Ga nano-drops predominantly along the step edges.

A high resolution image is shown in Fig. 36(a). The height of the step is about 3.3 $\mathring{A}$ which is one graphite monolayer step. The contact radius between the liquid tip and the graphite surface is estimated to be 1.75 nm from the step edge width. There are Ga nano-drops along the step edges in the image and Fig. 36(b) shows a profile across the nano-drops marked by a line on the image. The vertical axis is the height and the horizontal axis is the lateral size of the nano-drops. The diameters of the nano-drops are between 3 nm and 5 nm, very close to the contact diameter of the drop measured from the step-edge width. The best way to measure the diameter of solid nano crystals (like gold nanocrystals) or carbon nanotubes is by measuring the vertical height, which eliminates problems of the shape convolution. For liquid Ga this method may not give us the actual diameter of drop because the tip drop and the surface nanodrops may briefly coalesce. This could also affect the imaged lateral diameter. We measured the height of Ga nano-drops and obtained values between 1 nm and 1.7 nm which is somewhat smaller than the lateral radius. The average volume of the Ga nano-drop is about 70 nm^3.

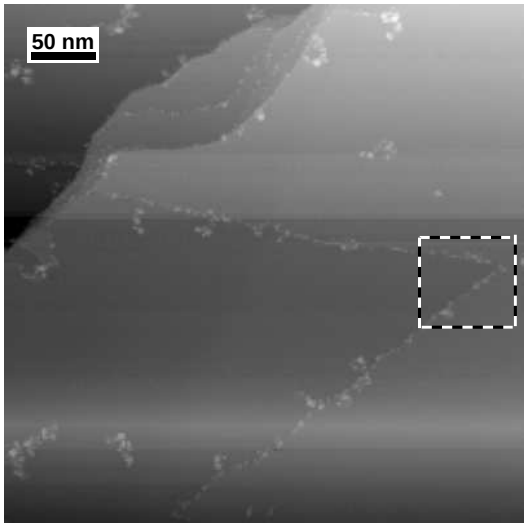

Figure 35: A 400 $nm \times 400\ nm$ STM image of graphite using liquid Ga tip at T = 311 K ($R_{Ga} = 180\ \mu m$, $I_T = 100\ pA$, $V_T = 20\ mV$). See the following figure for an expanded image within the outlined region.

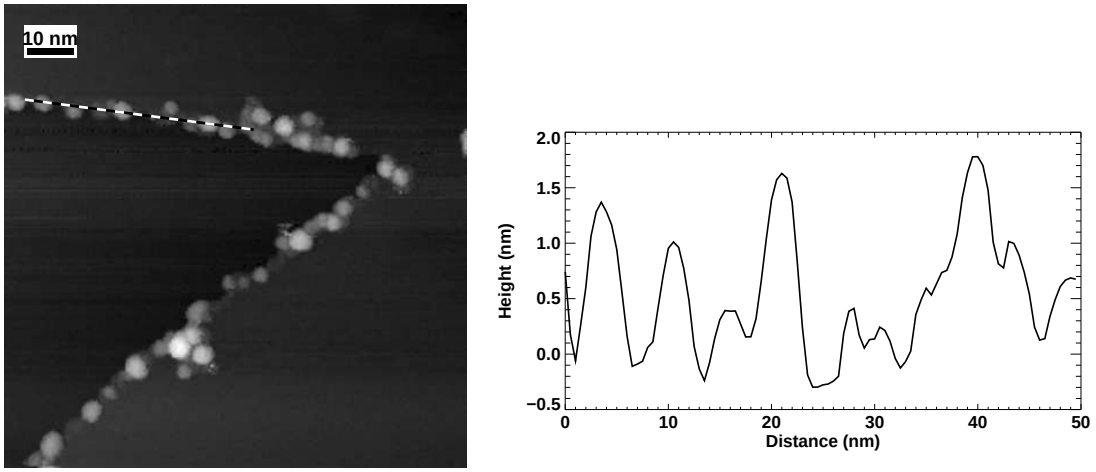

(a) (b)

Figure 36: (a) A 100 $nm \times 100\ nm$ STM image of graphite using liquid Ga tip at T = 311 K ($R_{Ga} = 180\ \mu m$, $I_T = 100\ pA$, $V_T = 20\ mV$). (b) Height profile of the Ga nano-drops along step edge, as labeled in the image. The image corresponds to the boxed region in the previous figure.

3.4 Discussion

In most contact experiments the load (force) $F(\delta)$ is measured as a function of the deformation displacement δ. But in our case, the contact conductance G was measured as a function of displacement Z. The deformation displacement $\delta = Z - Z_o$, where $Z - Z_o$ is the displacement at initial contact. A liquid Ga tip does not deform the surface of graphite during contact. But the contact area will increase as Z displacement increases. The contact force at the interface of Ga-HOPG can be estimated by the Young-Laplace equation. The estimated contact force was in range of 100 to 200 fN. This is 10 - 10^2 times less than the smallest forces achievable in commercial scanning force microscopes. we didn't observe exponential (tunneling) increase in most of our measurements; rather it started abruptly, then increases in a linear or sublinear manner during the approach to the graphite surface. This is associated with Ga drop instability.

The initial contact conductance is very small (a few nS), much less than G_0 . This might be due to momentum mismatch [113, 114] at the interface of the graphite and gallium. Figure 37 shows the approximate Fermi surfaces of graphite and gallium, projected on the k_x, k_y plane. The Fermi wave vector of Ga is 1.66 $\mathring{A}^{-1}$ for an infinite plane while for graphite the k-points in the BZ are located 1.7 $\mathring{A}^{-1}$ from the zero center. The only way electrons can transfer across a planar interface is through inelastic scattering.

We don't know for sure the source of this small contact conductance for small contact area. We know that very small Hg cluster behave like insulators and as the size of the Hg clusters increases the metallicity of the clusters increases [115]. This behavior also occurs in other small clusters of metals [116–118]. This behavior may be occurring in the liquid Ga drop. Small drops might behave like poor conductors and big drops might behave like good conductors. We don't have direct evidence about the size of the Ga drop and we cannot rely on the above arguments.

The appearance of conductance plateaus reminds one of conductance quantization in metallic wires. However, the observed conductance steps are not multiples of G_0, perhaps because the transmission coefficient is not unity ($T \neq 1$). One the other hand, as we showed in the previous section, there are Ga nano-drops on the surface. These Ga nano-drops could

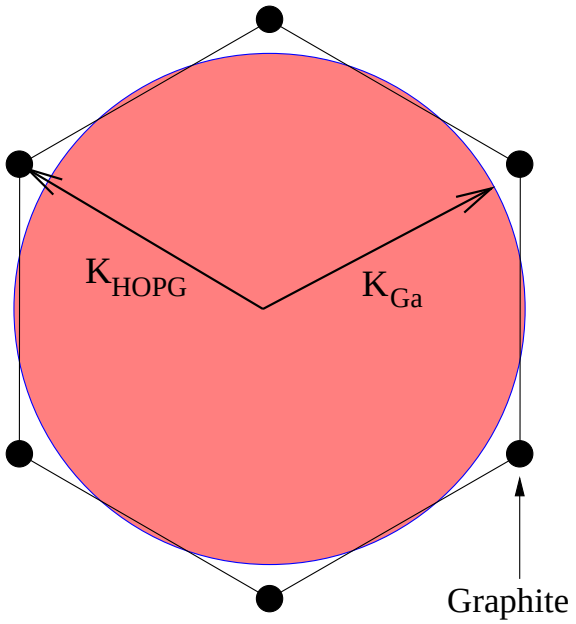

Figure 37: Fermi surface of graphite and gallium. The Fermi wave vector for Ga $K_{GA} = 1.66\ \mathring{A}^{-1}$ and for graphite the k-points K_{HOPG} in the BZ are located $1.7\ \mathring{A}^{-1}$ from the zero center.

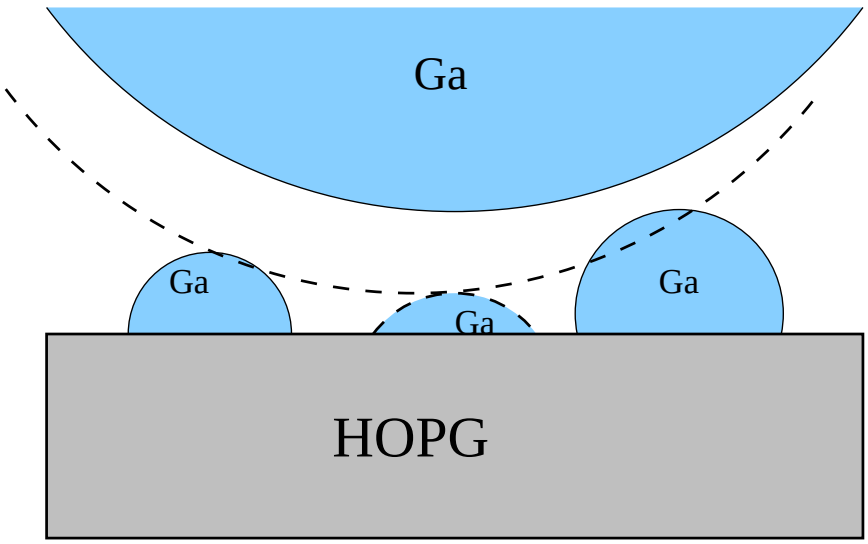

Figure 38: Model of contact between Ga tip and Ga drop on the surface of the HOPG.

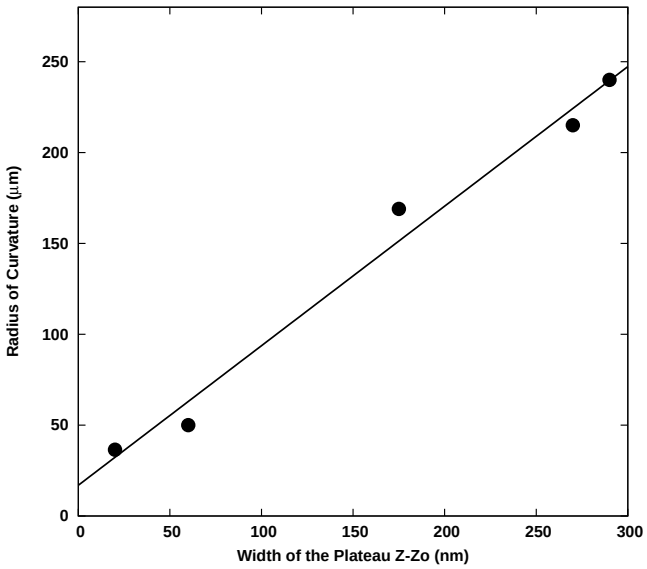

Figure 39: Radius of curvature of liquid Ga tip versus width of first plateau for the large Z displacements. The radius of Ga drops were estimated from the microscopic image of the drop. The experimental results are indicated by a solid circle and the linear fit to the data is shown by the solid line.

make successive contact with the Ga tip during contact conductance measurements. The model of this contact conductance is shown in Fig. 38. The conductance plateaus for large Z displacement (and large setpoint current) might be the result of contact between the Ga nano-drops (on the surface of graphite) and the Ga tip. This makes the contact between the same metal (Ga drop) rather than of Ga tip with a graphite surface.

Figure 39 shows the radius of the liquid Ga tip plotted as a function of the width of the first plateau. The data for the width of the plateau came from the conductance spectra with large displacements. The radius of the drop scaled linearly with the width of the first plateau. The slope of the linearly fit line is 0.768 ± 0.058. The change from initial conductance plateau to next plateau may be due to the applied force ($F = \frac{2\gamma}{R} \times A$) to the surface by the liquid tip. That is, it needs a critical threshold force to change from one plateau to the next. The contact radius is determined from the profile of the Taylor cone at bias voltage of 20 mV for all the liquid tip radii. This leads us that the force is inversely related to macroscopic radius R. Thus, for a given Z displacement the contact force is smaller for large R as compared with small R.

From imaging the graphite with a liquid tip, we observed that gallium came out from

the tip and deposited on the surface. Experimental results [110] for the drop-jet instability show that the droplet size does not depend on the initial radius of curvature. These Ga nano-drops most often deposited on the step-edges of the graphite. We observed from our profile the diameter of the Ga nano-drops are close to the contact diameter measured from the step width. It is clear from our image there are plenty of Ga nano-drops on the surface of graphite and there is a possibility the Ga tip can make contact either with graphite or Ga nano-drop or perhaps with both during a contact experiment.

CHAPTER IV

CONTACT CONDUCTANCE OF SOLID METAL TIPS

The contact conductance experiments started with liquid Ga tips. At the beginning of our work, we preferred the liquid tip for one simple reason: to have variable contact area without deformation of the surface of graphite. For small displacements, we observed very small contact conductance, to the order of 5 nS, and we believed that this small conductance might be due to momentum mismatch at the interface of graphite and Ga. That is, the projected Fermi wave vector for Ga $\mathrm{K}_{Ga} = 1.66\ \mathring{A}^{-1}$ is located inside the K-points of graphite $\mathrm{K}_{HOPG} = 1.70\ \mathring{A}^{-1}$. With this momentum mismatch, the only way for electrons to transfer across a planar interface would be through inelastic scattering, and due to that we observed very small conductance at the interface. We chose copper and aluminum to observe the effect of momentum mismatch at the metal-graphite interface. The Fermi wave vector for Cu $K_{Cu} = 1.36\ \mathring{A}^{-1}$ is located well inside the k-points of graphite. But for Al the Fermi wave vector $K_{AL} = 1.75\ \mathring{A}^{-1}$ is located outside the k-points of graphite, which allows phase-matching of Al states to those in graphite.

The pressure under a solid tip is much different than for the liquid tips, i.e. the contact force in solid metal tips is much larger than the liquid tips at the interface of graphite. We used the DMT model to estimate the contact force at the interface. Most of the experimental spectra are without (or small) hysteresis between forward and reverse conductance. Therefore, the DMT model [see details in Chapter I] was shown to be the best model for our experimental data. The contact radius and force were estimated by the DMT model using experimental deformation displacements and radius of curvature R of the tip. The radius R of the tips were measured via FEM. The solid metal tips were cleaned by sputtering [101] in Ne gas and annealed with e-beam heating. We also used sputtering for sharpening of the tips, as explained in Chapter II. In the next section, we will present and discuss experimental $G(Z)$ measurements of Cu tips with different tip radii. We will also present

contact area and force as estimated by the DMT model. In section 4.2, we will present and discuss experimental conductance spectra between Al tips and graphite.

4.1 Copper-HOPG Contact Conductance

4.1.1 20 nm Cu tip

A newly-cleaved HOPG sample was annealed at 1000 ^{o}C for 25 min. inside the UHV chamber before the contact experiment. The Cu tip was electrochemically etched as described in Chapter II. It was sputtered in Ne gas (pressure of 8.25×10^{-5} $mbar$) with an emission current of 5 μA. The Cu tip was sputtered for 2 min. The threshold voltage decreased from 600 V to 400 V during the sputtering. This was an indication that the tip was sharper after the sputtering. Finally, the tip was annealed by electron bombardment heating for 30 sec. at 1 kV with an emission current 1.32 mA. The radius of curvature of the tip was estimated from Fowler-Nordheim theory [103], as detailed in Chapter II.

An image of HOPG taken by the Cu tip with a 20 nm radius of a curvature is shown in Fig. 40(a). The profile across a triple step is shown in Fig. 40(b). The imaged height of the step is about 0.9 nm (three monolayers of graphite). The faint "ghost" step is not a real step, but results from double-tip imaging. All the $G(Z)$ in this Chapter were acquired simultaneously with the image, via the method of CITS [108]. Figure 41 shows the conductance versus tip displacement at four different regions labeled in Fig. 40(a). The initial conductance is very small, of order 5 nS (similar to the initial conductance step for the liquid Ga tips). Spectra 1 and 2 were taken far from the step as indicated in the image. These conductance spectra don't reveal any hysteresis between the forward and reverse conductance. However, spectra 3 and 4, which were taken near the graphite step, show some hysteresis between the forward and the reverse conductance traces.

We presented different contact mechanics models in Chapter II, and the DMT model was shown to be the closest model to our experiment. There are two main forces between contacting surfaces, i.e. the attractive (adhesive) and the repulsive (Hertz) forces. These two forces cancel one another when their magnitudes are equal. The contact radius a_o at

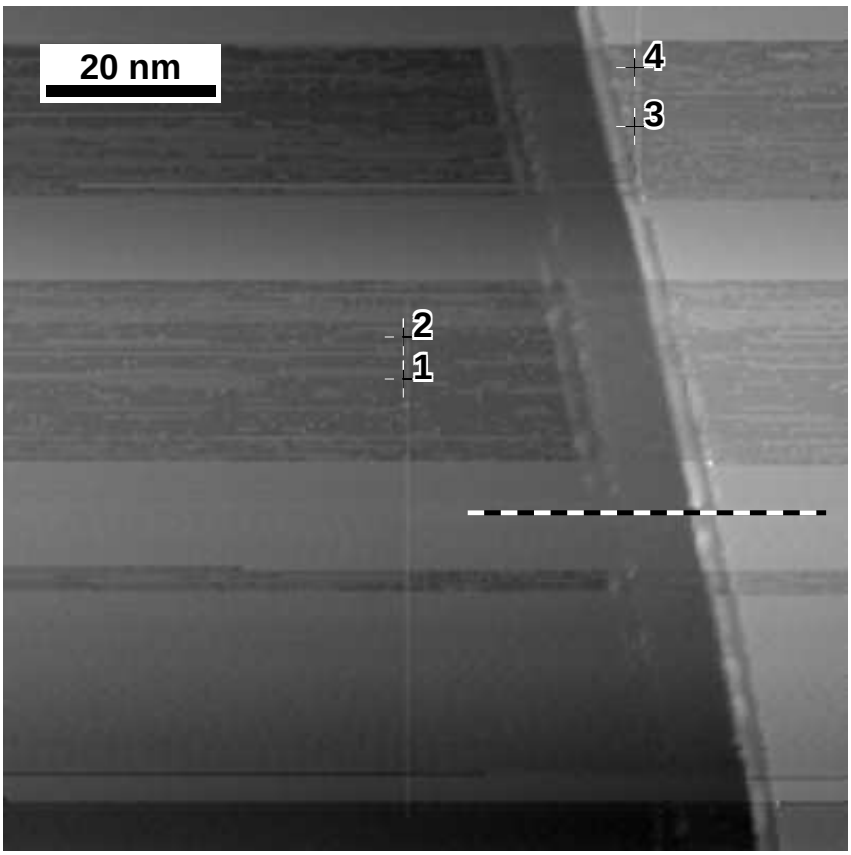

(a)

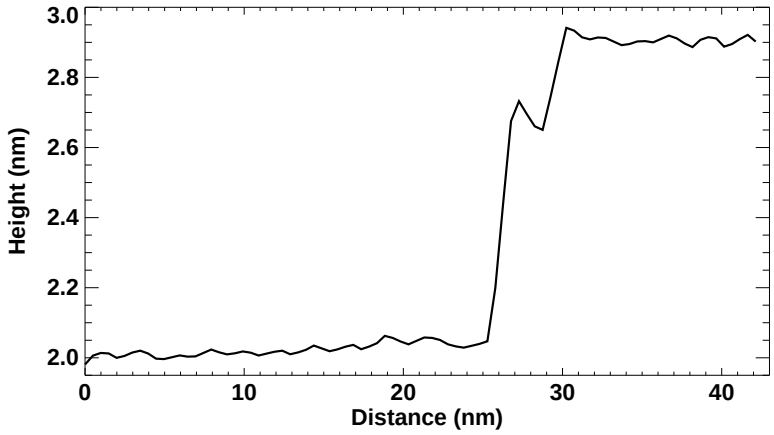

(b)

Figure 40: (a) Graphite surface (100 $nm \times 100\ nm$) imaged by a Cu tip with a radius of curvature $R = 20nm$ ($I_T = 100\ pA, V_T = 2\ V$). (b) Height profile of graphite across a step edge as labeled by the dashed line in the image.

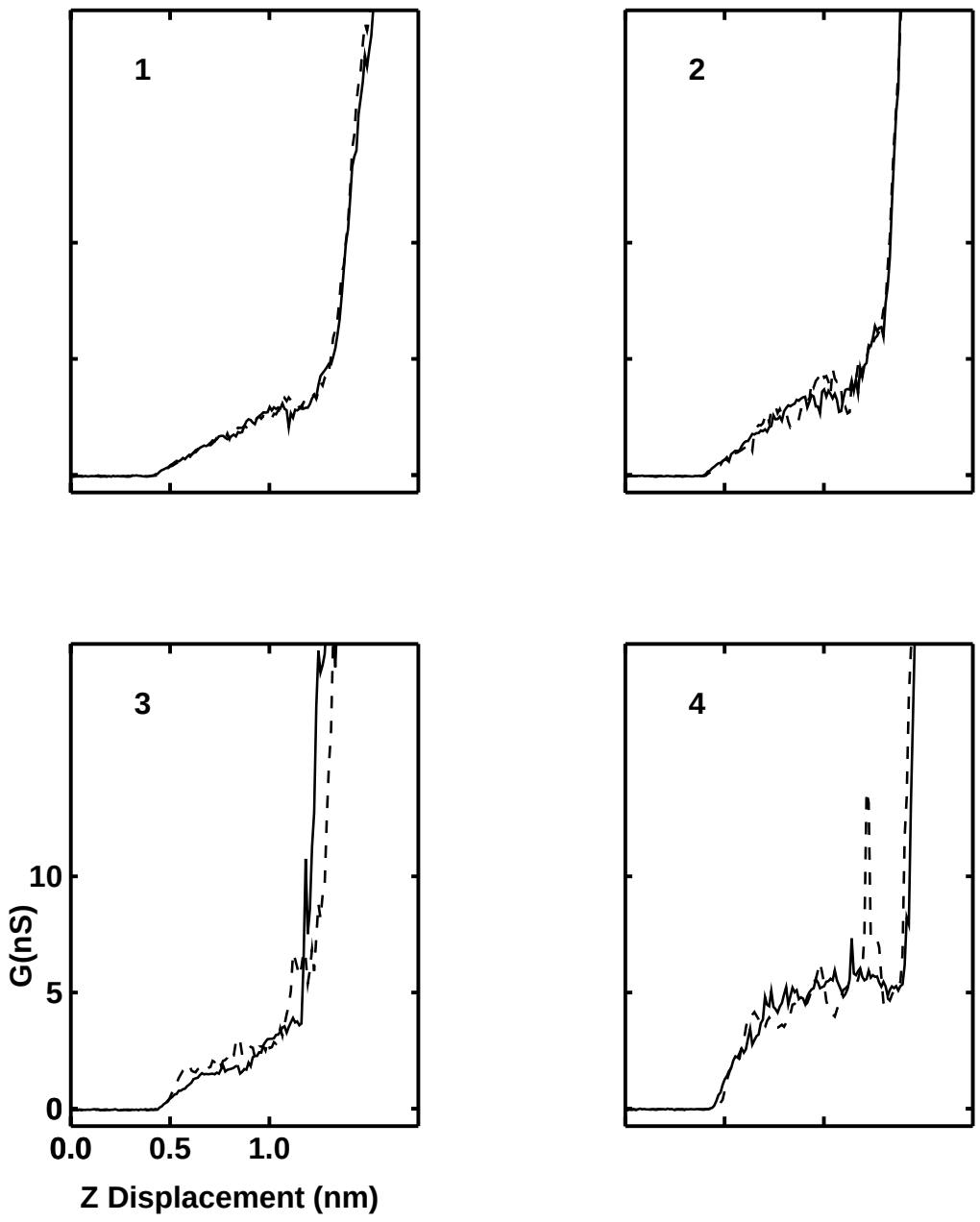

Figure 41: Measurements of conductance versus tip displacement ($R = 20nm$, $I_T = 100\ pA, V_T = 20\ mV$). The forward conductance is indicated by a solid line and the reverse by a dashed line.

zero force can be calculated from the DMT model (Eq. 31):

$$a_o = (\frac{2\pi w R^2}{E^*})^{1/3},$$

where w and E^* are the work of adhesion and the effective Young's modulus. From the formula and values in Tables 1 and 2, the contact radius a_o for a 20 nm tip is expected to be 3.4 nm (equivalent to 36.3 nm^2 contact area). Figure 42 shows a conductance spectrum versus contact area. The contact area ($a = \sqrt{R\delta}$; see Chapter II) was calculated from experimental deformation displacement δ using the DMT model. The deformation displacement δ taken to be the Z displacement from the conductive threshold, i.e. we obtained δ by shifting the Z displacement to zero such that $G(Z = 0) = 0$. Figure 42 shows that the initial conductance increases linearly up to a contact area of 40 nm^2 before it briefly plateaus and then increases rapidly to higher conductance.

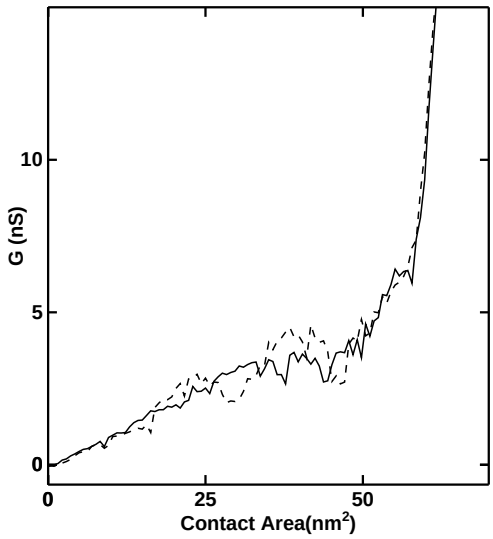

Figure 42: Contact conductance versus contact area between Cu tip and graphite surface (R = 20 nm, I_T = 100 pA, V = 20 mV). The forward conductance is indicated by a solid line and the reverse by a dashed line. This data is from spectrum in Fig. 41.

In Fig. 43 is shown the same conductance spectrum plotted versus force. The force is obtained from the DMT model using the experimental deformation displacement. Negative force in the figure occurs when the attractive force is larger than the repulsive force. In this regime the surface of the tip and graphite are under overall tensile stress. We expect that the interlayer separation of the graphite will increase from its natural spacing. A positive

force means that the repulsive force dominates the attractive force. For this regime both the tip and sample will be deformed under the compressive stress. The interlayer separation of the graphite will decrease from its natural separation. In this regime the conductance increases faster [119].

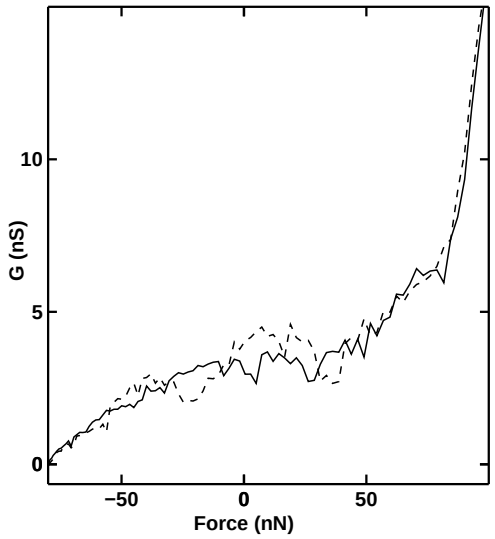

Figure 43: Contact conductance versus force between Cu tip and graphite surface (R = 20 nm, $I_T = 100\ pA, V = 20\ mV$). The forward conductance is indicated by a solid line and the reverse by a dashed line.This data is from spectrum in Fig. 41.

After the contact measurements the radius of the tip was again characterized via field emission current-versus-voltage measurements. In this case radius of curvature of the tip was about 31.3 nm, which is larger than the radius before the experiment (20 nm). Apparently the tip either deformed plastically or possibly picked some graphite flakes during contact with graphite. The graphite surface apparently deformed elastically because there was no visible change in the image of the graphite taken after the $G(Z)$ measurements. The $G(Z)$ spectra also show almost no hysteresis.

4.1.2 44 nm Cu tip

The HOPG sample was annealed at 975 ^oC for 10 min. The Cu tip was sputtered at 5 μA emission current with Ne gas (base pressure $6.93\times10^{-5}\ mbar$) for 3 min. It was also annealed by e-beam for 1 min. with an emission current 1.98 mA. The radius of the tip (44 nm) was measured using the Fowler-Nordheim theory. Figure 44(a) shows one representative

spectrum from a total of 134. The conductance spectra were very reproducible and without hysteresis. The general behavior of the data between 0-5 nS is similar to the previous conductance spectra. The conductance increases in linear or sublinear form up to 5 nS. The conductance increases very dramatically after 5 nS. This behavior was also observed with the 20 nm Cu tip.

The apparent barrier height of the tunnel barrier ϕ_{ap} is define as [120, 121]

$$\phi_{ap} = \left(\frac{1}{1.025} \frac{d \ln(I)}{dZ} \right),$$

where Z is displacement in $\mathring{A}$ and ϕ_{ap} is in eV. Figure 44(b) shows the apparent barrier height as function of Z displacement. The barrier height starts at a very high value compared to the 4.4 eV average work function of Cu and Al and then collapses very rapidly to zero within 0.15 nm Z displacement.

Figure 45 shows the conductance spectrum versus contact area (πa^2). The contact radius a is estimated from the DMT model using experimental deformation displacement δ and radius of a curvature R of the Cu tip. The conductance increases almost linearly with contact area up to 5 nS. But beyond 5 nS it increases drastically. The contact area at 5 nS conductance is about 110 nm^2.

In Fig. 46 is shown the conductance spectrum as a function of force. The force is calculated from the DMT model using the experimental deformation displacement. The conductance increases with force sublinearly from -150 nN to 25 nN. The adhesive force dominates for a conductance less than 4 nS. However, the repulsive force dominates for a conductance beyond 4 nS. The conductance starts to increase very dramatically around 25 nN force. We believe that at this force and beyond the layers of graphite begin to deform from their natural distance enough to affect transport perpendicular to the layers.

The radius of curvature of the tip was measured by FEM to be 66 nm at the end of the contact experiment. The radius of the Cu tip increased from the radius before the experiment (44 nm). The same physical change was also observed with the previous Cu tip (20 $nm \rightarrow$ 31 nm) for similar Z displacements. The Cu tip apparently undergoes plastic deformation during the contact experiment. The surface of the graphite was observed to

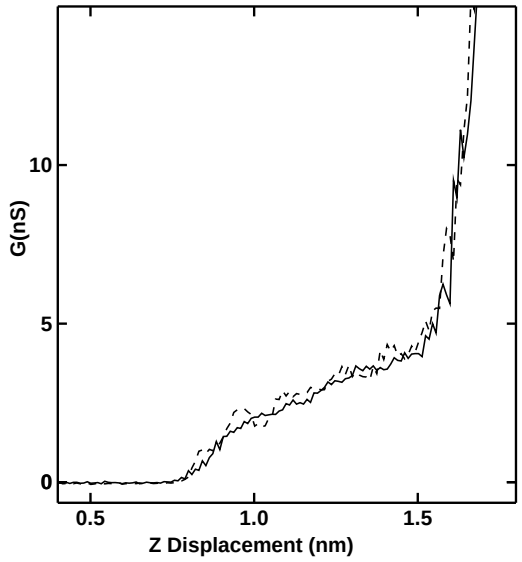

(a)

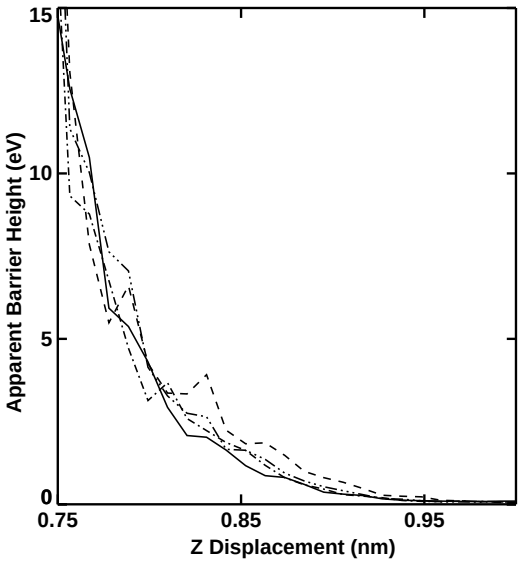

(b)

Figure 44: (a) Contact conductance versus tip displacement ($R = 44\ nm$, $I_T = 100\ pA, V_T = 20\ mV$. (b) Apparent barrier height versus Z displacement, four different spectra are taking as representative and indicated by different line styles.

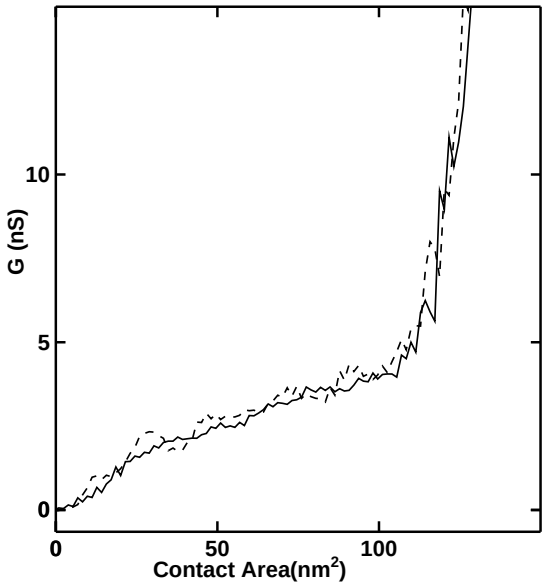

Figure 45: Contact conductance versus contact area between Cu tip ($R = 44nm$) and HOPG surface. The set current was 100 pA and the bias voltage was 20 mV. The forward conductance is indicated by a solid line and the reverse by a dashed line.

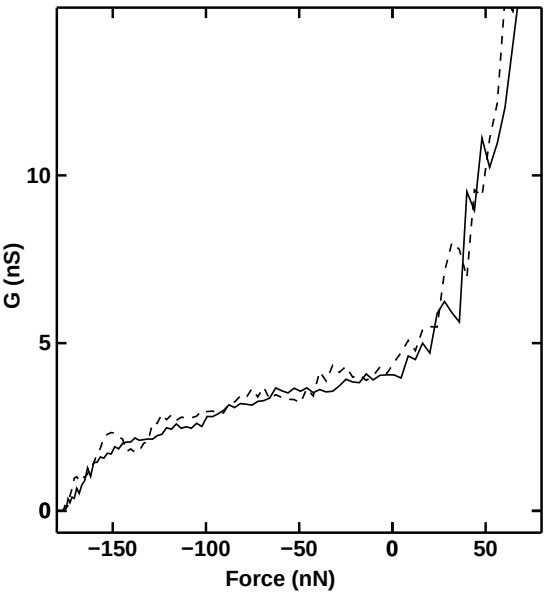

Figure 46: Contact conductance versus force of Cu tip with HOPG surface ($R = 44\ nm$, $I_T = 100\ pA$, $V = 20\ mV$). The forward conductance is indicated by solid line and the reverse by a dashed line. The force is estimated from the DMT model.

remain the same. Thus, images before and after the $I(Z)$ measurements were identical. That is, there was no any physical change on the surface from one image to the next. We came to the conclusion that graphite deforms elastically. The $G(Z)$ curve is also without hysteresis between the forward and reverse directions. Graphite is classified as soft material with Young's modulus 36.5 GPa (c direction). This property of graphite support our conclusion.

4.1.3 130 nm Cu Tip

A Cu tip was sputtered in Ne gas (pressure 1.32×10^{-4} $mbar$) at emission current 5 μA for 8 min. The threshold voltage dropped from 2.7 kV to 1.9 kV during the sputtering, indicating that the tip became sharper and cleaner during the sputtering process. This tip was annealed by electron bombardment heating for 45 sec. at 1 kV with emission current 0.65 mA. Emission current as a function of applied voltage was measured for tip profiling via Fowler- Nordheim. The radius of tip was 130 nm, substantially larger than previous tips.

Figure 47 shows the conductance measurements as a function of Z displacement. The overall behavior of the conductance spectrum is similar to previous conductance spectra obtained with the smaller tips. The initial conductance occurs at a larger displacement (Z=1.2 nm) as compared to the smaller tips. However, the conductance values are similar. This could be a consequence of the pressure ($P \propto \frac{1}{a^2}$) for a large tip being smaller than for a small tip at a given Z displacement.

Figure 48(a) shows the conductance versus contact area. The contact radius is estimated from the measured deformation displacement using the DMT model. The overall behavior of the conductance spectrum with contact area is similar to the smaller tips, but the contact area is larger for a similar conductance spectrum as compared to the smaller tips.

Figure 48(b) shows the conductance spectrum as a function of calculated force. The force is estimated from the DMT model, as for the smaller tips. In the initial conductance region, the force is dominated by attractive force. That is, at the start of the contact the force is about -500 nN. In the DMT model, the force includes long-range surface forces that exist outside the contact area. Therefore, for larger tips the contribution to the attractive

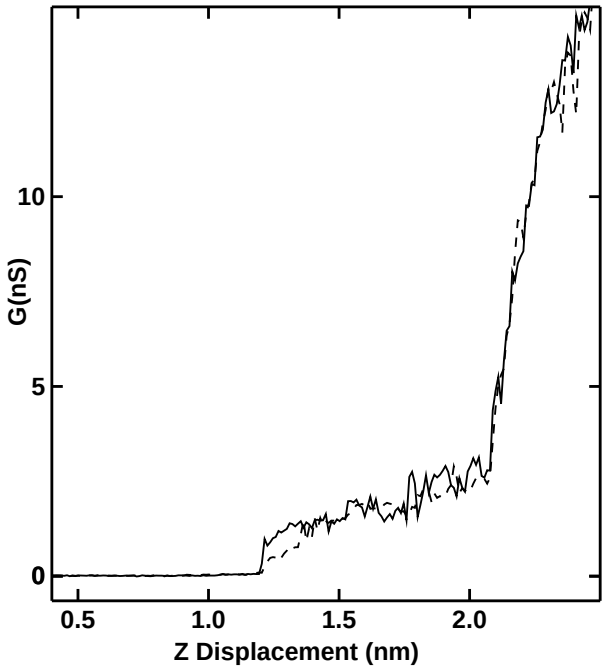

Figure 47: Measurements of contact conductance as function of tip displacement between Cu tip and HOPG surface ($R = 130\ nm$, $I_T = 100\ pA, V_T = 20\ mV$). The forward conductance is indicated by a solid line and the reverse by a dashed line.

force from outside the contact area is substantially larger than for smaller tips. It is possible to have local deformation of the graphite surface even in the attractive regime. For that reason in Fig. 48(b), the dramatic increase of the conductance could be due to compression of the graphite layers immediately under the tip apex.

4.1.4 39 nm Cu tip

Figure 49 shows conductance as a function of tip displacement for a Cu tip with radius of curvature 39 nm. We present one representative spectrum from many spectra. The conductance spectra were relatively reproducible. Figure 50(a) shows $I(V)$ the spectra evaluated at different Z displacements. The $I(V)$ were taken at 0.4 nm, 0.6 nm, 0.8 nm and 1 nm Z displacements. In Fig. 50(b) is shown the differential conductance (dI/dV) for the above $I(V)$. The dI/dV is calculated numerically. The dI/dV spectra are fairly symmetric, as seen in the figures, but the minima of the dI/dV spectra are shifted to -15 mV negative tip bias at zero voltage. The value of dI/dV at zero voltage is not zero. The shift

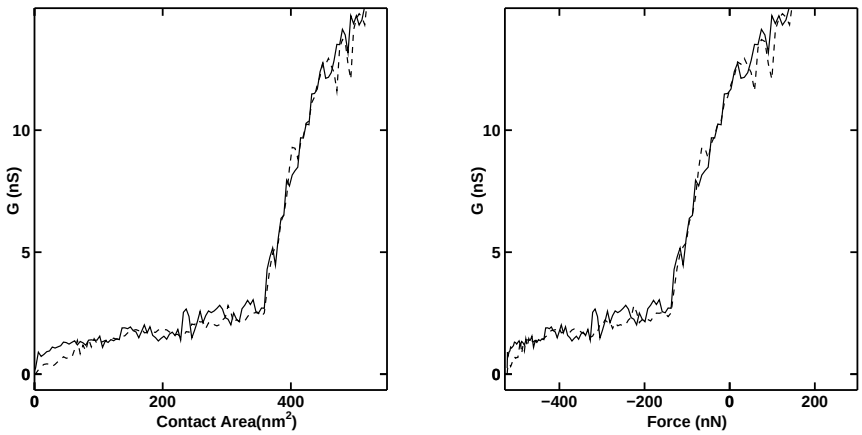

(a) (b)

Figure 48: Contact conductance Cu-to-graphite ($R = 130$ nm, $I_T = 100\ pA$, $V = 20\ mV$). (a) Conductance versus contact area. (b) Conductance versus force. The contact area and force are estimated from the DMT model using the experimental deformation distance. The forward conductance is indicated by a solid line and the reverse by a dashed line

in minimum of dI/dV spectra might be due to the pressure applied to graphite surface, i.e the interlayer spacing is compressed as the pressure increases with Z displacement. This behavior was observed in theoretical simulations (Kilic et al. [119]). As the graphite layers deformed, the interlayer separation became very close, and as a result the conductivity of the graphite increased.

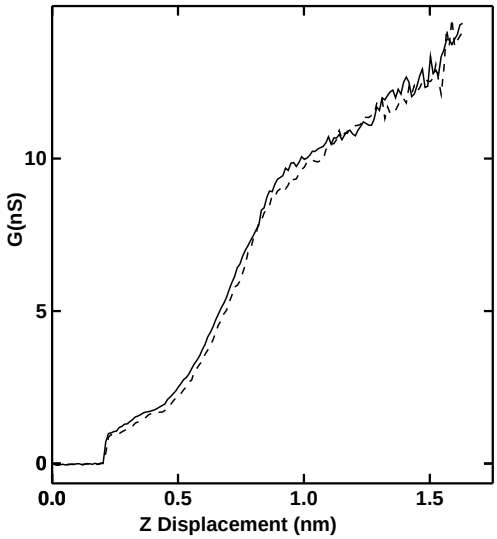

Figure 49: Contact conductance versus tip displacement between Cu tip and HOPG surface ($R = 39\ nm$, $I_T = 100\ pA$, $V_T = 20\ mV$). The forward conductance is indicated by a solid line and the reverse by a dashed line.

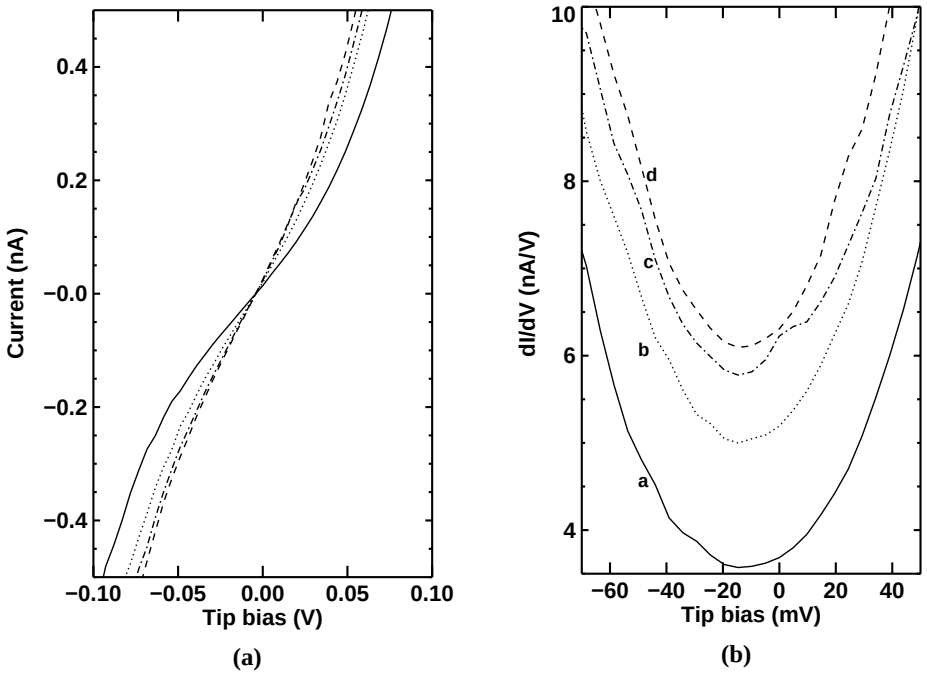

Figure 50: (a) $I(V)$ spectra at different tip displacements of the Cu tip ($R = 39\ nm$, $I_T = 100\ pA$). (b) The differential conductance (dI/dV) of the spectra in Fig. 50(a) taken at different tip displacements (a=0.4 nm, b=0.6 nm, d=0.8 nm, and c=1 nm; note a, b, d, c order).

4.1.5 Discussion

Figure 51 shows conductance spectra versus Z displacement for Cu tips different radii. The Z displacement for R=20 nm, 44 nm and 130 nm tips in the figure were shifted by 0.4 nm, 0.75 nm and 1.2 nm, respectively, to adjust deformation displacements [$G(\delta = Z - Zo = 0) = 0$]. The dramatic increase in the conductance spectra occurs at almost the same displacement for all of these tips. The overall behavior of the conductance spectra for different radii are similar. The initial contact conductance at the short plateau was observed around 3-5 nS for most of the Cu tips with different radii.

Figure 52 shows the *logarithm* of the conductance as a function of Z displacement for the 130 nm Cu tip. Most of the $G(Z)$'s were taken at 20 mV and tip bias 2 V. But, the $G(Z)$'s in Fig. 52 were taken at the same voltage as the imaging bias voltage. The $G(Z)$ data were acquired at 20 mV, 0.25 V and 0.5 V. The initial conductance occurs at negative displacements (negative displacements shows that the tip is in contact during low-bias imaging), before the servo-determined initial position of the tip. This behavior was also observed for liquid Ga tips with low bias voltage. The slopes for different bias voltages align at the same Z position. The slope jumped to next slope at the same displacements for all the bias voltage. Thus, the overall behavior at different bias voltage is similar.

In most AFM measurements, the force is measured as a function of displacement. But in our experiments, we measured contact conductance as a function of Z displacement. The contact radius a was estimated by the DMT model using the radius of curvature R and deformation displacement δ ($a = \sqrt{\delta R}$). The force was also calculated using experimental deformation displacements. The force was in the range typical of commercial scanning force microscopes.

From the Young's modulus of Cu and HOPG, we found that Cu compressed less than graphite for a given displacement. Thus, graphite deformed 0.78δ for a given deformation displacement δ, but Cu deformed 0.22δ. This follows from the Hertz forces [$F_h = E^* R^{1/2} \delta^{3/2}$; Eq. 19 from Chapter II]. It is hard to know deformation of each layer of the graphite but most of the deformation would occur within the first several layers.

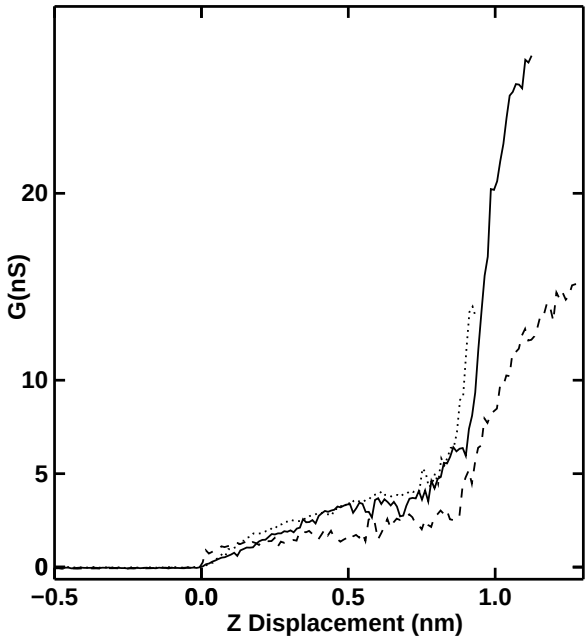

Figure 51: Conductance versus tip displacement for different tip radii (solid line for $R = 20$ nm, dotted line for R=44 nm and dashed line for $R = 130$ nm). $V_t = 20$ mV, $I_t = 100$ pA.

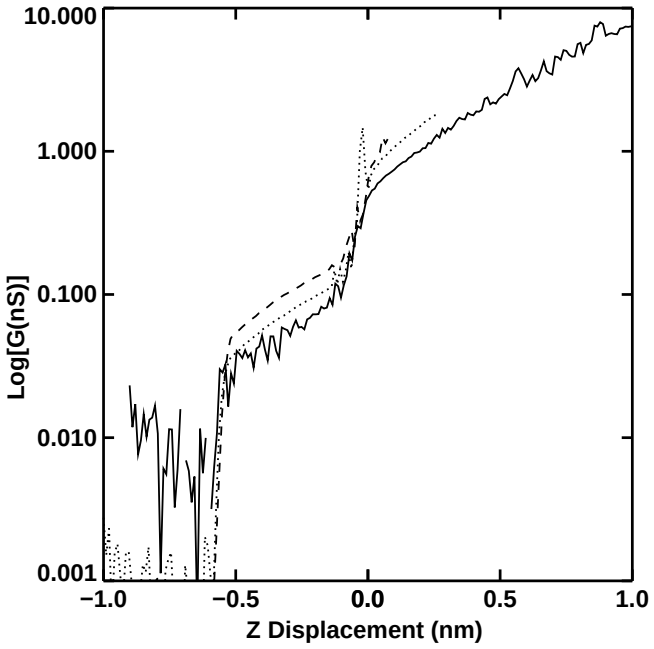

Figure 52: Logarithm of contact conductance plotted versus tip displacement. Solid, dotted, and dashed lines are represents 20 mV, 0.25 V and 0.5 V bias voltage respectively. ($R = 130$ nm, $I_t = 100$ pA). The spectra have been shifted in Z to align similar features.

We believe that the graphite deformed elastically during contact with tip. The separation of the graphite layers decreases during contact, but returns to the original separation when the contact is broken. There was no evidence of plastic deformation on images of graphite taken after the $G(Z)$, i.e. the image was similar in topography to the image taken before the $G(Z)$. The profile of the tip after the contact experiments indicated that the radius increased. The tip may deform plastically, or perhaps it picked up carbon atoms during the $G(Z)$ measurements.

4.2 Al-HOPG Contact Conductance

4.2.1 128 nm Al tip

All of the Al-HOPG contact conductance measurements were done under the same environment as in the cases of Ga and Cu tips. The Al tip was cleaned by a similar method as used for the Cu tip. The tip was sputtered at emission current 5 μA for a few min. in Ne gas and annealed by e-beam heating (1.32 mA, 1 kV, 40 sec.). The radius of curvature was estimated from Fowler-Nordheim theory. The graphite was annealed for 20 min. at 1100 ^oC prior to the contact experiments. All the $G(Z)$ were acquired simultaneously with the image via the method of CITS. In Fig. 53(a) is shown the image of the graphite taken at 2 V bias and a tunnelling current of 100 pA. The profile of the step edge is shown in Fig. 53(b). The height of the step is 3.35 Å, which is one monolayer of graphite.

Figure 54(a) shows four representative spectra taken at different regions on the image. The $G(Z)$'s were acquired at 20 mV but the bias voltage for imaging was 2 V. The four $G(Z)$ are indicated in Fig. 53(a). There is a clear initial conductance plateau around 12-20 nS for most of the $G(Z)$ spectra. In most of them the hysteresis between the forward and reverse conductance spectra is small, but not zero. Very small conductance ($<$1 nS) is observed in the reverse direction in some of the spectra (see e.g. spectra 2 and 3). Figure 54(b) shows an STM image of graphite taken after the $G(Z)$ measurements. This image is identical with the image taken during $G(Z)$ [Fig. 53(a)], which demonstrates that the graphite surface was deformed elastically.

We present a single representative spectrum for analysis of barrier height, area and force. Figure 55(a) shows conductance versus tip displacement. In Fig. 55(b) is shown apparent barrier height (in eV) as a function of tip displacement. The barrier height starts at a very high value compared to the 4.28 eV work function of Al, and then collapses continuously to zero over $\sim$0.2 nm. For a metal-to-metal contact [62, 122, 123], when the barrier completely collapses electrons can pass freely from one region to the other through the resulting 1D channel, and the conductance occurs in integer multiples of the quantum of conductance ($G_o = 2e^2/h$). For our case, the interface is metal-to-graphite and the conductance is only 1.5×10^{-4} Go at the plateau.

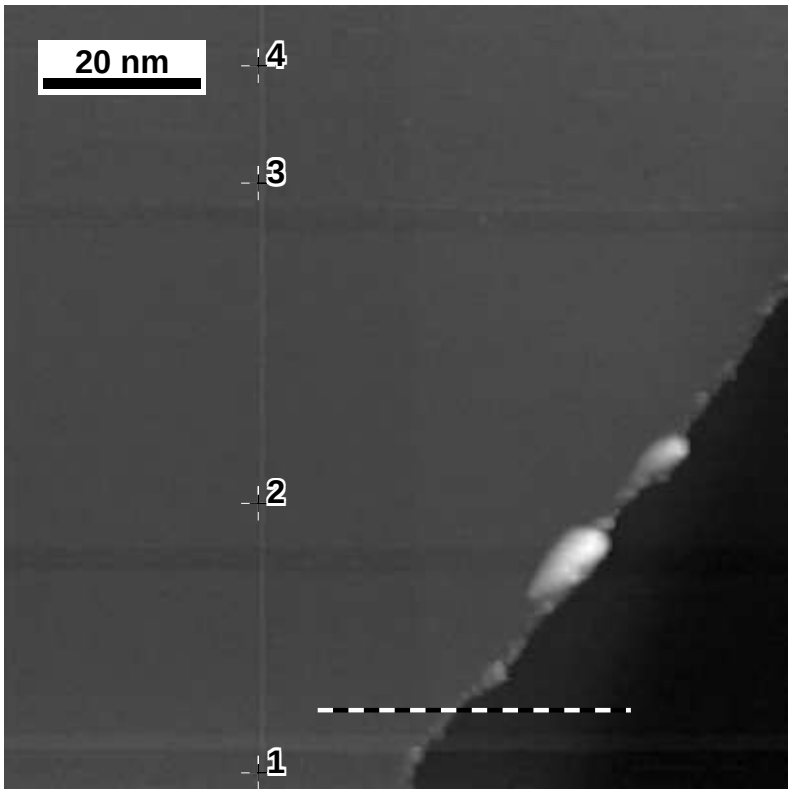

(a)

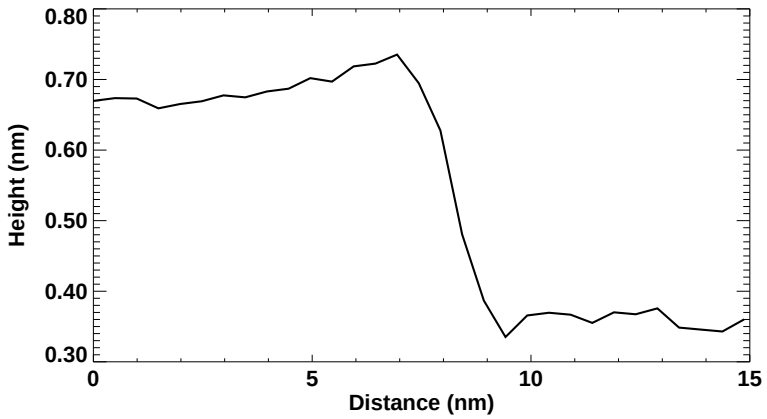

(b)

Figure 53: (a) STM image of graphite (100 $nm \times 100\ nm$) was taken simultaneously with $G(Z)$ spectra ($R = 128\ nm$, $V_{sample} = 2$ V, $I_T = 100\ pA$). 197 spectra were acquired; those from positions 1-4 are shown in Fig. 54(a). (b) Profile of the step marked on the image. The step height is about 3.35 Å (one atomic layer).

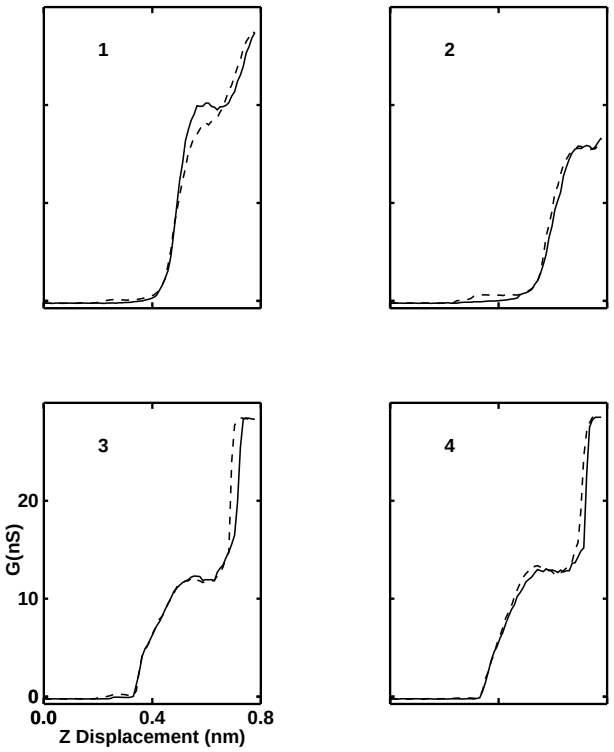

(a)

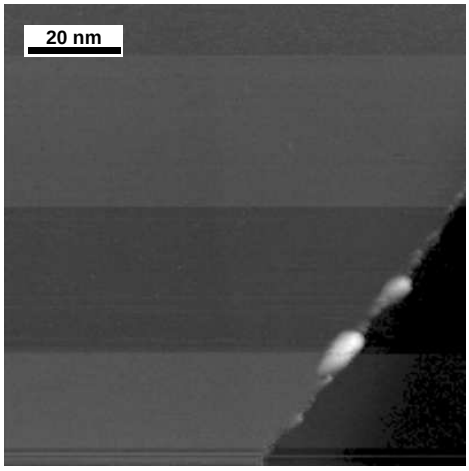

(b)

Figure 54: (a) Conductance versus tip displacement between Al tip and HOPG surface ($R = 128\ nm$, $I_T = 100\ pA$, $V = 20\ mV$). The forward conductance is indicated by a solid line and the reverse by a dashed line. Spectra 1-4 correspond to positions marked in Fig. 53(a). (b) STM image of graphite ($100\ nm \times 100\ nm$) taken after $G(Z)$.

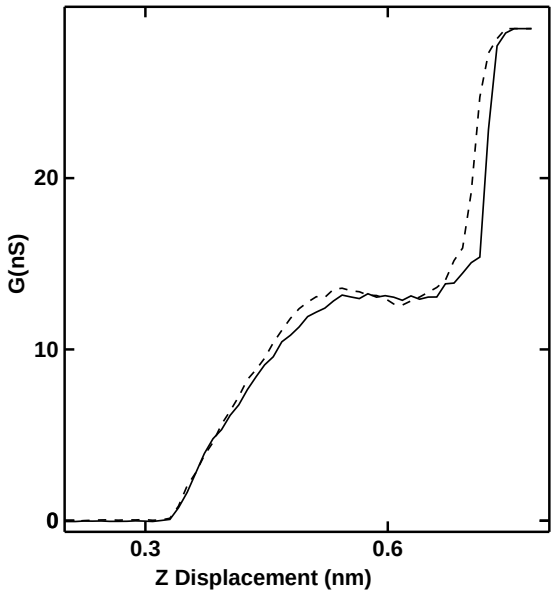

(a)

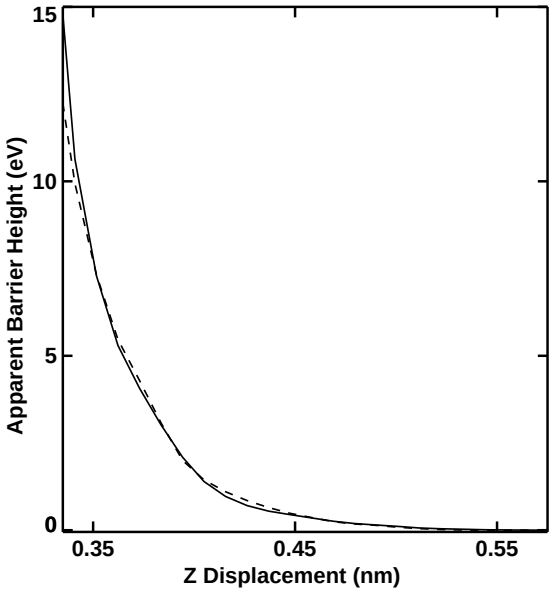

(b)

Figure 55: (a) Contact conductance versus Z displacement between Al tip and HOPG (R = 128 nm, I_T = 100 pA, V = 20 mV). Data from spectrum 4 in Fig. 54(a). (b) Apparent barrier height versus Z displacement. Solid line represents forward conductance and dashed line represents reverse direction.

Figure 56(a) shows the conductance spectrum versus contact area. The contact radius is estimated from the DMT model using the experimental deformation displacement δ and radius of curvature of the tip. For this particular tip the contact area at the plateau goes from 75 nm^2 to 150 nm^2. In Fig. 56(b) is shown the conductance spectrum versus force. The applied force is calculated from experimental $G(Z)$ data using the DMT model. In the $G(F)$ spectra, the adhesive force (attractive) is the dominant force for the entire range of Z displacement. In $G(Z)$ spectra [Fig. 55(a)] the maximum displacement is very small (< 0.8 nm). This small deformation displacement δ would result in a small repulsive force ($F_h = E^* R^{1/2} \delta^{3/2}$).

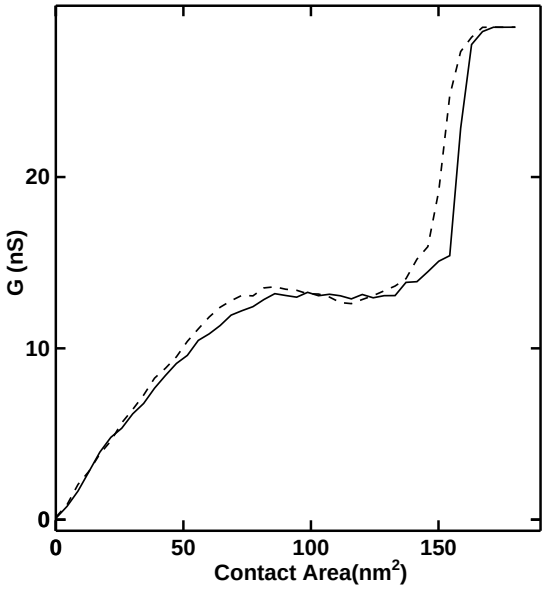

(a)

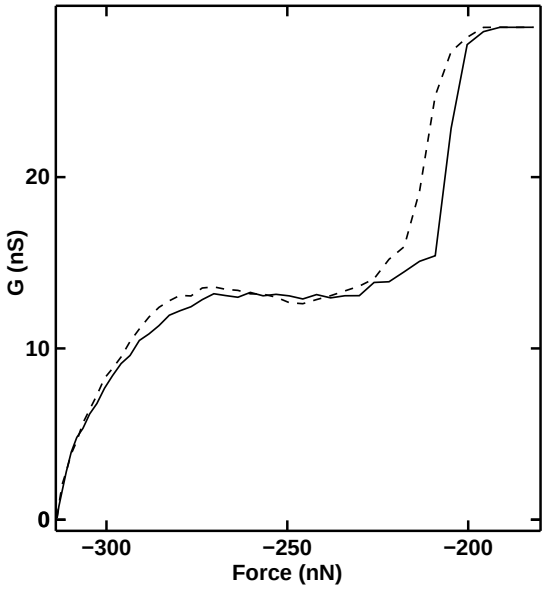

(b)

Figure 56: (a) Contact conductance versus contact area between Al tip and HOPG (R=128 nm, I_T=100 pA, V=20 mV). (b) Contact conductance versus force. The forward and reverse conductance spectra are indicated by solid and dashed lines, respectively.

4.2.2 57.5 nm Al tip

The contact conductance as a function of tip displacement for an Al tip with a radius of curvature 57.5 nm is shown in Fig. 57(a). The initial conductance occurs around 1 nS which is smaller than the previous tips. There is almost no hysteresis between the forward and reverse conductance spectra. The initial conductance is less than 0.5 nS and at this conductance the contact area spans from 0 to 400 nm^2 as shown in Fig. 57(b).

In Fig. 58(a) is shown $I(V)$ spectra at a single position taken on the surface of graphite, for different Z displacements. Most of the $I(V)$ were taken when the tip was in contact with the graphite. The $I(V)$ were taken at 2, 3, 4, 5, 6, and 7 nm Z displacements. The differential conductance dI/dV was calculated numerically from the experimental IV [Fig. 58(a)]. In Fig. 58(b) the dI/dV as a function of voltage is plotted for different tip displacements. The minima of the dI/dV spectra occur very close to zero bias voltage with perhaps some deviation for small Z displacements (spectra a & b). The minimum value of differential conductance is greater than zero at $V = 0$ ($dI/dV > 0$, at $V = 0$). This minimum dI/dV increases with Z displacement.

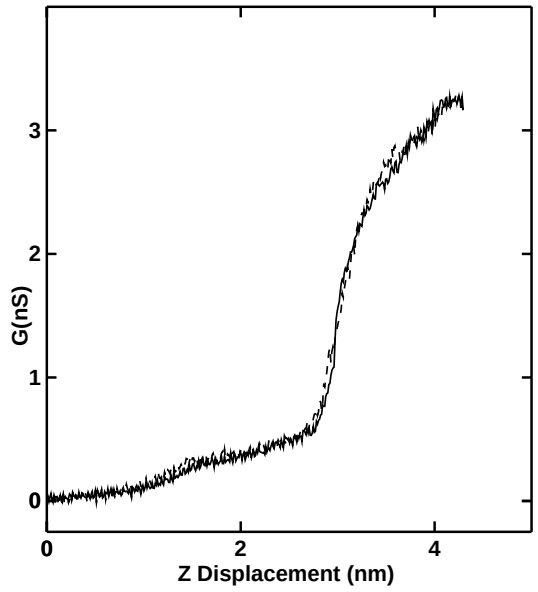

(a)

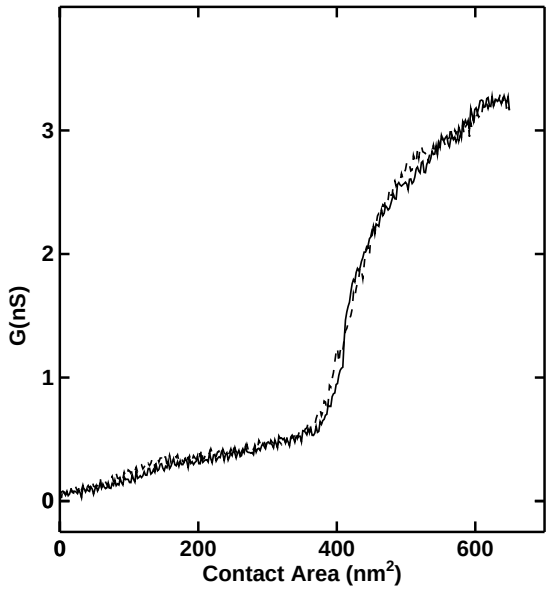

(b)

Figure 57: (a) Contact conductance versus Z displacement between Al tip and HOPG surface ($R = 57.5\ nm$, $I_T = 100\ pA$, $V = 20\ mV$). (b) Contact conductance as a function of contact area. The forward and reverse conductance spectra are indicated by a solid line and dashed line, respectively.

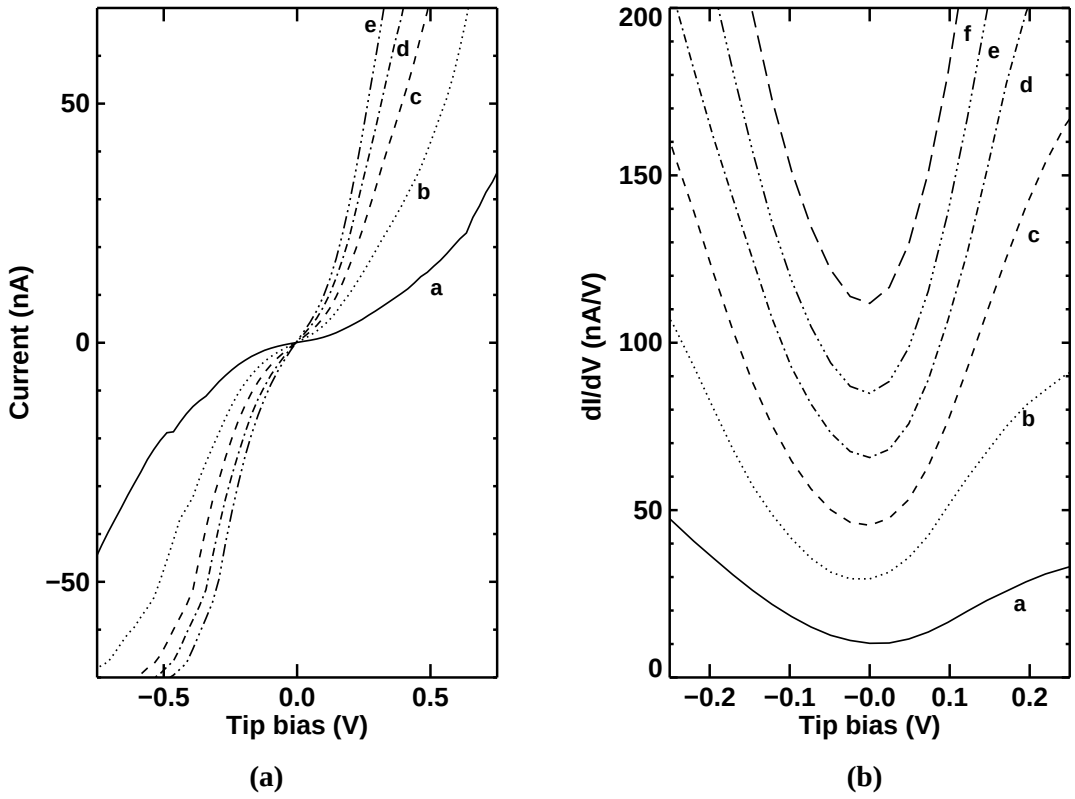

Figure 58: (a) Room temperature $I(V)$ spectra between Al tip and HOPG at different Z displacements ($R = 57.5\ nm$, $V_T = 2\ V$, $I_T = 10\ nA$) (b) dI/dV of the spectra in 58(a) at different Z displacements (a = 2 nm, b = 3 nm, c = 4 nm, d = 5 nm, e = 6 nm, and f = 7 nm).

4.2.3 Discussion

The controlling parameter in all the conductance spectra were the Z displacements. We used the Z displacements along with the tip radius of curvature for the analysis of contact area and force. The deformation displacement δ for graphite and Al tip was estimated from the Hertz model. The model shows that for a given displacements, graphite deforms 0.66δ and Al deforms 0.34δ. Thus the graphite deforms more as compared to the Al tip. In some of the field emission measurements of tips done after the contact experiments, the radius of the tip increased 50% from its value before the experiment. Thus the Al tip deforms plastically in many cases. However, there is no visible change on the image of the graphite from before contact measurements to after. Therefore we believe that the deformation of the graphite surface is quasi-elastic. Although there was not any apparent structural change on the surface of the sample taken after the contact experiments, there could be unresolved dislocation or defect movement beneath the surface [124, 125]. Note that we used the bulk Young's modulus for our analysis but the Young's modulus for a nanowire is typically bigger than the bulk Young's modulus [126].

CHAPTER V

DISCUSSION AND MODELS

The experiments described in the preceding two Chapters clearly differ in the character of the mechanical interaction of the tip with the graphite surface. The detailed mechanical interaction is subject to some variation from one spectrum to the next, as well as from one tip to the next. Nevertheless, the conductance spectra of the solid and liquid tips have much in common. For small tip displacements, a survey of the $G(Z)$ spectra presented reveals the following general features:

1. The shape of $G(Z)$ is non-exponential.
2. The hysteresis between forward and reverse $G(Z)$ spectra is typically small.
3. The scale of the initial contact conductance is extremely small (a few nS, or $< 10^{-4} Go$).
4. Conductance plateaus and/or shoulders are observed.
5. Regions of *negative* dI/dZ are occasionally observed (without significant hysteresis).
6. The minima of dI/dV spectra acquired in contact with the surface occur very close to zero bias voltage.

In this Chapter we will briefly discuss some of the aspects unique to the solid and liquid tips, respectively, but subsequently we will focus on those conductance features common to all tips. We believe that these should be related to the electronic structure of the metal-graphite contact. In the final Section, we outline a simple physical model which could account for some of our observations.

5.1 Solid tips

For electron tunneling from a solid metal tip to a typical metal sample, one expects an exponential dependence of the tunnel current on tip-sample distance, with an eventual collapse of the tunnel barrier, just before mechanical contact occurs [56, 120]. When the barrier collapses, a confined channel is formed, and the conductance is of order $1Go$. The results that we find for metal-graphite contacts are different. Conductance typically begins fairly abruptly (although a short region of exponential form is often seen), followed by a linear or sublinear rise as a function of Z. A plateau is often observed before the conductance increases more dramatically. For aluminum tips, a second conductance plateau was also seen [see e.g. Fig. 54(a), spectra 3 and 4].

The rapid increase in conductance was shown in Fig. 51 to be independent of tip radius. A schematic of the deformation of graphite layers is shown in Fig. 59. Graphite layers lying at different depths below the surface are deformed by different amounts, but clearly the largest deformation occurs for the first layer of graphite. The maximum deformation of the graphite can be shown to be independent of the tip radius [127]:

$$F = E_g a\delta_g = E_t a\delta_t \Longrightarrow E_g\delta_g = E_t\delta_t, \tag{37}$$

where F is the Hertzian force, a is contact area, $\delta = Z - Z_o = \delta_t + \delta_g$ is the total deformation displacement (controlled experimentally), δ_g is the deformation of graphite, and δ_t is the deformation of the tip. E_g and E_t are the Young's modulii of graphite and tip respectively. Thus, the deformation δ_g of graphite can be evaluated independent of the radius of the tip. Likewise, the maximum compression of the graphite interlayer spacing beneath the tip should be independent of tip radius [86, 127]. Consequently, we believe that this high conductance threshold occurs due to a rapid increase in conductance between graphite layers as they are compressed. For an applied pressure 2 GPa (one of the experimental estimated pressure), one can estimate from the elastic constants a maximum change in the interlayer spacing of 0.367 Å.

For smaller tip displacements ($< 0.8\ nm$ for Cu), we expect that the conductance properties are dominated more by in-plane electronic properties, and not by changes induced

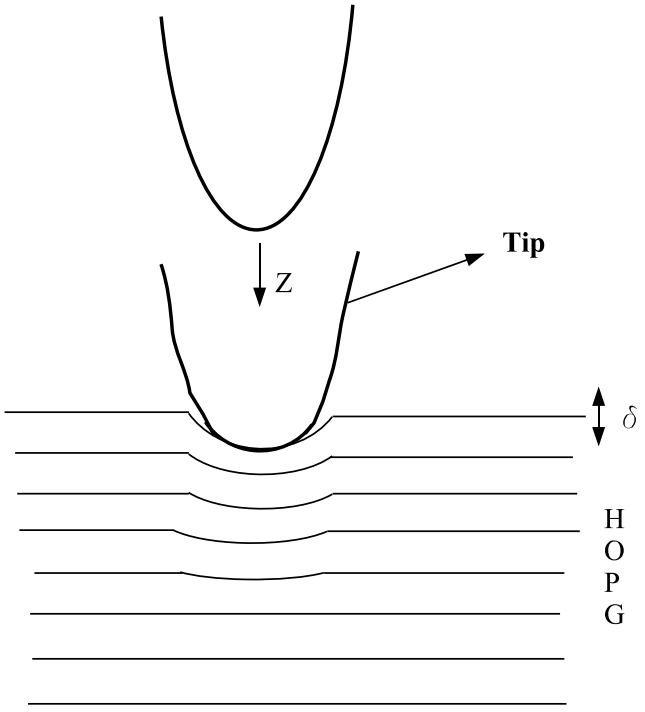

Figure 59: Schematic drawing of deformed graphite layers and tip. δ is the total deformation displacement of the tip and graphite.

by mechanical deformation. Furthermore, the small hysteresis observed for small displacements is an indication of elastic deformation of both the tip and substrate (note that Al tips tend to show somewhat larger hysteresis, however). The JKR contact theory has inherent hysteresis between the pushing and pulling directions, but the DMT model is without hysteresis. All of our analysis was done using the DMT model, as discussed in Chapter II.

5.2 Liquid tips

For liquid Ga tips, results have been presented for "large" tip-sample displacements (beyond a few nanometers) and for smaller displacements. For Ga drops (tips) below 200μm radius, we were able to image the graphite surface directly, which enables one to correlate conductance features with surface morphology. The reason for instability of the STM servo system for larger liquid tips is not known. However, there is at least one potential problem for the larger drops. As compared to smaller drops, the natural mechanical resonances of a large drop will occur at lower frequencies and with larger amplitude due to the smaller

internal pressure. This could cause an oscillatory response of the STM servo, as was observed for small servo reference current. For larger reference current (large contact area), this instability would be less likely. For the discussion which follows, we will focus on small displacements, where the results may be compared to the small-displacement results for solid tips.

5.3 Screening-charge model

The observation of a non-exponential from of $G(Z)$ for both liquid and solid tips almost certainly indicates that the tip is in contact with the surface throughout most of the range where G is nonzero. For tip tunneling voltages less than ~ 0.5 V (solid tips), the Z-displacement necessary to obtain $G = 0$ was about -0.5 to -1 nm which provides further evidence that the "tunnel" current for small bias voltage is actually due to tip-graphite contact. Other authors have reached similar conclusions [128], and the small contact conductance has been exploited previously to perform "point contact imaging" [14]. Recent measurements [129] also showed very small contact conductance (1.25 nS) between a polycrystalline tungsten tip and graphite. Despite the mechanical contact between tip and sample, however, the observed reversibility of our small-displacement $G(Z)$ spectra (solid and liquid tips) indicates that the interaction is predominantly elastic. In this regime, we expect that a model of only the electronic structure of the metal-graphite contact should explain most of the spectral features that we have observed.

In constructing a model for the contact conductance, we recognize two main issues:

- Graphite has a unique quasi-2D electronic structure with remarkably low density of states.
- Potential differences, including work function differences, are screened in any conducting material.

Because the density of states is so low in graphite, the bands must distort significantly in order to provide states for the screening charge. Screening charge is necessary to equilibrate the chemical potentials between the metal tip and the graphite substrate (the chemical

potential difference between two materials is simply the difference in work functions; our tip bias of 20 mV also contributes, but the work function difference is typically much larger). Consequently, in the limit of a single graphene sheet, we envision a 2D "puddle" of screening charge directly below the metal contact. This charge would be relatively isolated from the rest of the graphite: From underlying layers due to the inherently weak interlayer coupling, and from states in the surrounding graphene because of large reflectivity at the boundary of the potential well created to accommodate the screening charge. For graphite, multiple layers would contribute to the screening, but conductance properties would be dominated by the top graphene sheet.

For typical metals, the electron density of states is so high that screening results in distortions of the electronic structure on the μeV scale (*cf.* descriptions of Thomas-Fermi screening in elementary solid state physics books). Graphite is close to a zero-gap semiconductor, with a density of states at E_F of the order of $10^{-4}\ eV^{-1}atom^{-1}$ [42], that is, $\sim 10^4$ times smaller than a typical metal (for graphene the density of states goes to zero at E_F). The result is the formation of a potential well underneath the metal contact, whose depth is tens to hundreds of meV. The actual depth of this well is difficult to know precisely, since screening charge will be present in several graphite layers, but the depth should scale with the work-function difference (the sign of the screening charge–electrons or holes–also would be determined by the work function difference). The radius of the screening-charge well would also be substantially larger than the area of mechanical contact, since the screening length in graphite is large ($1/k_F = \sqrt{\hbar^2/2m^*E_F} \approx 6\ nm$ for graphite, using E_F =0.024 eV [130] and $m^* = 0.05m_o$ [131]).

In this Section, we examine a very simple model of the situation just described. We assume a potential well exists at the metal-graphite interface, and consider only the top graphene sheet. Electrons will be transferred from the metal to graphite during contact [or holes, if the metal work function is larger than that of graphite (4.6 eV)]. The screening-charge potential well is modelled as cylindrical, with a potential depth V_o and radius a. Figure 60 shows the model of the potential created within the graphite, underneath the metal contact. We solved the Schroedinger equation for this 2D confining potential using

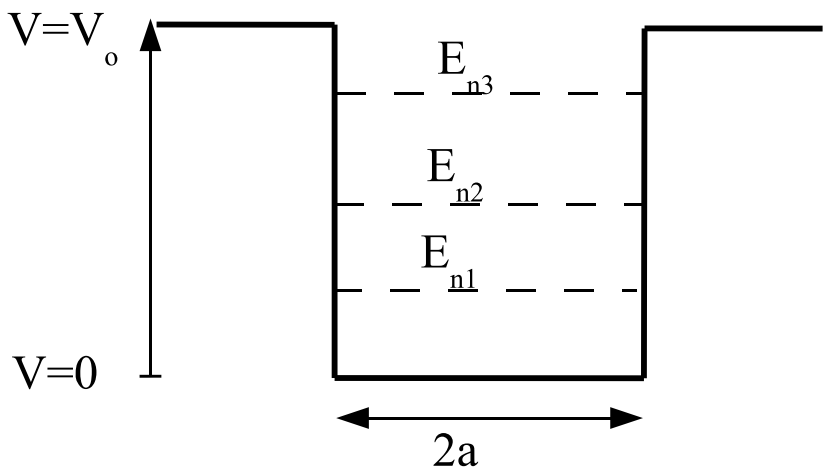

Figure 60: A model of the cylindrical potential well depth of V_o. a is the radius of cylinder. E_{ni} are the energy levels.

cylindrical coordinates:

$$\frac{-\hbar^2}{2m}\left[\frac{1}{\rho}\frac{\partial}{\partial\rho}\left(\frac{\rho\partial\Psi}{\partial\rho}\right)+\frac{1}{\rho^2}\frac{\partial^2\Psi}{\partial\theta^2}\right]+V(\rho)\Psi=E\Psi, \tag{38}$$

where

$$V(\rho)=\begin{cases}0 & \text{if } \rho\le a\\ V_0 & \text{if } \rho>a\end{cases}.$$

The solutions of the above differential equation are Bessel functions of types J and K:

$$\Psi(\rho,\theta)=\begin{cases}AJ_l(\kappa\rho)e^{\pm il\theta} & \text{if } \rho\le a\\ BK_l(K\rho)e^{\pm il\theta} & \text{if } \rho>a\end{cases},$$

where A and B are constants determined from the boundary conditions, a is the radius of the cylinder, and l is the angular momentum quantum number. κ and K are defined as follows:

$$\kappa^2=\frac{2mE}{\hbar^2}\qquad and\qquad K^2=\frac{2m}{\hbar^2}(V_o-E),$$

where V_o is the potential depth and E is the eigenvalue of the wave equation. The effective mass m for electron in graphite is $0.05m_o$ [131]. By applying the boundary condition at $\rho=a$, the eigenstates are linear combinations of Bessel functions.

The potential depth at the interface of the metal and graphite can be estimated from the work function difference and the energy dispersion of graphite. Graphene is well characterized by a linear dispersion, $E = \gamma k_{\|}$, where $\gamma = 0.58eV \cdot nm$ [132, 133]. The depth of the potential well V_0 is related to the surface charge density σ:

$$\sigma = e \int_0^{\Delta k} \frac{2}{(2\pi)^2} 2\pi k_{\|} dk_{\|} = e \int_0^{V_0} g(E) dE = \frac{e}{\pi} \int_0^{V_0} \frac{E}{\gamma^2} dE = \frac{e}{2\gamma^2 \pi} V_0^2$$

$$V_0 = \sqrt{\frac{2\pi\gamma^2\sigma}{e}} \tag{39}$$

To find σ, we estimate the electric field $\mathcal{E}$ by assuming a Ga-graphene separation d, and an electrochemical potential difference arising from the work function difference $\Delta\Phi$:

$$\sigma = \alpha\epsilon_0\mathcal{E} = \alpha\epsilon_0 \frac{\Delta\Phi}{e} \frac{1}{d}, \tag{40}$$

with α an unknown constant which accounts for imperfect screening; i.e. the screening charge will be spread over a small number of graphene layers near the surface. Thus, the potential depth V_o can be approximated as

$$V_o = \sqrt{\alpha \frac{2\pi\gamma^2\epsilon_0}{ed} \frac{\Delta\Phi}{e}} \tag{41}$$

Estimating $\alpha = 0.25$ (a conservative estimate; the screening length has been calculated to be slightly more than 1 graphene layer [134]), $d = 0.335\ nm$ (the graphite interlayer spacing), and using the literature value of $0.58eV \cdot nm$ for γ determines

$$V_0 = \left[0.295eV \cdot V^{-1/2}\right] \sqrt{\Delta\Phi/e} \tag{42}$$

Using Matlab, we solved numerically for the the eigen-energies of Eq. 38 as a function of well radius a for 6 different values of V_0. The calculation accounted for both angular and spin degeneracies. These energy spectra served as input to a simple model of the conductance which obeys the following assumptions and key points:

1. Electrons (or holes) within the screening-charge well occupy discrete eigenstates.

2. The chemical potential E_F within the screening-charge well is equilibrated with the chemical potential in the metal tip.

3. The chemical potential far outside the screening-charge well differs from that within by the applied voltage (typically 20 mV).

4. The chemical potential far outside the well is nearly coincident with the energy of carriers at the K-points of the graphene Brillouin zone.

5. Pauli exclusion prohibits direct transport of electrons within the well to occupied states at (predominantly) energies below E_F (a more detailed model would take proper account of the thermal population of states).

6. The transmission coefficient for transport of an electron (or hole) from inside the well to outside (or vice-versa) is very small, even at energies near E_F. This is due to the large impedance mismatch between states with finite kinetic energy inside the well and those outside with nearly zero kinetic energy.

7. Conductance is assumed to be proportional to the probability of escape from the well via thermal excitation from any state in the well to E_F. The escape probability is also taken to be proportional to the perimeter of the screening-charge well: $G \propto 2\pi a \cdot P(a) = 2\pi a \cdot \sum_i e^{-(V_0 - E_i)/k_B T}$. The small voltage bias and reverse current are both ignored.

Figure 61(a) shows the model thermal excitation probability as function of well radius for a potential depth $V_0 = 200\ meV$, which corresponds to Ga/HOPG. The steps in "conductance" correspond to successive additions of energy states within the quantum well as the well radius increases. Before a new state can be supported by the well, the energy of existing states decreases with increasing radius, which creates regions of decreasing escape probability between the abrupt steps. Figure 61(b) shows an experimental conductance spectrum obtained between Ga and HOPG (see also Fig. 29(b)). The model qualitatively reproduces both the abrupt conductance steps and the regions of negative slope. We associate the small values of the conductance with a small transmission coefficient (large

electron-wave impedance mismatch) from inside the well to outside.

Model thermal excitation probability as a function of well radius is shown also in Fig. 62(a), for parameters appropriate to the Cu/HOPG case ($\phi \simeq 66\ meV$). An experimental $G(Z)$ spectrum is shown for comparison in Fig. 62(b). Note that the model shows an abrupt onset of conduction and a region of positive dG/dZ just above the onset, as found experimentally (see also Fig. 32 for an example with a "hump" after the initial onset of conductance). The rapid increase of $G(Z)$ for larger experimental displacements is believed to be due to the compression of graphite planes, as explained in Sec.5.1.

Figure 63 shows the escape probability for electrons (or holes) escaping from the potential well as a function of the well radius for six different values of the well depth V_0. For the shallowest potential the escape probability increases linearly with the radius of the well. We have observed this behavior in some of our experimental results (the Cu/HOPG spectrum of Fig. 62(b) may fall into this class). For a potential depth of 0.2 eV (Ga/HOPG), no states exist in the well below 1.42 nm radius. For a potential depth 0.066 eV (Cu/HOPG), there are no states available below 2.47 nm well radius. Thus the screening-charge well is not able to hold states below a critical radius, which grows larger for smaller V_0. Note that the model critical radius is quite close to the estimated contact radius near the first ($\sim 5nS$) conductance plateau in Fig. 42.

The simple model presented here is clearly not complete, but even in this nascent form it reproduces nearly the entire range of behaviors observed in measured $G(Z)$ spectra for small displacements. We believe that it encompasses much of the basic physics of the initial metal-to-graphite contact.

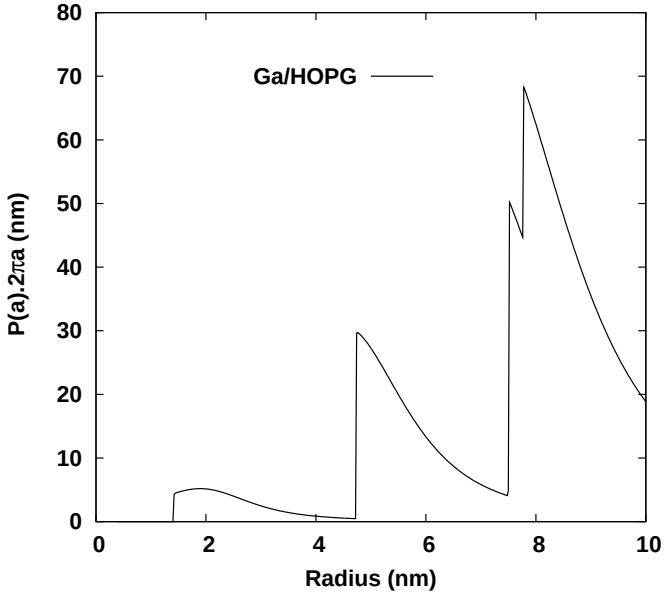

(a)

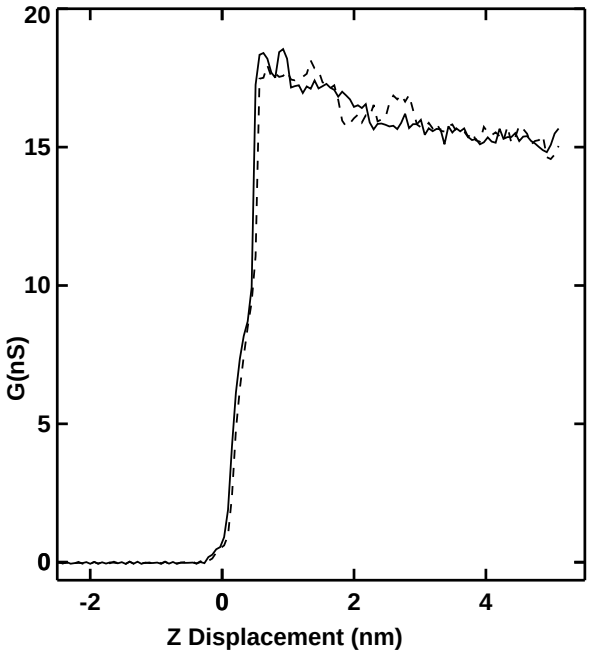

(b)

Figure 61: (a) Model: Thermal excitation probability of the states escaping from the potential well ($\phi \simeq 200\ meV$) to the outside as function of well radius for Ga-HOPG interface. (b) Experimental result: Conductance as function of tip displacement between Ga-HOPG interface ($V_T = 20\ mV, I_T = 100\ pA$).

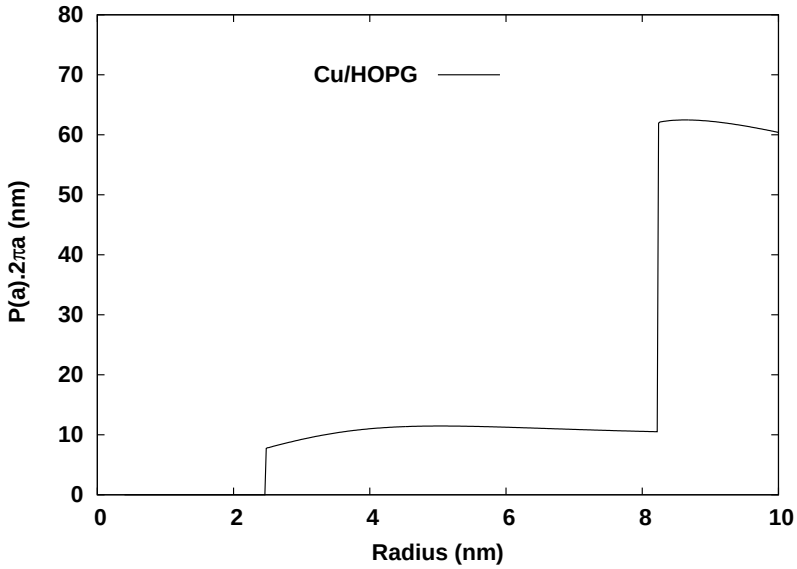

(a)

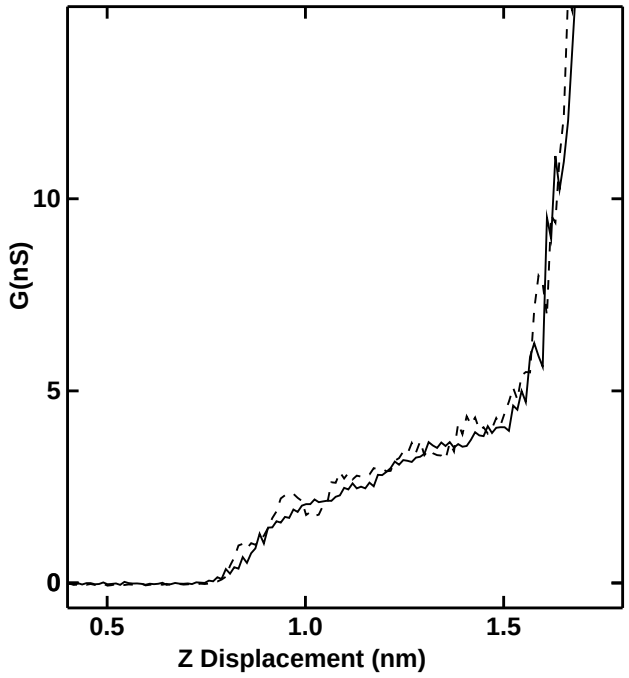

(b)

Figure 62: (a) Model: Thermal excitation probability of the states escaping from the potential well ($\phi \simeq 66\ meV$) to the outside as function of well radius for Cu-HOPG interface. (b) Experimental result: Contact conductance (Cu-to-graphite) versus tip displacement (R=44 nm, $I_T = 100\ pA, V_T = 20\ mV$).

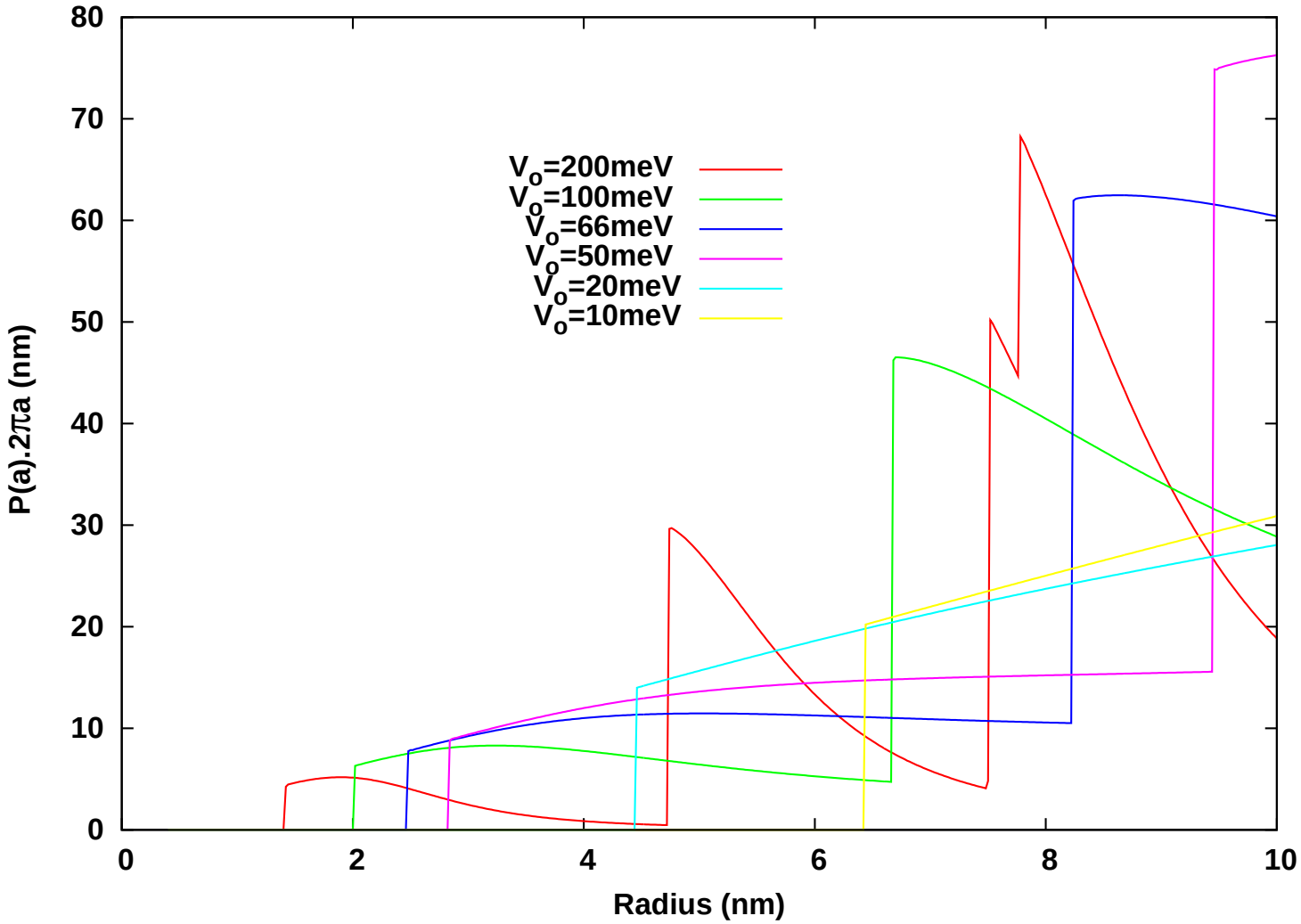

Figure 63: Room-temperature escape probability for carriers within the screening-charge potential well as a function of well radius for different potential depths V_0.

CHAPTER VI

CONCLUSIONS

6.1 Summary of the Results

The main aim of this work was to investigate the electronic properties of nanometer-scale contacts between metals and the graphite surface. The work began with Ga liquid tips in order to create a contact of easily controlled area and to decouple the effect of mechanical deformations from the electronic properties. The pressure from a liquid Ga drop-tip can be made small enough that it does not significantly distort the graphite surface during contact (kPa; substantially smaller than can be achieved in a conventional scanning force microscope). Solid metal tips of different materials (Cu, Al) were also employed to investigate the effect of metal electronic structure on the conductance. From the general characteristics of contact conductance among all of these materials (summarized in Chapter 5), we draw the following conclusions:

1. The contact conductance through nanometer-scale metal contacts on atomically-flat graphite is determined mainly by the electronic structure of graphite/graphene and the electrochemical potential difference (work function difference) between graphite and the metal contact.

2. Beyond the work function difference, the electronic structure of the metal plays only a secondary role in the contact conductance (near room temperature).

3. The thermodynamic phase (liquid or solid) also plays little role for the initial contact conductance.

4. The general features of conductance versus contact area can be explained within a simple model for the accumulation of screening charge within the top (or top few) layers of graphite.

5. The transmission coefficient is small for carriers crossing the in-plane boundary of the screening-charge potential well. This is the source of the overall small values of contact conductance.

Specific to the solid tips, we also concluded that the graphite surface deforms elastically over the few-nm range of displacements employed in this work, while the tip can deform plastically for large enough Z displacement.

During the course of conductance measurements with liquid Ga drops, it was discovered that the surface could be imaged with atomic-scale vertical resolution. To our knowledge, this is the first atomic-scale imaging of a surface using a conductive liquid tip. This capability provided us with detailed knowledge of the local surface structure, and enabled us to correlate aspects of the conductance spectra, such as hysteresis, with atomic features on the graphite surface. From analysis of these unique images, we conclude:

1. The area of contact between the Ga and graphite is only a few nanometers for typical imaging conditions (100 pA, 20 mV).

2. Wetting at the Ga/graphite interface occurs only on atomic steps and other defects.

3. The liquid tip must distort very dramatically under the influence of the applied voltage (electric field). We expect that a "Taylor cone" forms, with a nm-scale radius of curvature at its apex.

The presence of a large number of Ga nano-drops on the surface, all of similar size (3–5 nm), may indicate that the liquid tip suffers a "drop-jet" instability, although there exists no direct evidence.

6.2 Future Work

All contact conductance measurements were done at room temperature in UHV. It would be interesting to do contact experiments at low temperatures to observe the effect of temperature on the initial low conductance behavior. The electronic structure of the metal could become important in this case. The initial conductance should also be studied for a

broader range of metals, with both positive and negative work function difference relative to graphite. Also, the actual work function difference could perhaps be measured via a scanning Kelvin probe technique. This would require some changes to the STM software and electronics.

Contact forces clearly play a role in the conductance for solid tips, so it would be useful to measure simultaneously both the force and the conductance. This would require substantial modifications to the existing STM system. In order to eliminate the force completely (and thus our reliance on the DMT model), one could deposit metallic nano-islands on the surface of graphite via physical vapor deposition (evaporation). The STM tip could contact islands of different sizes (determined by imaging) to obtain conductance versus contact area. A difficulty is that the lateral diffusion of metals on graphite is so large that islands typically nucleate only at steps and defects, which would impact the interpretation of the conductance data. Low temperature growth or perhaps buffer-layer assisted growth (using a noble gas as a matrix to perform metal clusters) might be necessary to obtain islands on flat graphite terraces.

Our new method of imaging the graphite surface with liquid Ga should enable a number of new measurements aimed toward understanding wetting, friction, and perhaps fluid dynamics on the nanometer-scale. Further experiments could include velocity and direction dependent scanning to investigate friction, conductance measurements at widely varying rates for similar information, and experiments employing a wider range of drop sizes– perhaps including Ga thin films on normal STM tips. Finite-element modelling of the experiment should also prove useful for understanding the deformation of the liquid as it approaches the graphite surface and the apparent *absence* of a jetting instability during small-displacement $G(Z)$ spectroscopy.

REFERENCES

[1] S. Heinze, J. Tersoff, R. Martel, V. Derycke, J. Appenzeller, and P. Avouris. "Carbon nanotubes as Schottky barrier transistors." Phys. Rev. Lett. **89** (10) (2002).

[2] G. F. Audette, E. J. van Schalk, B. Hazes, and R. T. Irvin. "DNA-binding protein nanotubes: Learning from nature's nanotech examples." Nanoletters **4** (10), 1897–1902 (2004).

[3] M. Endo, T. Hayashi, Y. A. Kim, M. Terrones, and M. S. Dresselhaus. "Applications of carbon nanotubes in the twenty-first century." Philos. Trans. R. Soc. London, Ser. A **362** (1823), 2223–2238 (2004).

[4] Y. X. Zhou, A. Gaur, S. H. Hur, C. Kocabas, M. A. Meitl, M. Shim, and J. A. Rogers. "p-channel, n-channel thin film transistors and p-n diodes based on single wall carbon nanotube networks." Nanoletters **4** (10), 2031–2035 (2004).

[5] J. Appenzeller, J. Knoch, M. Radosavljevic, and P. Avouris. "Multimode transport in Schottky-barrier carbon-nanotube field-effect transistors." Phys. Rev. Lett. **92** (22) (2004).

[6] S. Ciraci, E. Tekman, A. Baratoff, and I. P. Batra. "Theoretical-study of short-range and long-range forces and atom transfer in scanning force microscopy." Phys. Rev. B **46** (16), 10 411–10 422 (1992).

[7] A. G. M. Jansen, A. P. Vangelder, and P. Wyder. "Point-contact spectroscopy in metals." J. Phys. C **13** (33), 6073–6118 (1980).

[8] U. Landman, W. D. Luedtke, B. E. Salisbury, and R. L. Whetten. "Reversible manipulations of room temperature mechanical and quantum transport properties in nanowire junctions." Phys. Rev. Lett. **77** (7), 1362–1365 (1996).

[9] B. J. van Wees, H. van Houten, C. W. J. Beenakker, J. G. Williamson, L. P. Kouwenhoven, D. van der Marel, and C. T. Foxon. "Quantized conductance of point contacts in a two-dimensional electron-gas." Phys. Rev. Lett. **60** (9), 848–850 (1988).

[10] N. Agrait, G. Rubio, and S. Vieira. "Plastic-deformation of nanometer-scale gold connective necks." Phys. Rev. Lett. **74** (20), 3995–3998 (1995).

[11] I. P. Batra, P. Sen, and S. Ciraci. "Quantum transport through one-dimensional aluminum wires." J. Vac. Sci. Technol. B **20** (3), 812–817 (2002).

[12] C. J. Muller, J. M. Krans, T. N. Todorov, and M. A. Reed. "Quantization effects in the conductance of metallic contacts at room temperature." Phys. Rev. B **53** (3), 1022–1025 (1996).

[13] G. Rubio, N. Agrait, and S. Vieira. "Atomic-sized metallic contacts: Mechanical properties and electronic transport." Phys. Rev. Lett. **76** (13), 2302–2305 (1996).

[14] M. Enachescu, D. Schleef, D. F. Ogletree, and M. Salmeron. "Integration of point-contact microscopy and atomic-force microscopy: Application to characterization of graphite/Pt(111)." Phys. Rev. B **60** (24), 16 913–16 919 (1999).

[15] S. Paulson, A. Helser, M. B. Nardelli, R. M. Taylor, M. Falvo, R. Superfine, and S. Washburn. "Tunable resistance of a carbon nanotube-graphite interface." Science **290** (5497), 1742–1744 (2000).

[16] D. Sundholm and J. Olsen. "Finite-element MCHF calculations on excitation-energies and the ionization-potential of carbon." Chem. Phys. Lett. **182** (5), 497–502 (1991).

[17] H. O. Pierson. *Handbook of Carbon, Graphite, Diamond, and Fullerenes* (Noyes, 1993).

[18] M. Hasegawa and K. Nishidate. "Semiempirical approach to the energetics of interlayer binding in graphite." Phys. Rev. B **70** (20) (2004).

[19] R. Zacharia, H. Ulbricht, and T. Hertel. "Interlayer cohesive energy of graphite from thermal desorption of polyaromatic hydrocarbons." Phys. Rev. B **69** (15) (2004).

[20] J. C. Charlier, X. Gonze, and J. P. Michenaud. "1st-principles study of the electronic-properties of graphite." Phys. Rev. B **43** (6), 4579–4589 (1991).

[21] C. Villaquiran, M. Gomez, and N. Luiggi. "Band structure and fermi surface of rhombohedral and simple graphites." Phys. Status Solidi B **220** (1), 691–696 (2000).

[22] H. N. Murty, , and E. A. Heintz. "Kinetics of graphitization -I. activation energies." Carbon **7** (6), 667–681 (1969).

[23] G. Kaye and T. Laby. *Tables of Physical and Chemical Constants* (Longman, London, UK, 1973).

[24] D. R. Lide. *Hand book of Chemistry and Physics* (CRC press, 2003), 84th edition.

[25] P. Wallace. "The band theory of graphite." Phys. Rev. **71** (9), 622 (1947).

[26] D. Bowen. "Theory of the electric resistivity of polycrystalline graphite." Phys. Rev. **76** (12), 1878–1878 (1949).

[27] W. W. Tyler and A. C. Wilson. "Thermal conductivity, electrical resistivity, and thermoelectric power of graphite." Phys. Rev. **89** (4), 870–875 (1953).

[28] A. Bianconi, S. B. M. Hagstrom, and R. Z. Bachrach. "Photoemission studies of graphite high-energy conduction-band and valence-band states using soft-x-ray synchrotron radiation excitation." Phys. Rev. B **16** (12), 5543–5548 (1977).

[29] J. C. Boettger. "All-electron full-potential calculation of the electronic band structure, elastic constants, and equation of state for graphite." Phys. Rev. B **55** (17), 11 202–11 211 (1997).

[30] D. Tomanek and S. G. Louie. "1st-principles calculation of highly asymmetric structure in scanning-tunneling-microscopy images of graphite." Phys. Rev. B **37** (14), 8327–8336 (1988).

[31] Z. Y. Rong. "Extended modifications of electronic-structures caused by defects - scanning-tunneling-microscopy of graphite." Phys. Rev. B **50** (3), 1839–1843 (1994).

[32] T. W. Odom, J. L. Huang, P. Kim, and C. M. Lieber. "Atomic structure and electronic properties of single-walled carbon nanotubes." Nature **391** (6662), 62–64 (1998).

[33] J. W. G. Wildoer, L. C. Venema, A. G. Rinzler, R. E. Smalley, and C. Dekker. "Electronic structure of atomically resolved carbon nanotubes." Nature **391** (6662), 59–62 (1998).

[34] V. Meunier, M. B. Nardelli, C. Roland, and J. Bernholc. "Structural and electronic properties of carbon nanotube tapers." Phys. Rev. B **6419** (19), art. no.–195 419 (2001).

[35] K. Tanaka, T. Sato, T. Yamabe, K. Okahara, K. Uchida, M. Yumura, H. Niino, S. Ohshima, Y. Kuriki, K. Yase, and F. Ikazaki. "Electronic-properties of carbon nanotube." Chem. Phys. Lett. **223** (1-2), 65–68 (1994).

[36] D. L. Carroll, P. Redlich, P. M. Ajayan, J. C. Charlier, X. Blase, A. DeVita, and R. Car. "Electronic structure and localized states at carbon nanotube tips." Phys. Rev. Lett. **78** (14), 2811–2814 (1997).

[37] P. L. McEuen, M. S. Fuhrer, and H. K. Park. "Single-walled carbon nanotube electronics." IEEE Trans. Nanotechnology **1** (1), 78–85 (2002).

[38] D. D. L. Chung. "Review Graphite." Journal of Materials Science **37** (8), 1475–1489 (2002).

[39] M. Posternak, A. Baldereschi, A. J. Freeman, and E. Wimmer. "Prediction of electronic surface-states in layered materials - graphite." Phys. Rev. Lett. **52** (10), 863–866 (1984).

[40] T. Fauster, F. J. Himpsel, J. E. Fischer, and E. W. Plummer. "3-dimensional energy-band in graphite and lithium-intercalated graphite." Phys. Rev. Lett. **51** (5), 430–433 (1983).

[41] Y. C. Wang, K. Scheerschmidt, and U. Gosele. "Theoretical investigations of bond properties in graphite and graphitic silicon." Phys. Rev. B **61** (19), 12 864–12 870 (2000).

[42] R. C. Tatar and S. Rabii. "Electronic-properties of graphite - a unified theoretical-study." Phys. Rev. B **25** (6), 4126–4141 (1982).

[43] G. Binning, H. Rohrer, C. Gerber, and E. Weibel. "Surface studies by scanning tunneling microscopy." Phys. Rev. Lett. **49** (1), 57–61 (1982).

[44] M. A. Lantz, S. J. O'Shea, and M. E. Welland. "Simultaneous force and conduction measurements in atomic force microscopy." Phys. Rev. B **56** (23), 15 345–15 352 (1997).

[45] J. Tersoff and N. Lang. *Scanning Tunneling Microscopy*, volume 27, chapter 1, p. 1 (Academic Press, INC., 1993).

[46] S. D. Alekperov, S. I. Vasiliev, V. B. Leonov, V. I. Panov, and A. E. Semenov. "An STM-study of the asymmetry of the graphite surface lattice atomic image." Doklady Akademii Nauk SSSR **307** (5), 1104–1108 (1989).

[47] Y. Sugawara, T. Ishizaka, and S. Morita. "Scanning force tunneling microscopy of a graphite surface in air." J. Vac. Sci. Technol. B **9** (2), 1092–1095 (1991).

[48] J. Tersoff and N. D. Lang. "Tip-dependent corrugation of graphite in scanning tunneling microscopy." Phys. Rev. Lett. **65** (9), 1132–1135 (1990).

[49] J. E. Yao and Y. K. Jiao. "Observing the varying scanning tunneling microscopy image of graphite." J. Vac. Sci. Technol. A **8** (1), 508–510 (1990).

[50] M. R. Soto. "The effect of point-defects on the STM image of graphite." Surf. Sci. **225** (1-2), 190–194 (1990).

[51] N. Isshiki, K. Kobayashi, and M. Tsukada. "Effect of electronic states of the tip on the STM image of graphite." Surf. Sci. **238** (1-3), L439–L445 (1990).

[52] K. F. Kelly and N. J. Halas. "Determination of alpha and beta site defects on graphite using C-60-adsorbed STM tips." Surf. Sci. **416** (1-2), L1085–L1089 (1998).

[53] S. Gwo and C. K. Shih. "Site-selective imaging in scanning-tunneling-microscopy of graphite - the nature of site asymmetry." Phys. Rev. B **47** (19), 13 059–13 062 (1993).

[54] F. Atamny, O. Spillecke, and R. Schlogl. "On the STM imaging contrast of graphite: towards a "true" atomic resolution." Phys. Chem. Chem. Phys. **1** (17), 4113–4118 (1999).

[55] H. J. Mamin, E. Ganz, D. W. Abraham, R. E. Thomson, and J. Clarke. "Contamination-mediated deformation of graphite by the scanning tunneling microscope." Phys. Rev. B **34** (12), 9015–9018 (1986).

[56] J. K. Gimzewski and R. Moller. "Transition from the tunneling regime to point contact studied using scanning tunneling microscopy." Phys. Rev. B **36** (2), 1284–1287 (1987).

[57] N. Agrait, J. G. Rodrigo, and S. Vieira. "On the transition from tunneling regime to point-contact - graphite." Ultramicroscopy **42**, 177–183 (1992).

[58] J. M. Krans, C. J. Muller, I. K. Yanson, and J. M. van Ruitenbeek. "One-atom point contacts." Physica B **194**, 1033–1034 (1994).

[59] D. P. E. Smith, G. Binnig, and C. F. Quate. "Atomic point-contact imaging." Appl. Phys. Lett. **49** (18), 1166–1168 (1986).

[60] J. C. Maxwell. *A Treatise on Electricity and Magnetism* (Oxford, 1904).

[61] Y. Sharvin. "A possible method for studying fermi surfaces." Sov. Phys. JETP **21**, 655 (1965).

[62] M. Brandbyge, J. Schiotz, M. R. Sorensen, P. Stoltze, K. W. Jacobsen, J. K. NOrskov, L. Olesen, E. Laegsgaard, I. Stensgaard, and F. Besenbacher. "Quantized conductance in atom-sized wires between 2 metals." Phys. Rev. B **52** (11), 8499–8514 (1995).

[63] D. J. Bakker, Y. Noat, A. I. Yanson, and J. M. van Ruitenbeek. "Effect of disorder on the conductance of a Cu atomic point contact." Phys. Rev. B **65** (23), 235 416 (2002).

[64] S. Ciraci and E. Tekman. "Theory of transition from the tunneling regime to point contact in scanning tunneling microscopy." Phys. Rev. B **40** (17), 11 969–11 972 (1989).

[65] D. Erts, H. Olin, L. Ryen, E. Olsson, and A. Tholen. "Maxwell and Sharvin conductance in gold point contacts investigated using TEM-STM." Phys. Rev. B **61** (19), 12 725–12 727 (2000).

[66] J. A. Torres and J. J. Saenz. "Conductance steps in point contacts: Quantization or cross-section jumps?" Physica B **218** (1-4), 234–237 (1996).

[67] J. A. Torres, J. I. PascuaL, and J. J. Saenz. "Theory of conduction through narrow constrictions in a 3-dimensional electron-gas." Phys. Rev. B **49** (23), 16 581–16 584 (1994).

[68] G. Wexler. "Size effect and non-local Boltzmann transport equation in orifice and disk geometry." Proc. Phys. Soc., London **89** (566P), 927 (1966).

[69] R. Landauer. "Electrical resistance of disordered one-dimensional lattices." Philos. Mag. **21** (172), 863–867 (1970).

[70] J. M. Soler, A. M. Baro, N. Garcia, and H. Rohrer. "Interatomic forces in scanning tunneling microscopy - giant corrugations of the graphite surface." Phys. Rev. Lett. **57** (4), 444–447 (1986).

[71] S. Frank, P. Poncharal, Z. L. Wang, and W. A. de Heer. "Carbon nanotube quantum resistors." Science **280** (5370), 1744–1746 (1998).

[72] J. M. Krans, C. J. Muller, I. K. Yanson, T. C. M. Govaert, R. Hesper, and J. M. van Ruitenbeek. "One-atom point contacts." Phys. Rev. B **48** (19), 14 721–14 724 (1993).

[73] J. M. Krans, J. M. van Ruitenbeek, V. V. Fisun, I. K. Yanson, and L. J. de Jongh. "The signature of conductance quantization in metallic point contacts." Nature **375** (6534), 767–769 (1995).

[74] J. M. Krans, J. M. van Ruitenbeek, and L. J. de Jongh. "Atomic structure and quantized conductance in metal point contacts." Phys. B **218** (1-4), 228–233 (1996).

[75] K. Johnson. *Contact Mechanics* (Cambridge University Press, 1985).

[76] I. Sridhar, K. L. Johnson, and N. A. Fleck. "Adhesion mechanics of the surface force apparatus." J. Phys. D. **30** (12), 1710–1719 (1997).

[77] G. Kaye and T. Laby. *Tables of Physical and Chemical Constants* (Longman, 1995), 16th edition.

[78] W. D. Callister. *Materials Science and Engineering: An Introduction* (John Wiley and Sons, Inc., 1997), 4th ed. edition.

[79] B. Cappella and G. Dietler. "Force-distance curves by atomic force microscopy." Surface Science Reports **34**, 1–104 (1999).

[80] K. L. Johnson, K. Kendall, and A. D. Roberts. "Surface energy and contact of elastic solids." Proc. R. Soc. London Ser., A **324** (1558), 301 (1971).

[81] B. V. Derjaguin, V. M. Muller, and Y. P. Toporov. "Effect of contact deformations on adhesion of particles." J. Colloid. Interface Sci. **53** (2), 314–326 (1975).

[82] B. V. Derjaguin, V. M. Muller, and Y. P. Toporov. "Role of molecular forces in contact deformations." J. Colloid. Interface Sci. **67** (2), 378–379 (1978).

[83] J. Drelich, G. W. Tormoen, and E. R. Beach. "Determination of solid surface tension from particle-substrate pull-off forces measured with the atomic force microscope." J. Colloid. Interface Sci. **280** (2), 484–497 (2004).

[84] N. A. Burnham and A. J. Kulik. *Handbook of micro/nano tribology*, 2nd edition (1999).

[85] B. Gady, D. Schleef, R. Reifenberger, D. Rimai, and L. P. DeMejo. "Identification of electrostatic and van der Waals interaction forces between a micrometer-size sphere and a flat substrate." Phys. Rev. B **53** (12), 8065–8070 (1996).

[86] D. S. Rimai, L. P. DeMejo, W. Vreeland, R. Bowen, S. R. Gaboury, and M. W. Urban. "The effect of Young's modulus on the surface-force-induced contact radius of spherical glass particles on polyurethane substrates." J. Appl. Phys. **71** (5), 2253–2258 (1992).

[87] J. S. William Alexander. *CRC Materials Science and Engineering Handbook* (Boca Raton, FL : CRC Press, 2001), 3rd edition.

[88] N. A. Burnham, D. D. Dominguez, R. L. Mowery, and R. J. Colton. "Probing the surface forces of monolayer films with an atomic-force microscope." Phys. Rev. Lett. **64** (16), 1931–1934 (1990).

[89] B. V. Deryagin, V. M. Muller, and Y. P. Toporov. "Influence of contact deformations on particle adhesion: 2. Macroscopic calculation of adhesive force with allowance for contact deformations in a spherical elastic particle." Colloid Journal of the USSR **37** (6), 962–969 (1975).

[90] D. Maugis. "Adhesion of spheres - the JKR-DMT transition using a Dugdale model." J. Colloid. Interface Sci. **150** (1), 243–269 (1992).

[91] P. E. Quesenberry. *Scanning Tunneling Microscopy Studies of a Reactive Interface: Ni/GaAs* (Ph.D. Thesis, Georgia Institute of Technology, 1996).

[92] *Model TPU 180, BALZERS.* 24 Trafalar square, Nashua NH 03063.

[93] *Model 500 Ion Pump, ULTEK.* Ultek Division, P. Box 10920, Palo Alto, CA 94303.

[94] *Model 1211, DL Instruments, LLC.* 176 Lake RD., Dryden, NY 13053.

[95] *Spi Supplies.* West Chester, PA 19381.

[96] E. Dujardin, T. W. Ebbesen, A. Krishnan, and M. M. J. Treacy. "Wetting of single shell carbon nanotubes." Advanced Materials **10** (17), 1472–1475 (1998).

[97] "http://environmentalchemistry.com/yogi/periodic/ , Internet."

[98] C. Berger, Y. Yi, J. Gezo, P. Poncharal, and W. A. de Heer. "Contacts, non-linear transport effects and failure in multi-walled carbon nanotubes." New Journal of Physics **5** (2003).

[99] *Model 6000 Inchworm Moter, Burleigh Instrumnets, Inc.* Burleigh Park, Fishers, NY 14453.

[100] M. Miller and G. Smith. *Atom Probe Microanalysis* (Materials Research Society, 1989).

[101] H. W. Fink. "Mono-atomic tips for scanning tunneling microscopy." IBM J. Res. Dev. **30** (5), 460–465 (1986).

[102] D. K. Biegelsen, F. A. Ponce, J. C. Tramontana, and S. M. Koch. "Ion milled tips for scanning tunneling microscopy." Appl. Phys. Lett. **50** (11), 696–698 (1987).

[103] E. W. Muller and T. T. Tsong. *Field Ion Microscopy* (American Elsevier, 1969).

[104] *Microchannel Plates, Galileo Electro-Optics Corporation.* Galileo Park, P.O.Box 550 Sturbridge, MA 01566.

[105] R. Gomer. *Field Enission and Field Ionization* (Harvard University Press, 1962).

[106] R. H. J. Good and E. W. Muller. "Field emission." Encyclopedia of Physics **XXI**, 176–231 (1956).

[107] A. W. Adamson. *Physical Chemistry of Surfaces* (Wiley, 1990), 5th edition.

[108] R. J. Hamers, R. M. Tromp, and J. E. Demuth. "Surface electronic-structure of Si(111)-(7 x 7) resolved in real space." Phys. Rev. Lett. **56** (18), 1972–1975 (1986).

[109] J. Mitterauer. "Microstructured liquid-metal ion and electron sources (MILMIS/MILMES)." Applied Surface Science **87**, 79–90 (1995).

[110] A. L. Yarin, S. Koombhongse, and D. H. Reneker. "Taylor cone and jetting from liquid droplets in electrospinning of nanofibers." J. Appl. Phys. **90** (9), 4836–4846 (2001).

[111] V. G. Suvorov and E. A. Litvinov. "Dynamic Taylor cone formation on liquid metal surface: numerical modelling." J. Phys. D. **33** (11), 1245–1251 (2000).

[112] V. G. Suvorov and N. M. Zubarev. "Formation of the Taylor cone on the surface of liquid metal in the presence of an electric field." J. Phys. D. **37** (2), 289–297 (2004).

[113] J. Tersoff. "Contact resistance of carbon nanotubes." Appl. Phys. Lett. **74** (15), 2122–2124 (1999).

[114] P. Delaney and M. Di Ventra. "Comment on Contact resistance of carbon nanotubes [Appl. Phys. Lett. 74, 2122 (1999)]." Appl. Phys. Lett. **75** (25), 4028–4029 (1999).

[115] R. Busani, M. Folkers, and O. Cheshnovsky. "Direct observation of band-gap closure in mercury clusters." Phys. Rev. Lett. **81** (18), 3836–3839 (1998).

[116] J. L. Wang, G. H. Wang, and J. J. Zhao. "Nonmetal-metal transition in Zn_n (n=2-20) clusters." Phys. Rev. A **68** (1), 013 201 (2003).

[117] Q. Wang, Q. Sun, J. Z. Yu, and Y. Kawazoe. "Nonmetal-metal transition in Ba_n clusters." Solid State Commun. **117** (11), 635–639 (2001).

[118] R. Guirado-Lopez and F. Aguilera-Granja. "Nonmetal-metal transition in Rh_n and Ru_n clusters." Phys. Lett. A **265** (1-2), 116–121 (2000).

[119] C. Kilic, H. Mehrez, and S. Ciraci. "Quantum point contact on graphite surface." Phys. Rev. B **58** (12), 7872–7881 (1998).

[120] N. D. Lang. "Apparent barrier height in scanning tunneling microscopy." Phys. Rev. B **37** (17), 10 395–10 398 (1988).

[121] L. Olesen, M. Brandbyge, M. R. Sorensen, K. W. Jacobsen, E. Laegsgaard, I. Stensgaard, and F. Besenbacher. "Apparent barrier height in scanning tunneling microscopy revisited." Phys. Rev. Lett. **76** (9), 1485–1488 (1996).

[122] N. Agrait, J. G. Rodrigo, and S. Vieira. "Conductance steps and quantization in atomic-size contacts." Phys. Rev. B **47** (18), 12 345–12 348 (1993).

[123] V. Rodrigues and D. Ugarte. "Quantum conductance properties of metal nanowires." Materials Science and Engineering B-Solid State Materials for Advanced Technology **96** (2), 188–192 (2002).

[124] T. Tsuji and K. Yamanaka. "Observation by ultrasonic atomic force microscopy of reversible displacement of subsurface dislocations in highly oriented pyrolytic graphite." Nanotechnology **12** (3), 301–307 (2001).

[125] T. Tsuji, H. Irihama, and K. Yamanaka. "Observation of dislocation behavior in graphite by using ultrasonic atomic force microscopy." JSME International Journal Series A-Solid Mechanics and Materials Engineering **45** (4), 561–566 (2002).

[126] P. S. Branicio and J. P. Rino. "Large deformation and amorphization of Ni nanowires under uniaxial strain: A molecular dynamics study." Phys. Rev. B **62** (24), 16 950–16 955 (2000).

[127] L. Kogut and I. Etsion. "Elastic-plastic contact analysis of a sphere and a rigid flat." Journal of Applied Mechanics-Transactions of the ASME **69** (5), 657–662 (2002).

[128] C. M. Mate, G. M. McClelland, R. Erlandsson, and S. Chiang. "Atomic-scale friction of a tungsten tip on a graphite surface." Phys. Rev. Lett. **59** (17), 1942–1945 (1987).

[129] S. Hembacher, F. J. Giessibl, J. Mannhart, and C. F. Quate. "Local spectroscopy and atomic imaging of tunneling current, forces, and dissipation on graphite." Phys. Rev. Lett. **94** (5), 056 101 (2005).

[130] E. Mendez, A. Misu, and M. S. Dresselhaus. "Magnetoreflection study of graphite under pressure." Phys. Rev. B **21** (2), 827–836 (1980).

[131] J. McClure. "Energy band structure of graphite." IBM J. Res. Dev. **8** (3), 255–261 (1964).

[132] S. G. Lemay, J. W. Janssen, M. van den Hout, M. Mooij, M. J. Bronikowski, P. A. Willis, R. E. Smalley, L. P. Kouwenhoven, and C. Dekker. "Two-dimensional imaging of electronic wavefunctions in carbon nanotubes." Nature **412** (6847), 617–620 (2001).

[133] M. Ouyang, J. L. Huang, and C. M. Lieber. "One-dimensional energy dispersion of single-walled carbon nanotubes by resonant electron scattering." Phys. Rev. Lett. **88** (6), 066 804 (2002).

[134] P. B. Visscher and L. M. Falicov. "Dielectric screening in a layered electron gas." Phys. Rev. B **3** (8), 2541 (1971).

VITA

Asmerom Yemane Ogbazghi was born in Mendefera, Eritrea on June 17, 1970 from Alganesh Belay and Yemane Ogbazghi. He graduated from St. George High School in 1988. He received Bachelor of Science in Physics from Addis Ababa University in 1992. He worked as a teaching assistant at the University of Asmara from 1994 to 1996. He came to Atlanta in 1996 from Eritrea for graduate study. He obtained his Master of Science in Physics from Clark Atlanta University in 1998. He came to the Georgia Institute of Technology in 1998 and he has worked in field of contact conductance metal-to-graphite under Dr. Phillip First for the last five years. He also earned an M.S. degree in Electrical and Computer Engineering from Georgia Tech in 2004. He is a member of the American Physical Society.